# UC Riverside
## UC Riverside Electronic Theses and Dissertations

**Title**

Chemical and Physical Investigation of Secondary Organic Aerosol Formation

**Permalink**

https://escholarship.org/uc/item/77q5m29m

**Author**

Nakao, Shunsuke

**Publication Date**

2012

Peer reviewed|Thesis/dissertation

UNIVERSITY OF CALIFORNIA
RIVERSIDE


Chemical and Physical Investigation of Secondary Organic Aerosol Formation

A Dissertation submitted in partial satisfaction
of the requirements for the degree of

Doctor of Philosophy


in


Chemical and Environmental Engineering


by

Shunsuke Nakao

June 2012


Dissertation Committee:
        Dr. David R. Cocker III, Chairperson
        Dr. Paul J. Ziemann
        Dr. Akua Asa-Awuku

This Dissertation of Shunsuke Nakao is approved:

_____

_____

_____
                                    Committee Chairperson


University of California, Riverside

The text of this dissertation, in part, is a reprint of the material as is appears in Nakao et al. (Atmos. Chem. Phys., 12, 3927–3937, 2012), Nakao et al. (Atmos. Chem. Phys., 11, 10649-10660, 2011), Nakao et al. (Aerosol Science and Technology, 45, 954-962, 2011), and Malloy et al. (Aerosol Science and Technology, 43, 673-678, 2009). The co-author listed in that publication directed and supervised the research which forms the basis for this dissertation.

ABSTRACT OF THE DISSERTATION

Chemical and Physical Investigation of Secondary Organic Aerosol Formation

by

Shunsuke Nakao

Doctor of Philosophy, Graduate Program in Chemical and Environmental Engineering
University of California, Riverside, June 2012
Dr. David R Cocker III, Chairperson

The overall objective of this dissertation is to advance the understanding of anthropogenic influences on SOA formation with a major focus on SOA formation from the photooxidation of aromatic hydrocarbons. This study advances the poor understanding of aromatic SOA formation through multi-generational reactions by investigating the significance of major intermediate species - specifically phenolic compounds and glyoxal. Phenolic compounds are identified to play a significant role in aromatic SOA formation (approximately 20% of aromatic SOA formed via the phenolic route, under low $NO_x$ conditions). The formation of bicyclic hydroperoxides, currently assumed in aromatic reaction mechanisms, is supported by chemical analysis utilizing a soft-ionization technique. SOA formation from glyoxal uptake onto aerosol, however, is shown to have a negligible effect on SOA formation from the oxidation of aromatic hydrocarbons (RH less than 80%) in an environmental chamber, contrary to the current belief based on simpler systems. Therefore, glyoxal is excluded as an intermediate species of aromatic SOA at least in the experimental conditions of this study.

Another facet of the body of work details development and application of a new real-time aerosol density measurement system. A recently proposed empirical relationship between SOA density and elemental composition (O/C and H/C) is evaluated against the extensive database of this study, extending the applicability of the empirical relationship towards aromatic compounds. In addition, SOA formation from diesel exhaust photooxidation is investigated by the combination of the real-time density measurement and other physical/chemical analysis, demonstrating that mass-based measurement techniques are critical in interpreting the physical processes during diesel SOA formation, i.e., evaporation of semi-volatile organics from fractal-like primary organic aerosol, as well as condensation of secondary organic compounds onto fractal-like particles. Finally, real-time density measurement is applied to the photooxidation of $CH_3I$, which produces fractal-like iodine oxide particles (IOP); density measurement is critical for determination of mass-based aerosol formation yields. Nearly all reacted iodine is found in particle phase when there is sufficiently high $O_3$, which was reasonably modeled in the absence of $NO_x$. A discrepancy between observed and modeled IOP formation in the presence of $NO_x$ suggests incomplete understanding in iodine chemistry involving $NO_x$.

**Table of Contents**

**List of Tables**

## List of Figures

# 1 Introduction

## 1.1 Introduction of Dissertation

Organic aerosol (OA) accounts for ~20-90% of aerosol mass in the lower troposphere (Kanakidou et al., 2005). OA contributes to global climate change (2007; Kanakidou et al., 2005), adverse human health risks (Davidson et al., 2005; Pope and Dockery, 2006), and visibility reduction (Eldering and Cass, 1996). OA is classified into two categories: 1) primary OA (POA) that is directly emitted from sources as particles, and 2) secondary OA (SOA) that is formed in the atmosphere from oxidative processing of gas-phase organic compounds, followed by gas-to-particle conversion; previous researchers have estimated that SOA formation from volatile precursors account for approximately 70% of OA carbon mass globally (Hallquist et al., 2009 and references therein).

Traditionally, SOA formation has been described by gas-to-particle partitioning of oxidation products of hydrocarbons (Pankow, 1994). Early works suggested that the minimum number of carbon in parent hydrocarbons of SOA is seven (Grosjean and Seinfeld, 1989; Odum et al., 1997); hydrocarbons with smaller number of carbons were believed to produce products too volatile to partition to preexisting particles. Therefore, SOA formation from oxidation of hydrocarbons with seven or more carbons typically observed in the atmosphere (e.g., substituted aromatic hydrocarbons, monoterpenes, and sesquiterpenes, herein referred as "traditional" SOA precursors) have been studied extensively.

In spite of the significant progresses in the understanding of chemical/physical processes of SOA formation (Hallquist et al., 2009), SOA formation processes from the photooxidation of aromatic hydrocarbons remain poorly understood. Typically only 10% or less of aromatic SOA mass can be identified using current analytical techniques (Cocker et al., 2001; Hamilton et al., 2005; Sato et al., 2007), making development of explicit mechanisms of aromatic SOA formation practically impossible. Although aromatic SOA has been proposed to form via multi-generational reactions, the significance of each multi-generational reaction channel remains uncertain (e.g., ring-opening products vs. ring-retaining products).

Attempts have made to predict aromatic SOA formation by modeling the explicit gas-phase mechanism with additional gas-to-particle partitioning (Johnson et al., 2004; Johnson et al., 2005); in their studies, reasonable prediction of SOA formation was acquired only after partitioning coefficients were raised by one or two orders of magnitudes, highlighting the poor understanding of the aromatic SOA formation. They proposed heterogeneous reactions as a possible missing SOA source leading to model underprediction, which remains uncertain.

In addition to the problems of the poor understanding of "traditional" SOA formation, recent studies suggest significant missing sources of SOA exist. The best understanding in mid-2000s of SOA formation from traditional precursors resulted in several fold ~ two

orders of magnitude of underestimation in SOA formation in major field campaigns,

suggesting the presence of missing sources (Volkamer et al., 2006). A number of

additional SOA forming pathways have been proposed to account for the missing sources.

Additional SOA formation pathways include formation of SOA from more volatile/less

volatile precursors than traditional SOA precursors. For example, oligomerization in

condensed phase has been proposed as a pathway for highly volatile species to form SOA

(e.g., Kalberer et al., 2004; Volkamer et al., 2009). On the other hand, organic vapors

with low volatilities may contribute to SOA formation; recent studies suggest

semivolatile components of primary organic aerosol (POA) evaporate to release

semivolatile organic compounds (SVOCs) and intermediate volatility organic compounds

(IVOCs), which easily form SOA in the atmosphere due to their lower volatility

(Robinson et al., 2007; Shrivastava et al., 2006). Significance of the SOA formation from

these non-traditional (more volatile/less volatile than traditional) precursors remains

uncertain.

In this study, a unique combination of chemical and physical approach provides new

insights on both traditional and non-traditional SOA precursors. Intermediate processes

of aromatic SOA formation is evaluated with the emphasis on phenolic compounds and

glyoxal: phenolic compounds are chosen as an example class of ring-retaining products

and glyoxal as an example of dicarbonyl ring-opening products that have been proposed

to form SOA via oligomerization by condensed-phase reactions. Another facet of this

study utilizes physical characterization techniques, primarily using particle effective

density as a tool to provide insights on chemical/physical processes of SOA formation. The following outlines each chapter in the dissertation.

Chapter 2 advances the current poor understanding of aromatic SOA formation by directly evaluating the significance of one of the major first-generation products, phenolic compounds (in low $NO_x$ conditions), and exploring possible formation mechanisms of aromatic SOA. Phenolic compounds are shown to contribute to aromatic SOA by approximately 20%, suggesting that phenolic compounds are significant intermediate species, although the majority of pathways remain unknown.

Chapter 3 evaluates the significance of another major first-generation product of aromatics, glyoxal, in aromatic SOA formation. The current belief that glyoxal can be a major intermediate of aromatic SOA, especially in humid conditions, is challenged using chemical and physical approaches, utilizing synthesized glyoxal and direct glyoxal measurements. Rapid glyoxal uptake onto deliquesced $(NH_4)_2SO_4$ seed particles are confirmed as reported by previous studies; however, glyoxal uptake onto aromatic SOA under dark/irradiated conditions in this study is demonstrated to be negligible, thus excluding glyoxal as a precursor in aromatic SOA in this study.

Chapter 4 shifts the emphasis from chemical aspects of aromatic SOA formation towards physical aspects of SOA formation and provides details on the aerosol particle mass analyzer – scanning mobility particle sizer (APM-SMPS) that is extensively utilized in

the following chapters. As opposed to the common configuration of the differential mobility analyzer (DMA)-APM, by locating the APM upstream of the SMPS, better time-resolution and sensitivity is achieved without loss of accuracy.

Chapter 5 utilizes a large database of density and elemental ratios (O/C and H/C) of SOA formed from the oxidation of 23 different volatile organic compounds (VOC) to evaluate a density estimation method recently proposed by Kuwata et al. (2011). The estimation method is shown to predict SOA density within 20% error even for SOA formed by oxidation of aromatic compounds, which was not evaluated by Kuwata et al. (2011); therefore, this study extends the applicability of the density estimation method to include anthropogenic systems.

Chapter 6 applies APM-SMPS system to SOA formation from diesel exhaust, which has acquired increasing attention as a non-traditional SOA forming pathway. The effective density measurement is especially useful in interpreting the chemical/physical processes in this system, since all the processes of 1) evaporation of semi-volatile organics from fractal-like POA (soot agglomerate), 2) condensation of secondary organics to POA, as well as 3) coagulation of particles within an environmental chamber result in changes in particle shape and effective densities. This study suggests that mass-based analysis is critical in interpreting SOA formation involving fractal-like particles and confirmed the significance of SOA formation from diesel exhaust in varied experimental conditions (e.g., dilution/injection methods).

Finally, Chapter 7 applies the chemical/physical approaches to a different system, photooxidation of methyl iodide ($CH_3I$). Although previous studies observed fractal-like iodine oxide particles (IOP) produced from the photooxidation of iodocarbons (e.g., $CH_2I_2$) (Jimenez et al., 2003), mass-based analysis of fractal-like IOP within an environmental chamber have never been performed due to the experimental difficulty of real-time density measurement. Mass-based analysis of fractal-like IOP utilizing APM-SMPS showed mass-based particle formation yield of $CH_3I$ is nearly one (0.7~1.2) with the presence of excess $O_3$ (with NO no more than a few ppb). A predictive model for gas-phase reaction and IOP formation is developed by extending SAPRC-07 mechanism to include iodine chemistry; implications of modeling results are discussed.

Furthermore, my research conducted at UCR has contributed to three additional peer-reviewed 2nd-author publications, providing new insights on chemistry and physics of SOA formation and aging processes in the atmosphere. Effects of aging (oxidative processing) were investigated in terms of chemical composition and physical properties of SOA formed by α-pinene ozonolysis with and without OH radical scavengers and *m*-xylene photooxidation. No significant aging was observed with OH radical scavengers, pointing out the critical role of OH radicals (Qi et al., 2010a). Temperature effects on SOA formation were investigated in terms of chemical composition and physical properties (volatility and density); temperature was shown to have significant impacts on SOA formation from *m*-xylene photooxidation, which could not be described solely by

thermodynamics, suggesting the presence of thermally-labile compounds in SOA (Qi et al., 2010b). SOA formation from a series of conjugated dienes (isoprene, 1,3-butadiene, and 2,3-dimethyl-1,3-butadiene) was investigated under high $NO_x$ conditions. Effects of ketone and aldehyde groups on SOA formation were discussed and oligomer formation was observed even at atmospherically relevant low SOA mass loadings (Sato et al., 2011).

## 1.2    References

Cocker, D. R., Mader, B. T., Kalberer, M., Flagan, R. C., Seinfeld, J. H.: The effect of water on gas-particle partitioning of secondary organic aerosol: 2. m-xylene and 1,3,5-trimethylbenzene photooxidation systems, Atmospheric Environment, 35, 6073-6085, 2001

Davidson, C. I., Phalen, R. F., Solomon, S.: Airborne particulate matter and human health: A review, Aerosol Science and Technology, 39, 737-749, 2005

Eldering, A., Cass, G. R.: Source-oriented model for air pollutant effects on visibility, Journal of Geophysical Research, 101(D14), 19343-19369, 1996

Grosjean, D., Seinfeld, J. H.: Parameterization of the formation potential of secondary organic aerosols, Atmospheric Environment, 23(8), 1733-1747, 1989

Hallquist, M., Wenger, J. C., Baltensperger, U., Rudich, Y., Simpson, D., Claeys, M., Dommen, J., Donahue, N. M., George, C., Goldstein, A. H., Hamilton, J. F., Herrmann, H., Hoffmann, T., Iinuma, Y., Jang, M., Jenkin, M., Jimenes, J. L., Kiendler-Scharr, A., Maenhaut, W., McFiggans, G., Mentel, T. F., Monod, A., Prevot, A. S., Seinfeld, J. H., Surratt, J. D., Szmigielski, R., Willdt, J.: The formation, properties and impact of secondary organic aerosol: current and emerging issues, Atmospheric Chemistry and Physics, 9, 5155-5236, 2009

Hamilton, J. F., Webb, P. J., Lewis, A. C., Reviejo, M. M.: Quantifying small molecules in secondary organic aerosol formation during the photo-oxidation of toluene with hydroxyl radicals, Atmospheric Environment, 39, 7263-7275, 2005

IPCC (2007). Intergovernmental Panel on Climate Change: Climate Change 2007: The Physical Science
Basis, Cambridge University Press, UK.

Jimenez, J. L., Bahreini, R., Cocker, D. R., Zhuang, H., Varutbangkul, V., Flagan, R. C., Seinfeld, J. H., O'Dowd, C. D., Hoffman, T.: New particle formation from photooxidation of diiodomethane ($CH_2I_2$), Journal of Geophysical Research, 108(D10) 2003

Johnson, D., Jenkin, M., Wirtz, K., Martin-Reviejo, M.: Simulating the formation of secondary organic aerosol from the photooxidation of toluene, Environ. Chem., 1, 150-165, 2004

Johnson, D., Jenkin, M. E., Wirtz, K., Martin-Reviejo, M.: Simulating the formation of secondary organic aerosol from the photooxidation of aromatics hydrocarbons, Environ. Chem., 2, 35-48, 2005

Kalberer, M., Paulsen, D., Sax, M., Steinbacher, M., Dommen, J., Prevot, A. S., Fisseha, R., Weingartner, E., Frankevich, V., Zenobi, R., Baltensperger, U.: Identification of polymers as major components of atmospheric organic aerosols, Science, 303, 1659-1662, 2004

Kanakidou, M., Seinfeld, J. H., Pandis, S. N., Barnes, I., Dentener, F. J., Facchini, M. C., Van Dingenen, R., Ervens, B., Nenes, A., Nielsen, C. J., Swietlicki, E., Putaud, J. P., Balkanski, Y., Wilson, J.: Organic aerosol and global climate modelling: a review, Atmospheric Chemistry and Physics, 5, 1053-1123, 2005

Kuwata, M., Zorn, S. R., Martin, S. T.: Using Elemental Ratios to Predict the Density of Organic Material Composed of Carbon, Hydrogen, and Oxygen, Environmental Science & Technology, 46(2), 787-794, 2011

Odum, J. R., Jungkamp, T. P. W., Griffin, R. J., Forstner, H. J. L., Flagan, R. C., Seinfeld, J. H.: Aromatics, reformulated gasoline, and atmospheric organic aerosol formation, Environmental Science & Technology, 31, 1890-1897, 1997

Pankow, J. F.: An absorption model of gas/particle partitioning of organic compounds in the atmosphere, Atmospheric Environment, 28(2), 185-188, 1994

Pope, C. A., Dockery, D. W.: Health effects of fine particulate air pollution: Lines that connect, J. Air & Waste Manage. Assoc., 56, 709-742, 2006

Qi, L., Nakao, S., Malloy, Q., Warren, B., Cocker, D. R.: Can secondary organic aerosol formed in an atmospheric simulation chamber continuously age?, Atmospheric Environment, 44, 2990-2996, 2010a

Qi, L., Nakao, S., Tang, P., Cocker III, D. R.: Temperature effect on physical and chemical properties of secondary organic aerosol from m-xylene photooxidation, Atmos. Chem. Phys., 10(8), 3847-3854, 2010b

Robinson, A. L., Donahue, N. M., Shrivastava, M. K., Weitkamp, E. A., Sage, A. M., Grishop, A. P., Lane, T. E., Pierce, J. R., Pandis, S. N.: Rethinking organic aerosols: Semivolatile emissions and photochemical aging, Science, 315, 1259-1262, 2007

Sato, K., Hatakeyama, S., Imamura, T.: Secondary organic aerosol formation during the photooxidation of toluene: NOx dependence of chemical composition, J. Phys. Chem. A, 111, 9796-9808, 2007

Sato, K., Nakao, S., Clark, C. H., Qi, L., Cocker III, D. R.: Secondary organic aerosol formation from the photooxidation of isoprene, 1,3-butadiene, and 2,3-dimethyl-1,3-butadiene under high NOx conditions, Atmos. Chem. Phys., 11(14), 7301-7317, 2011

Shrivastava, M. K., Lipsky, E. M., Stanier, C. O., Robinson, A. L.: Modeling semivolatile organic aerosol mass emissions from combustion systems, Environmental Science & Technology, 40(8), 2671-2677, 2006

Volkamer, R., Jimenez, J. L., Martini, F. S., Dzepina, K., Zhang, Q., Salcedo, D., Molina, L. T., Worsnop, D. R., Molina, M. J.: Secondary organic aerosol formation from

anthropogenic air pollution: Rapid and higher than expected, Geophysical Research Letters, 33(L17811), doi: 10.1029/2006GL026899, 2006

Volkamer, R., Ziemann, P. J., Molina, L. T.: Secondary organic aerosol formation from acetylene (C2H2): seed effect on SOA yields due to organic photochemistry in the aerosol aqueous phase, Atmospheric Chemistry and Physics, 9, 1907-1928, 2009

## 2 Secondary Organic Aerosol Formation from Phenolic Compounds in the Absence of NO$_x$

### 2.1 Introduction

Secondary organic aerosol (SOA) is formed from oxidative processing of volatile organic compounds in the atmosphere. SOA has been suggested to contribute to climate change (IPCC, 2007; Kanakidou et al., 2005), adverse human health effects (Davidson et al., 2005; Pope and Dockery, 2006), and a reduction in visibility (Eldering and Cass, 1996). Previous researchers have estimated approximately 70% of organic aerosols are secondary in nature (Hallquist et al., 2009 and references therein). Aromatic hydrocarbons comprise ~20% of nonmethane hydrocarbons in the urban atmosphere and are considered to be one of the major precursors to urban SOA (Calvert et al., 2002).

A number of studies have investigated gas-phase photooxidation of aromatic hydrocarbons (e.g., Arey et al., 2009; Calvert et al., 2002; Coeur-Tourneur et al., 2006; Johnson et al., 2004; Johnson et al., 2005; Olariu et al., 2002; Takekawa et al., 2003; Volkamer et al., 2002). Previously identified first generation products of aromatic compound photooxidation explain approximately 50% of carbon balance (Calvert et al., 2002). Although multigenerational reactions have been suggested to contributed to aromatic SOA formation (Hurley et al., 2001; Ng et al., 2007; Sato et al., 2007), the extent of the contribution from the second or further reaction products to SOA is poorly understood.

Phenolic compounds are one of the major first generation products of OH reaction with aromatic hydrocarbons (Calvert et al., 2002). Previous studies suggested the major gas-phase reaction products from OH reaction of phenolics are dihydroxy compounds (e.g., 80% catechol formation from phenol, Olariu et al. (2002)). However, the mechanisms of SOA formation from phenolic compounds are highly uncertain. In addition, since phenolic compounds are significant products in wood smoke (Hawthorne et al., 1989; Hawthorne et al., 1992; Schauer et al., 2001; Simoneit, 1999), the reaction mechanism of phenolic compounds leading to SOA formation is of a great interest (Chang and Thompson, 2010; Coeur-Tourneur et al., 2010a; Coeur-Tourneur et al., 2010b; Grosjean, 1984; Henry et al., 2008; Iinuma et al., 2010; Sun et al., 2010).

SOA formation from individual aromatic and phenolic compounds were investigated using an environmental chamber under low $NO_x$ (and high $HO_2$) conditions to evaluate the role of phenolic species in SOA formation from aromatic hydrocarbons. Chemical analysis was performed using on-line and off-line mass spectrometry to infer the structure of aromatic and phenolic SOA.

## 2.2   Experimental

### 2.2.1   Environmental chamber

Most of the experiments were conducted in the UC Riverside/CE-CERT environmental chamber described in detail in Carter et al. (2005). In short, this facility consists of dual $90m^3$ Teflon® reactors suspended by rigid frames in a temperature controlled enclosure

(27 ± 1 °C) continuously flushed with dry (a dew point below -40 °C) purified air generated by an Aadco 737 series (Cleves, Ohio) air purification system. The top frames are slowly lowered during the experiments to maintain a slight positive differential pressure (0.03"$H_2O$) between the reactors and enclosure to minimize dilution and possible contamination of the reactors. 272 115W Sylvania 350 black lights are used as the light source for all the experiments reported herein.

Some of the results of dimethylphenols (DMPs) were acquired in the UCR/CE-CERT mezzanine chamber (Nakao et al., 2011). The UCR/CE-CERT mezzanine chamber is within a 2.5 m x 3 m x 7.8 m enclosure covered with reflective aluminum sheets and is illuminated with 170, 40W blacklights with peak intensity at 350 nm (SYLVANIA, 350 BL) with the $NO_2$ photolysis rate of 0.6 min$^{-1}$. Within this enclosure is a 12 m$^3$ volume 2 mil FEP Teflon® film reactor. A minimum of 1 m space between the reactor surface and blacklights avoids excessive heating at the surface of the film. Additionally, six fans are used to mix the air inside the enclosure with room air to minimize heating in the enclosure. Prior to each experiment, the bag is flushed overnight with purified air. Background particle concentration is below the detection limit of 0.2 cm$^{-3}$.

### 2.2.2    Gas and particle analysis

The Agilent 6890 Gas Chromatograph – Flame Ionization Detector was used to measure concentrations of reactants and products. All phenolic compounds were analyzed by a GC equipped with a thermal desorption system (CDS analytical, ACEM9305, Sorbent

Tube MX062171 packed with Tenax-TA/Carbopack/Carbosieve S111) except for dimethylphenols for mezzanine chamber experiments. Aromatic hydrocarbon measurements were calibrated using a dilute gas cylinder (SCOTT-MARIN, Inc) or by introducing known amount of liquid hydrocarbons into the reactor. Calibration for phenolic compounds was performed by impregnation of the glass cartridges with known quantities of phenolic compounds in acetonitrile. The Ionicon Proton Transfer Reaction – Quadrupole Mass Spectromer (PTR-MS) was used to measure dimethylphenol decay for mezzanine chamber experiments.

Particle size distribution between 27 nm and 686 nm was monitored by a custom built Scanning Mobility Particle Sizer (SMPS) similar to that described by Cocker et al. (2001). Particle effective density was measured with an Aerosol Particle Mass Analyzer (APM, Kanomax) (Ehara et al., 1996) and SMPS in series. The APM is located upstream of the SMPS for improved time resolution and sensitivity (S/N) over the more common configuration of Differential Mobility Analyzer (DMA) – APM (Khalizov et al., 2009; McMurry et al., 2002; Xue et al., 2009). A detailed description of the APM-SMPS system and data algorithms are described elsewhere (Malloy et al., 2009).

The high resolution time-of-flight aerosol mass spectrometer (HR-ToF-AMS) (DeCarlo et al., 2006) was operated in high resolution W mode. Elemental analysis (EA) was used to determine the atomic ratio (O/C) of non-refractory organic aerosols (Aiken et al., 2008).

The Agilent 6210 Accurate-Mass Time-of-Flight Mass Spectrometer equipped with multimode ionization source for electrospray and atmospheric pressure chemical ionization (ESI/APCI-TOFMS) is used to obtain accurate mass of analytes. Soft ionization by ESI and APCI provides lower fragmentation of the analytes compared to electron impact (EI) used for the HR-ToF-AMS or other conventional GC-MS techniques. Mass accuracy is routinely calibrated by standard compounds (Agilent low concentration MMI tuning mix, G1969-85020) before analysis and in most cases mass accuracy of less than 5ppm is achieved. Occasionally higher mass errors (~30ppm) were observed during sample analysis, which resulted in a consistent shift of mass throughout the mass range of the instrument. Since the extent of the shift can be inferred from repeatedly observed ions (e.g., pyruvic acid), formulas were carefully assigned based on tendency of shift and repeat experiments. Filter samples were collected onto Teflo® filters (2μm, 47mm, PALL Life Sciences) at 25 L/min for 1~4 hours. After collection, filters were stored in a freezer until extraction. Extractions were achieved by sonicating the filter in 5mL of acetonitrile. The extract volume was reduced under a gentle stream of $N_2$ until near dryness and reconstituted by 300 μL of acetonitrile/water/acetic acid (50/50/0.1v). Samples were directly infused to the TOFMS. A: Water (0.1v% acetic acid) and B: acetonitrile were used as eluents (B 50%, 0.5mL/min). Acetonitrile was chosen as the organic solvent to reduce the solvent-analyte reaction compared to methanol (Bateman et al., 2008). Mixed mode ionization (simultaneous APCI and ESI) was used with vaporizer temperature 200°C, nebulizer pressure 40 psig, corona current 2 μA, fragmentor voltage

100V. Although the mixed mode is used to survey a wide range of products, the resulting

major signals were the same as in ESI only. APCI yielded lower sensitivity in this study.

All Agilent TOFMS data was acquired in negative ion mode.

A Particle-Into-Liquid-Sampler (PILS) (Orsini et al., 2003; Weber et al., 2001) was

interfaced with the TOFMS to provide an on-line accurate mass analysis of water soluble

organic compounds (Bateman et al., 2010). In order to couple the PILS (Brechtel

Manufacturing Inc.) to the TOFMS, the use of HPLC pumps in addition to a commonly

used peristaltic pump was critical to overcome the backpressure of the TOFMS inlet and

to supply steady flow of water (18.2 MΩ, Milli-Q, Millipore) into the boiler. The PILS-

TOFMS system will be described in more detail in an upcoming publication (Clark et al.,

2011). The negative ESI was used as the ionization method with similar conditions as the

filter analysis without the corona current.

### 2.2.3    Chamber experiments

The experimental test matrix is summarized in Table 2.1. A known volume of high purity

liquid aromatic hydrocarbon (All purchased from Sigma-Aldrich: ≥99% or ≥99.5%,

except 2,4-DMP ≥98%) was injected through a heated glass injection manifold system

and flushed into the chamber with pure $N_2$. Since phenolic compounds are less volatile

than hydrocarbons typically used for chamber experiments, injection into the chambers

were carefully performed using a heated oven (50~80°C) through a heated transfer line

maintained at a temperature higher than the oven. The glass manifold inside the oven was

16

packed with glass wool to increase the mass transfer surface area. Since reasonable

agreement between the calculated concentration of phenolics (based on injected amount)

and observed concentrations were confirmed, loss of phenolics in the transfer line and to

the wall was assumed to be negligible. $H_2O_2$ was used as an OH (and $HO_2$) radical source.

$H_2O_2$ 50wt% solution was injected through the same oven system. Since the $H_2O_2$

solution did not spread through glass wool, the glass wool was processed with an

acid/base bath and cleaned by water and acetone which enabled the $H_2O_2$ solution to

spread. Initial $H_2O_2$ concentration was not measured, but is estimated to be 1~5ppm

based on amount injected and hydrocarbon decay rate. No seed particles were used in this

study. Exponential decay rates of particle number is used to calculate particle volume

wall loss (Carter et al., 2005). To investigate the role of organic peroxides, additional

high NO experiments were also performed and the chemical composition of SOA was

compared to low $NO_x$ condition. Initial ratio of approximately 50/50/500 ppb for

phenolic/methyl nitrite/NO was used to ensure that excess NO was present to suppress

$RO_2 + HO_2$ reaction.


## 2.3    Results and Discussion

### 2.3.1    SOA formation

SOA yield (Y) is defined as the mass of aerosol formed (wall-loss-corrected) ($M_o$)

divided by mass of hydrocarbon reacted ($\Delta HC$)

$$Y = \frac{M_o}{\Delta HC}$$                                        Equation 1

Its dependence on aerosol mass loading has been traditionally parameterized by  as

shown below: (Odum et al., 1996)

$$Y = \sum Y_i = M_o \sum_i \frac{\alpha_i K_i}{1 + M_o K_i}$$
Equation 2

where $\alpha_i$ is the mass-based stoichiometric coefficient for the reaction generating product $i$,

$K_i$ is the partitioning coefficient of product $i$. Equation 1 and 2 were applied for the SOA

yields obtained (Figure 2.1). Particle density of 1.4 g/cm$^3$ was used. 2,4-DMP had the

highest SOA formation potential of the three DMP isomers, with a SOA yield

approximately twice as high as the other DMP isomers. SOA yield from phenol was

higher than benzene.

SOA from aromatic hydrocarbons formed under low $NO_x$ conditions was previously

reported to be effectively non-volatile (Ng et al., 2007), in which case SOA yield would

be independent of particle mass concentration (flat SOA yield curves). However, for

benzene, *o-/m*-cresol, and possibly DMPs, the SOA yield was observed to be slightly

dependent on particle concentration. Therefore, in this study, constant SOA yield was not

assumed and a one product model fit was applied to perform calculation of the

contribution of phenolic route in the following section of the contribution of phenolic

route.

### 2.3.2    Contribution of phenolic route

The formation yields of phenolics from aromatics were obtained. An example for *o-*

cresol and *m/p*-cresol formation from toluene is shown in Figure 2.2. The cresol

formation yields from toluene were calculated from measured cresol by correcting for the

further reaction of cresols with OH. Equations in Atkinson et al. (1982) and rate constants from Calvert et al. (2002) were used for the correction. Phenol, cresols, and DMPs formation yields are in reasonable agreement with previous studies (Table 2.3) (Atkinson, 1989; Atkinson et al., 1991; Berndt and Böge, 2006; Klotz et al., 1998; Smith et al., 1999; Smith et al., 1998; Volkamer et al., 2002).

Contributions of the phenolic route to aromatic SOA formation in the low $NO_x$ system were estimated by combining SOA yield measurement (Figure 2.1), phenolic yields, and consumption of phenolics (e.g., Figure 2.2). The amount of phenolics (as products) reacted is calculated as the gap between the observed concentration of phenolic compounds and the concentration corrected for the secondary reaction. Phenolic route SOA is calculated by multiplying reacted phenolics and their SOA yield at appropriate mass loading using the phenolic SOA yield curves in Figure 2.1. SOA yields from cresol isomers (*o*-, *m*-, and *p*-) were assumed to be the same (Henry et al., 2008). The ratio of 2,4-DMP and 2,6-DMP produced from OH reaction of *m*-xylene was assumed to be the same as that reported by Smith et al. (1999). Formation of 3,5-DMP is assumed to be insignificant (Smith et al., 1999). Contribution of the phenolic route in the no $NO_x$ system is summarized in Table 2.1. The contribution was approximately 20% for benzene, toluene, and *m*-xylene in low $NO_x$ conditions.

## 2.4    Particle chemical composition

### 2.4.1    SOA elemental ratio and density

The results of elemental analysis of HR-ToF-AMS data (O/C ratio) are shown in Figure 2.3. The O/C ratios during the experiments were nearly constant with only a small increase in O/C observed over time. The O/C ratio decreased as the number of methyl substituents on the parent aromatic ring increased; ~0.6 for $C_6$ species (benzene, phenol, and catechol), ~0.5 for $C_7$ species (toluene and cresols), and ~0.4 for $C_8$ species (*m*-xylene and dimethylphenols). The decrease in O/C is approximately consistent with the increasing number of carbons in the parent aromatics, indicating that the methyl substituents did not play a major role in the SOA formation mechanism. Therefore the H-abstraction from methyl substituents is not likely to be an important route to aromatic SOA formation under low $NO_x$ conditions. The O/C ratios of SOA between aromatic hydrocarbons and corresponding phenolics were similar, suggesting the significance of multi-generational reactions.

Real-time SOA density measured by the APM-SMPS is shown in Figure 2.4. The SOA densities were observed to be initially high (~1.8 g/cm$^3$), which could be due to high density of nucleating species. The final SOA densities were in the range of 1.3-1.4 g/cm$^3$, in reasonable agreement with previous studies (Ng et al., 2007; Sato et al., 2010). Although Bahreini et al. (2005) observed weak correlation between effective density and relative contribution of m/z 44 signal to total organic signal of AMS, the final SOA densities were found to be independent of elemental composition of SOA from aromatics

tested in this study (Figure 2.5). Therefore a constant SOA density (1.4 g/cm$^3$) is applied to all the experiments in this study.

### 2.4.2 Filter analysis

Chemical composition of SOA was analyzed by off-line filter analysis. Samples were directly infused to the ESI/APCI-TOFMS. Although direct infusion of SOA extract into ESI-MS is often done (e.g., Altieri et al., 2006; Camredon et al., 2010; De Haan et al., 2009; Heaton et al., 2009), caution must be taken in interpreting the mass spectrums due to possible formation of adducts or analyte-solvent reaction products (Bateman et al., 2008; Pratt and Prather, 2011). Mass spectra obtained by ESI/APCI-TOFMS are shown in Figure 2.6. High mass accuracy measurements enabled determination of empirical formula typically within 5 ppm mass error. Inclusion of nitrogen or halogens in the formula calculation did not yield reasonable formulae. Major ions in each spectrum contained the same number of carbon as reactants (e.g., $C_6H_8O_6$ from phenol, $C_7H_{10}O_6$ from $o$-cresol, and $C_8H_{12}O_6$ from 2,4-DMP).

The possibility of adduct formation between acetic acid mobile phase modifier and analytes was investigated by changing acetic acid to formic acid; however, the major signals were still the same, indicating that the observed products are not adducts of the acid modifier. Acetonitrile was used in this study instead of methanol to reduce the risk of analyte-solvent reactions (particularly reactions of methanol and carbonyls or carboxylic acids) (Bateman et al., 2008). Tests substituting methanol as an organic

solvent did not alter the major MS signal distribution indicating those MS signals did not result from analyte-solvent reaction. The agreement of carbon number and apparent $CH_2$ shift with increasing number of methyl substituents on the aromatic precursor suggests that these major signals are not likely to be adducts formed during ionization.

Since only formulae were determined and no structural information is available in this study, there are a number of possible structures such as unsaturated multi-functional ring-opening products (e.g., diacids, polyols). Although column separation using different types of reverse-phase column was attempted, most of the major signals appeared in the non-retained peak, indicating that these species were too polar to be retained by conventional reversed-phase columns.

Another possible reaction products consistent with these formulae of the major signals are the bicyclic hydroperoxides formed from the reaction of $HO_2$ and bicyclic peroxy radicals (Figure 2.7). The formation of bicyclic peroxy radicals intermediate from OH-initiated reaction of aromatic hydrocarbons in gas-phase has been reported experimentally and theoretically (Andino et al., 1996; Birdsall et al., 2010; Birdsall and Elrod, 2011; Glowacki et al., 2009; Huang et al., 2008; Wyche et al., 2009). Johnson et al. (2004; 2005) predicted bicyclic hydroperoxides as one of the predominant aerosol species from aromatic hydrocarbons. Currently, organic peroxides such as hydroperoxides and peroxyhemiacetals have been suggested to be important component of SOA (e.g., monoterpene ozonolysis (Docherty et al., 2005), isoprene photooxidation (Surratt et al.,

2006), naphthalene photooxidation (Kautzman et al., 2010), and toluene photooxidation (Sato et al., 2007)). Reinnig et al. (2008) reported that the parent ion from two hydroperoxide surrogates, cumene hydroperoxide and tert-butylhydroperoxide were not seen by either negative or positive mode ESI and APCI. Further, only fragments for cumene hydroperoxide were observed for ESI and APCI operating only in the positive mode and for tert-butylhydroperoxide only in the positive APCI mode. This poses an uncertainty in our detection of bicyclic hydroperoxide in this study; however, since the tentatively proposed bicyclic hydroperoxide are highly oxidized and multi-functional (with an oxygen-bridge), other functional groups may enable the ionization.

The presence of peroxides was investigated by conducting phenol photooxidation experiments under excess NO. In excess NO condition, the (bicyclic) peroxy radicals rapidly react with NO to form the alkoxy radical, which is suggested to undergo decomposition (Atkinson, 2000; Calvert et al., 2002). The resulting mass spectrum (after separating nitrophenolic species by a reverse phase column; not shown) indicated $C_6H_8O_6$ and $C_6H_8O_7$ were still present, suggesting that at least some fraction of $C_6H_8O_6$ and $C_6H_8O_7$ are formed via a non-peroxy radical route. Although uncertainty remains, it is still interesting that major signals in ESI/APCI-TOFMS matched the widely recognized bicyclic hydroperoxides. Additional analytical techniques, such as column separation of the highly polar species, derivatization, MS/MS or NMR, are necessary for unambiguous identification of the products.

### 2.4.3 PILS-TOFMS

Mass spectra obtained by PILS-ESI-TOFMS of SOA formed from OH reaction with phenol, catechol, and *o*-cresol are shown in Figure 2.8. Major signals observed from off-line filter analysis were also observed by the on-line PILS-TOFMS such as m/z 175 and 191 from the phenol SOA mass spectrum (Figure 2.8 (a)). Since the PILS-TOFMS was operated without a denuder upstream, water soluble gas-phase compounds can potentially be collected by the PILS system. The highest signal in Figure 2.8 (a) (mass spectrum when SOA was highest), m/z109 is catechol ($C_6H_6O_2$), which is consistent with previous gas-phase studies (80.4% yield from phenol, Olariu et al. (2002)). From *o*-cresol, methylcatechol (m/z123) was observed. Although further reaction mechanisms of catechol species is highly uncertain, a series of signals consistent with –OH addition to catechol was observed ($C_6H_6O_2$, $C_6H_6O_3$, $C_6H_6O_4$, $C_6H_6O_5$), which could imply successive addition of –OH group to the aromatic ring. Although the absence of column separation before TOFMS may introduce adduct formation, the agreement between carbon number of major products and reactants is obvious, and hence the major signals are unlikely to be artifacts. Additionally, the agreement between off-line filter samples and on-line PILS indicates that the major signals from off-line filter analysis are not likely to be artifacts formed during filter collection.

### 2.5 Conclusions

The significance of phenolic compounds as intermediate species of aromatic SOA and possible SOA formation mechanism in the absence of $NO_x$ was investigated using the

UCR/CE-CERT Environmental Chamber. SOA formation yield measurements coupled to gas-phase yield measurements indicate that approximately 20% of the SOA of benzene, toluene, and *m*-xylene could be ascribed to the phenolic route. Initial SOA densities were as high as approximately 1.8 g/cm$^3$ and eventually reached the range of 1.3-1.4 g/cm$^3$, independent of elemental ratio (O/C) of SOA tested in this study. The major products observed by ESI/APCI-TOFMS contained the same number of carbons as parent aromatics. Major signals from on-line PILS-TOFMS and off-line filter analysis agreed, with some additional possible water soluble gas phase products observed by PILS-TOFMS such as catechol.

## 2.6 References

Aiken, A. C., DeCarlo, P. F., Kroll, J. H., Worsnop, D. R., Huffman, J. A., Docherty, K., Ulbrich, I., Mohr, C., Kimmenl, J. R., Sun, Y., Zhang, Q., Trimborn, A. M., Northway, M., Ziemann, P. J., Canagaratna, M. R., Onasch, T. B., Alfarra, M. R., Prevot, A. S., Dommen, J., Duplissy, J., Metzger, A., Baltensperger, U., Jimenez, J. L.: O/C and OM/OC ratios of primary, secondary, and ambient organic aerosols with High-Resolution Time-of-Flight Aerosol Mass Spectrometry, Environmental Science & Technology, 42, 4487-4485, 2008

Altieri, K. E., Carlton, A. G., Lim, H.-H., Turpin, B. J., Seitzinger, S. P.: Evidence for oligomer formation in clouds: Reactions of isoprene oxidation products, Environmental Science & Technology, 40, 4956-4960, 2006

Andino, J. M., Smith, J. N., Flagan, R. C., Goddard, W. A., Seinfeld, J. H.: Mechanism of atmospheric photooxidation of aromatics: A theoretical study, J. Phys. Chem., 100, 10967-10980, 1996

Arey, J., Obermeyer, G., Aschmann, S. M., Chattopadhyay, S., Cusick, R. D., Atkinson, R.: Dicarbonyl products of the OH radical-initiated reaction of a series of aromatics hydrocarbons, Environmental Science & Technology, 43, 683-689, 2009

Atkinson, R.: Kinetics and mechanisms of the gas-phase reactions of the hydroxyl radical with organic compounds, J. Phys. Chem. Ref. Data, Monograph 1, 1-246, 1989

Atkinson, R.: Atmospheric chemistry of VOCs and NOx, Atmospheric Environment, 34, 2063-2101, 2000

Atkinson, R., Aschmann, S. M., Arey, J.: Formation of ring-retaining products from the OH radical-initiated reactions of o-, m-, and p-xylene, International Journal of Chemical Kinetics, 23, 77-97, 1991

Atkinson, R., Aschmann, S. M., Carter, W. P. L., Winer, A. M., Pitts, J. N.: Alkyl nitrate formation from the NOx - air photooxications of C2-C8 n-alkanes, J. Phys. Chem., 86, 4563-4569, 1982

Bahreini, R., Keywood, M. D., Ng, N. L., Varutbangkul, V., Gao, H., Flagan, R. C., Seinfeld, J. H., Worsnop, D. R., Jimenez, J. L.: Measurements of secondary organic aerosol form oxidation of cycloalkenes, terpenes, and m-xylene using an Aerodyne Aerosol Mass Spectrometer, Environmental Science & Technology, 39(15), 5674-5688, 2005

Bateman, A. P., Nizkorodov, S. A., Laskin, J., Laskin, A.: High-resolution electospray ionization mass spectrometry analysis of water-soluble organic aerosol collected with a particle into liquid sampler, Anal. Chem., 82, 8010-8016, 2010

Bateman, A. P., Walser, M. L., Desyaterik, Y., Laskin, J., Laskin, A., Nizkorodov, S. A.: The effect of solvent on the analysis of secondary organic aerosol using electrospray ionization mass spectrometry, Environmental Science & Technology, 42, 7341-7346, 2008

Berndt, T., Böge, O.: Formation of phenol and carbonyls from the atmospheric reaction of OH radicals with benzene, Phys. Chem. Chem. Phys., 8, 1205-1214, 2006

Birdsall, A. W., Andreoni, J. F., Elrod, M. J.: Investigation of the role of bicyclic peroxy radicals in the oxidation mechanism of toluene, J. Phys. Chem., 114, 10655-10663, 2010

Birdsall, A. W., Elrod, M. J.: Comprehensive NO-Dependent Study of the Products of the Oxidation of Atmospherically Relevant Aromatic Compounds, The Journal of Physical Chemistry A, 115(21), 5397-5407, 2011

Calvert, J. G., Atkinson, R., Becker, K. H., Kamens, R. M., Seinfeld, J. H., Wallington, T. J., Yarwood, G.: The mechanism of atmospheric oxidation of aromatics hydrocarbons. New York, Oxford University Prss. 2002.

Camredon, M., Hamilton, J. F., Alam, M. S., Wyche, K. P., Carr, T., White, I. R., Monks, P. S., Rickard, A. R., Bloss, W. J.: Distribution of gaseous and particulate organic composition during dark a-pinene ozonolysis, Atmospheric Chemistry and Physics, 10, 2893-2917, 2010

Carter, W. P. L., Cocker, D. R., Fitz, D. R., Malkina, I. L., Bumiller, K., Sauer, C. G., Pisano, J. T., Bufalino, C., Song, C.: A new environmental chamber for evaluation of gas-phase chemical mechanisms and secondary aerosol formation, Atmospheric Environment, 39, 7768-7788, 2005

Chang, J. L., Thompson, A. E.: Characterization of colored products formed during irradiation of aqueous solutions containing H2O2 and phenolic compounds, Atmospheric Environment, 44, 541-551, 2010

Clark, C. C., Nakao, S., Sato, K., Qi, L., Asa-Awuku, A., Cocker, D. R., III: Chemical Characterization by Particle into Liquid Sampling Directly Coupled to an Accurate Mass Time-of-Flight Mass Spectrometer (PILS-ToFMS) of Secondary Organic Aerosol (SOA), in preparation 2011

Cocker, D. R., Flagan, R. C., Seinfeld, J. H.: State-of the art chamber facility for studying atmospheric aerosol chemistry, Environmental Science & Technology, 35(12), 2594-2601, 2001

Coeur-Tourneur, C., Cassez, A., Wenger, J. C.: Rate coefficients for the gas-phase reaction of hydroxyl radicals with 2-methoxyphenol (Guaiacol) and related compounds, J. Phys. Chem., 114, 11645-11650, 2010a

Coeur-Tourneur, C., Foulon, V., Lareal, M.: Determination of aerosol yields from 3-methylcatechol and 4-methylcatechol ozonolysis in a simulation chamber, Atmospheric Environment, 44, 853-857, 2010b

Coeur-Tourneur, C., Henry, F., Janquin, M.-A., Brutier, L.: Gas-phase reaction of hydroxyl radicals with m-, o- and p-cresol, International Journal of Chemical Kinetics, 38(9), 553-562, 2006

Davidson, C. I., Phalen, R. F., Solomon, S.: Airborne particulate matter and human health: A review, Aerosol Science and Technology, 39, 737-749, 2005

De Haan, D. O., Corrigan, A. L., Smith, K. W., Stroik, D. R., Turley, J. J., Lee, F. E., Tolbert, M. A., Jimenez, J. L., Cordova, K. E., Ferrell, G. R.: Secondary Organic Aerosol-Forming Reactions of Glyoxal with Amino Acids, Environmental Science & Technology, 43(8), 2818-2824, 2009

DeCarlo, P. F., Kimmel, J. R., Trimborn, A. M., Northway, M., Jayne, J. T., Aiken, A. C., Gonin, M., Fuhrer, K., Horvath, T., Docherty, K., Worsnop, D. R., Jimenez, J. L.: Field-deployable, high-resolution, Time-of-Flight Aerosol Mass Spectrometer, Anal. Chem., 78, 8281-8289, 2006

Docherty, K. S., Wu, W., Lim, Y. B., Ziemann, P. J.: Contributions of organic peroxides to secondary aerosol formed from reactions of monoterpenes with O3, Environmental Science & Technology, 39, 4049-4059, 2005

Ehara, K., Hagwood, C., Coakley, K. J.: Novel method to classify aerosol particles according to their mass-to-charge ratio-Aerosol particle mass analyzer, Journal of Aerosol Science, 27(2), 217-234, 1996

Eldering, A., Cass, G. R.: Source-oriented model for air pollutant effects on visibility, Journal of Geophysical Research, 101(D14), 19343-19369, 1996

Glowacki, D. R., Wang, L., Pilling, M. J.: Evidence of formation of bicyclic species in the early stages of atmospheric benzene oxidation, J. Phys. Chem. A, 113, 5385-5396, 2009

Grosjean, D.: Atmospheric reactions of ortho cresol: Gas phase and aerosol products, Atmospheric Environment, 18(8), 1641-1652, 1984

Hallquist, M., Wenger, J. C., Baltensperger, U., Rudich, Y., Simpson, D., Claeys, M., Dommen, J., Donahue, N. M., George, C., Goldstein, A. H., Hamilton, J. F., Herrmann, H., Hoffmann, T., Iinuma, Y., Jang, M., Jenkin, M., Jimenes, J. L., Kiendler-Scharr, A., Maenhaut, W., McFiggans, G., Mentel, T. F., Monod, A., Prevot, A. S., Seinfeld, J. H., Surratt, J. D., Szmigielski, R., Willdt, J.: The formation, properties and impact of secondary organic aerosol: current and emerging issues, Atmospheric Chemistry and Physics, 9, 5155-5236, 2009

Hawthorne, S. B., Krieger, M. S., Miller, D. J., Mathiason, M. B.: Collection and quantitation of methoxylated phenol tracers for atmospheric pollution from residential wood stoves, Environmental Science & Technology, 23(4), 470-475, 1989

Hawthorne, S. B., Miller, D. J., Langenfeld, J. J., Krieger, M. S.: PM-10 high-volume collection and quantitation of semi- and nonvolatile phenols, methoxylated phenols, alkanes, and polycyclilc aromatic hydrocarbons from winter urban air and their relationship to wood smoke emissions, Environmental Science & Technology, 26, 2251-2262, 1992

Heaton, K. J., Sleighter, R. L., Hatcher, P. G., Hall, W. A., Johnston, M. V.: Composition domains in monoterpene secondary organic aerosol, Environmental Science & Technology, 43, 7797-7802, 2009

Henry, F., Coeur-Tourneur, C., Ledoux, F., Tomas, A., Menu, D.: Secondary organic aerosol formation from the gas phase reaction of hydroxyl radicals with m-, o- and p-cresol, Atmospheric Environment, 42, 3035-3045, 2008

Huang, M., Zhang, W., Wang, Z., Hao, L., Zhao, W., Liu, X., Long, B., Fang, L.: Theoretical investigation on the detailed mechanism of the OH-initiated atmospheric photooxidation of o-xylene, International Journal of Quantum Chemistry, 108, 954-966, 2008

Hurley, M. D., Sokolov, O., Wallington, T. J., Takekawa, H., Karasawa, M., Klotz, B.: Organic aerosol formation during the atmospheric degradation of toluene, Environmental Science & Technology, 35(7), 1358-1366, 2001

Iinuma, Y., Boge, O., Grafe, R., Herrmann, F.: Methyl-nitrocatechols: Atmospheric tracer compounds for biomass burning secondary organic aerosols, Environmental Science & Technology, 44, 8453-8459, 2010

IPCC (2007). Intergovernmental Panel on Climate Change: Climate Change 2007: The Physical Science
Basis, Cambridge University Press, UK.

Johnson, D., Jenkin, M., Wirtz, K., Martin-Reviejo, M.: Simulating the formation of secondary organic aerosol from the photooxidation of toluene, Environ. Chem., 1, 150-165, 2004

Johnson, D., Jenkin, M. E., Wirtz, K., Martin-Reviejo, M.: Simulating the formation of secondary organic aerosol from the photooxidation of aromatics hydrocarbons, Environ. Chem., 2, 35-48, 2005

Kanakidou, M., Seinfeld, J. H., Pandis, S. N., Barnes, I., Dentener, F. J., Facchini, M. C., Van Dingenen, R., Ervens, B., Nenes, A., Nielsen, C. J., Swietlicki, E., Putaud, J. P., Balkanski, Y., Wilson, J.: Organic aerosol and global climate modelling: a review, Atmospheric Chemistry and Physics, 5, 1053-1123, 2005

Kautzman, K. E., Surratt, J. D., Chan, M. N., Chan, A. W. H., Hersey, S. P., Chhabra, P. S., Dalleska, N. F., Wennberg, P. O., Flagan, R. C., Seinfeld, J. H.: Chemical composition of gas- and aerosol-phase products from the photooxidation of naphthalene, J. Phys. Chem., 114, 913-934, 2010

Khalizov, A. F., Zhang, R., Zhang, D., Xue, H., Pagels, J., McMurry, P. H.: Formation of highly hygroscopic soot aerosols upon internal mixing with sulfuric acid vapor, Journal of Geophysical Research, 114, D05208, doi: 10.1029/2008JD010595, 2009

Klotz, B., Sorensen, S., Barnes, I., Becker, K. H., Etzkorn, T., Volkamer, R., Platt, U., Wirtz, K., Martin-Reviejo, M.: Atmospheric oxidation of toluene in a large-volume outdoor photoreactor: In situ determination of ring-retaining product yields, J. Phys. Chem. A, 102, 10289-10299, 1998

Malloy, Q., Nakao, S., Qi, L., Austin, R. L., Stothers, C., Hagino, H., Cocker, D. R.: Real-time aerosol density determination utilizing a modified Scanning Mobility Particle Sizer - Aerosol Particle Mass Analyzer system, Aerosol Science and Technology, 43, 673-678, 2009

McMurry, P. H., Wang, X. W., Park, K., Ehara, K.: The relationship between mass and mobility for atmospheric particles: A new technique for measuring particle density, Aerosol Science and Technology, 36, 227-238, 2002

Nakao, S., Shrivastava, M., Nguyen, A., Jung, H., Cocker, D.: Interpretation of Secondary Organic Aerosol Formation from Diesel Exhaust Photooxidation in an Environmental Chamber, Aerosol Science and Technology, 45(8), 954-962, 2011

Ng, N. L., Kroll, J. H., Chan, A. W. H., Chhabra, P., Flagan, R. C., Seinfeld, J. H.: Secondary organic aerosol formation from m-xylene, toluene, and benzene, Atmospheric Chemistry and Physics, 7, 3909-3922, 2007

Odum, J. R., Hoffman, T., Bowman, F., Collins, D., Flagan, R. C., Seinfeld, J. H.: Gas/particle partitioning and secondary organic aerosol yields, Environmental Science & Technology, 30(8), 2580-2585, 1996

Olariu, R. I., Klotz, B., Barnes, I., Becker, K. H., Mocanu, R.: FT-IR study of the ring-retaining products from the reaction of OH radicals with phenol, o-, m-, and p-cresol, Atmospheric Environment, 36, 3685-3697, 2002

Orsini, D. A., Ma, Y., Sullivan, A., Sierau, B., Baumann, K., Weber, R. J.: Refinements to the particle-into-liquid sampler (PILS) for ground and airborne measurements of water soluble aerosol composition, Atmospheric Environment, 37, 1243-1259, 2003

Pope, C. A., Dockery, D. W.: Health effects of fine particulate air pollution: Lines that connect, J. Air & Waste Manage. Assoc., 56, 709-742, 2006

Pratt, K. A., Prather, K. A.: Mass spectrometry of atmospheric aerosols—recent developments and applications. Part I: Off-line mass spectrometry techniques, Mass Spectrometry Reviews, DOI 10.1002/mas.20322 2011

Reinnig, M.-C., Müller, L., Warnke, J., Hoffmann, T.: Characterization of selected organic compound classes in secondary organic aerosol from biogenic VOCs by HPLC/MSn, Analytical and Bioanalytical Chemistry, 391(1), 171-182-182, 2008

Sato, K., Hatakeyama, S., Imamura, T.: Secondary organic aerosol formation during the photooxidation of toluene: NOx dependence of chemical composition, J. Phys. Chem. A, 111, 9796-9808, 2007

Sato, K., Takami, A., Isozaki, T., Hikida, T., Shimono, A., Imamura, T.: Mass spectrometric study of secondary organic aerosol formed from the photo-oxidation of aromatic hydrocarbons, Atmospheric Environment, 44, 1080-1087, 2010

Schauer, J. J., Kleeman, M. J., Cass, G. R., Simoneit, B. R. T.: Measurement of emissions from air pollution sources. 3. C1-C29 organic compounds from fireplace combustion of wood, Environmental Science & Technology, 35, 1716-1728, 2001

Simoneit, B. R. T.: A review of biomarker compounds as source indicators and tracers for air pollution, Environ. Sci. & Pllut. Res., 6(3), 159-169, 1999

Smith, D. F., Kleindienst, T. E., McIver, C. D.: Primary product distributions from the reaction of OH with m-, p-xylene, 1,2,4- and 1,3,5-trimethylbenzene, Journal of Atmospheric Chemistry, 34, 339-364, 1999

Smith, D. F., McIver, C. D., Kleindienst, T. E.: Primary product distribution from the reaction of hydroxyl radicals with toluene at ppb NOx mixing ratios, Journal of Atmospheric Chemistry, 30, 209-228, 1998

Sun, Y. L., Zhang, Q., Anastasio, C., Sun, J.: Insights into secondary organic aerosol formed via aqueous-phase reactions of phenolic compounds based on high resolution mass spectrometry, Atmospheric Chemistry and Physics, 10, 4809-4822, 2010

Surratt, J. D., Murphy, S. M., Kroll, J. H., Ng, N. L., Hildebrandt, L., Sorooshian, A., Szmigielski, R., Vermeylen, R., Maenhaut, W., Claeys, M., Flagan, R. C., Seinfeld, J. H.: Chemical composition of secondary organic aerosol formed from the photooxidation of isoprene, J. Phys. Chem. A, 110, 9665-9690, 2006

Takekawa, H., Minoura, H., Yamazaki, S.: Temperature dependence of secondary organic aerosol formation by photo-oxidation of hydrocarbons, Atmospheric Environment, 37, 3413-3424, 2003

Volkamer, R., Klotz, B., Barnes, I., Imamura, T., Washida, N.: OH-initiated oxidation of benzene Part 1. Phenol formation under atmospheric conditions, Phys. Chem. Chem. Phys., 4, 1598-1610, 2002
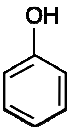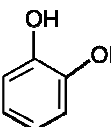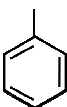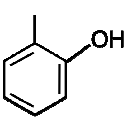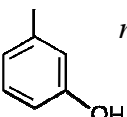
Weber, R. J., Orsini, D. A., Daun, Y., Lee, Y.-N., Klotz, P. J., Brechtel, F.: A particle-into-liquid collector for rapid measurement of aerosol bulk chemical composition, Aerosol Science and Technology, 35, 718-727, 2001
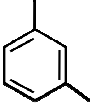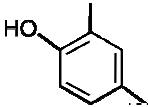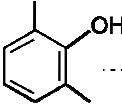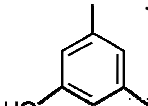
Wyche, K. P., Monks, P. S., Ellis, A. M., Cordell, R. L., Parker, A. E., Whyte, C., Metzger, A., Dommen, J., Duplissy, J., Prevot, A. S., Baltensperger, U., Rickard, A. R., Wulfert, F.: Gas phase precursors to anthropogenic secondary organic aerosol: detailed observations of 1,3,5-trimethylbenzene photooxidation, Atmospheric Chemistry and Physics, 9, 635-665, 2009

Xue, H., Khalizov, A. F., Wang, L., Zheng, J., Zhang, R.: Effects of coating of dicarboxylic acids on the mass-mobility relationship of soot particles, Environmental Science & Technology, 43, 2787-2792, 2009

## 2.7 Tables

Table 2.1 Experimental test matrix (low NOx)

| Run ID | $HC_i$ (ppb) | $HC_f$ (ppb) | $\Delta HC$ ($\mu g/m^3$) | $M_o$ ($\mu m^3/cm^3$) | SOA yield[c] |
|---|---|---|---|---|---|
| *benzene + $H_2O_2$* | | | | | |
| EPA1141A | 491 | 434 | 182 | 25 | 0.19 |
| EPA1149A | 490 | 429 | 195 | 26 | 0.18 |
| EPA1161A | 1031 | 929 | 326 | 64 | 0.28 |
| EPA1161B | 528 | 478 | 160 | 21 | 0.19 |
| EPA1225A | 953 | 833 | 383 | 73 | 0.27 |
| EPA1225B | 959 | 882 | 246 | 36 | 0.20 |
| *phenol + $H_2O_2$* | | | | | |
| EPA1206A | 51 | 21 | 115 | 35 | 0.43 |
| EPA1206B | 52 | 20 | 122 | 40 | 0.45 |
| EPA1217A | 138 | 49 | 338 | 96 | 0.40 |
| EPA1217B | 76 | 28 | 184 | 51 | 0.38 |
| *catechol+ $H_2O_2$* | | | | | |
| EPA1293A | 71[a] | 0 | 318 | 89 | 0.39 |
| *toluene + $H_2O_2$* | | | | | |
| EPA1266A | 104 | 77 | 100 | 12 | 0.17 |
| EPA1251B | 84 | 59 | 93 | 12 | 0.19 |
| EPA1141B | 85 | 57 | 108 | 15 | 0.20 |
| EPA1290B | 432 | 326 | 397 | 65 | 0.23 |
| *o-cresol+ $H_2O_2$* | | | | | |
| EPA1251A | 75 | 27 | 210 | 74 | 0.49 |
| EPA1252A | 54 | 12 | 184 | 52 | 0.39 |
| EPA1252B | 45 | 8 | 166 | 41 | 0.35 |
| EPA1266B | 101 | 41 | 263 | 87 | 0.46 |
| EPA1427A | 105 | 29 | 333 | 101 | 0.43 |
| *m-cresol+ $H_2O_2$* | | | | | |
| EPA1255A | 67 | 18 | 212 | 41 | 0.27 |
| EPA1255B | 55 | 16 | 174 | 38 | 0.31 |
| *m-xylene + $H_2O_2$* | | | | | |

|  | | | | | |
|---|---|---|---|---|---|
| EPA1244A | 124 | 47 | 333 | 57 | 0.24 |
| EPA1180B | 234 | 90 | 621 | 134 | 0.30 |
| EPA1209A | 229 | 77 | 656 | 126 | 0.27 |
| EPA1209B | 177 | 59 | 509 | 95 | 0.26 |
| EPA1212A | 114 | 21 | 401 | 91 | 0.32 |
| EPA1212B | 52 | 6 | 197 | 45 | 0.32 |
| EPA1248A | 315 | 262 | 229 | 16 | 0.10 |
| EPA1248B | 121 | 48 | 318 | 48 | 0.21 |

*2,4-DMP + $H_2O_2$*

| EPA1238A | 83 | 6 | 381 | 199 | 0.73 |
|---|---|---|---|---|---|
| EPA1238B | 62 | 2 | 293 | 140 | 0.67 |
| EPA1412A | 184 | 41 | 710 | 340 | 0.67 |

mezzanine chamber runs[b]

| mez100809 | 68 | 2.2 | 327 | 222 | 0.95 |
|---|---|---|---|---|---|
| mez100909 | 131 | 4.9 | 628 | 331 | 0.74 |
| mez101009 | 48 | 1 | 234 | 108 | 0.65 |
| mez101109 | 72 | 2 | 349 | 155 | 0.62 |
| mez101309 | 77 | 1.9 | 373 | 197 | 0.74 |
| mez102109 | 66 | 1 | 322 | 162 | 0.70 |

*2,6-DMP + $H_2O_2$*

| EPA1240A | 98 | 6 | 457 | 134 | 0.41 |
|---|---|---|---|---|---|
| EPA1240B | 58 | 2 | 278 | 75 | 0.38 |

mezzanine chamber runs[b]

| mez081409 | 64 | 0 | 319 | 79 | 0.35 |
|---|---|---|---|---|---|
| mez081609 | 66 | 0 | 327 | 86 | 0.37 |
| mez081809 | 67 | 16 | 255 | 24 | 0.13 |
| mez100609 | 64 | 2.8 | 305 | 95 | 0.44 |
| mez100709 | 130 | 2.7 | 632 | 196 | 0.43 |
| mez120309 | 125 | 0 | 621 | 149 | 0.34 |
| mez120409 | 96 | 0 | 478 | 124 | 0.36 |

*3,5-DMP + $H_2O_2$*

| EPA1243A | 90 | 9 | 400 | 83 | 0.29 |
|---|---|---|---|---|---|
| EPA1243B | 60 | 7 | 262 | 33 | 0.17 |

mezzanine chamber runs[b]

| mez051910 | 72.24 | 0 | 359 | 61 | 0.24 |
|---|---|---|---|---|---|
| mez052010 | 85.09 | 0 | 422 | 75 | 0.25 |
| mez052310 | 154.1 | 0 | 765 | 148 | 0.27 |
| mez060210 | 160.5 | 0 | 797 | 174 | 0.31 |

a) Initial concentration calculated by amount injected. Injection done with oven temperature ~ 120°C.
b) Initial DMPs concentrations calculated based on injection. Final concentration obtained
 by the PTR-MS.
c) yields calculated using SOA density 1.4g/cm³

Table 2.2 Phenolic formation yield from OH reaction with benzene, toluene, and *m*-xylene

|  | Phenolic formation yield (%) | | $NO_x$ (ppm) |
|---|---|---|---|
|  | Phenol | | |
| This study | 41.3 | | 0 |
| Berndt and Böge (2006) | $61 \pm 6$ | | 0 |
| Volkamer et al. (2002) | $53.1 \pm 6$ | | 0.002-2 |
|  | *o*-Cresol | (*m+p*)-Cresol | |
| This study | 15.8 | 7.3 | 0 |
| Atkinson et al. (1989) | $20.4 \pm 2.7$ | $4.8 \pm 0.9$ | 0-10 |
| Klotz et al. (1998) | $12.0 \pm 1.4$ | $5.9 \pm 0.9$ | 0.003-0.3 |
| Smith et al. (1998) | $12.3 \pm 0.6$ | $5.6 \pm 0.4$ | 0.10-0.42 |
|  | (2,4 + 2,6 + 3,5)-DMP | | |
| This study* | $8.2 \pm 1.3$ | | 0 |
| Smith et al. (1999) | $10.9 \pm 0.5$ | | 0.157-1.081 |
| Atkinson et al. (1991) | $21.0 \pm 5.6$ | | 0-10 |
| Noda et al. (2009) | $14.1 \pm 2.6$ | | 0.01-0.1 |

*acquired in mezzanine chamber using PTR-MS

Table 2.3 Estimated contribution of phenolic route to benzene, toluene, and *m*-xylene SOA.

|  | Benzene | Toluene | *m*-Xylene |
|---|---|---|---|
| Phenolic route (%) | 23.5 ± 4.7* | 15.8 ± 3.8* | 16.9 ± 3.4 (n=4) |

*Error estimated based on repeated m-xylene experiments and phenolic route calculations

## 2.8   Figures
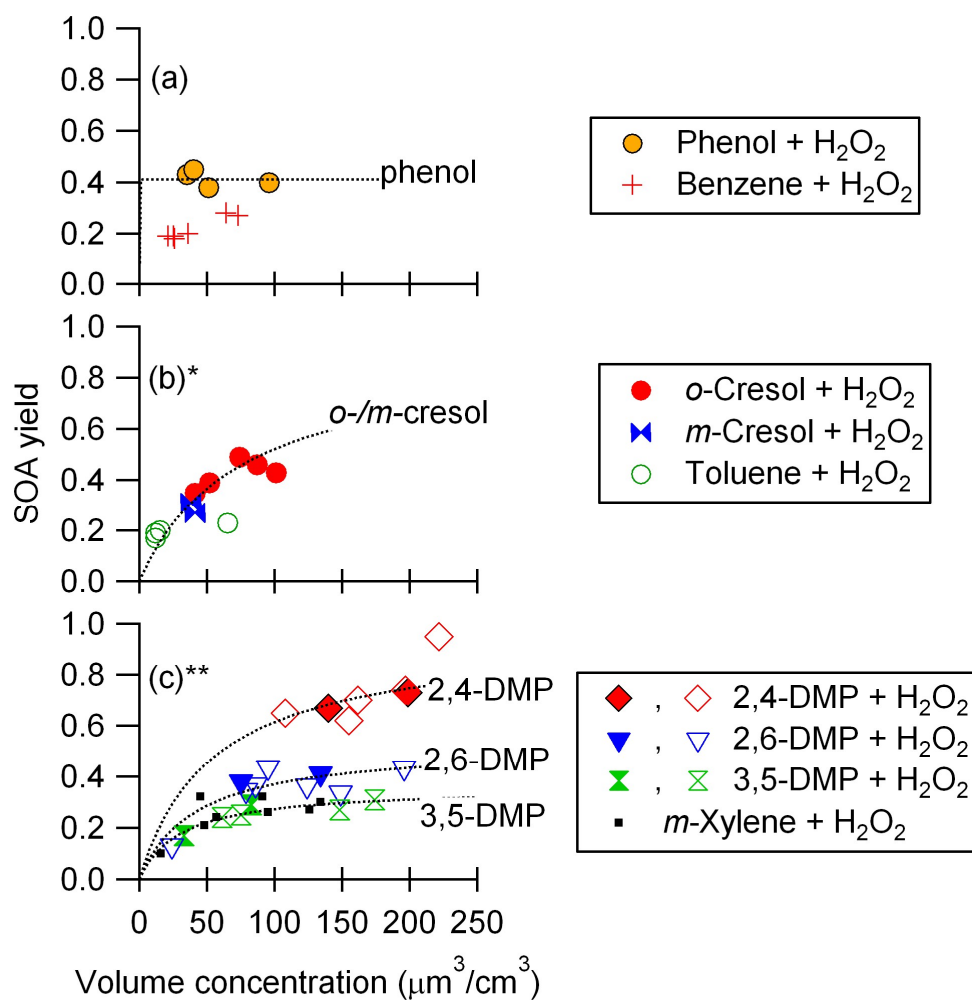


Figure 2.1 SOA yield of benzene, toluene, m-xylene, and their phenolic compounds in the absence of NOx (Dotted lines are one product model fit for phenolic compounds).
* SOA yields from cresols isomers are combined.
** Open symbols are data acquired in CE-CERT mezzanine chamber
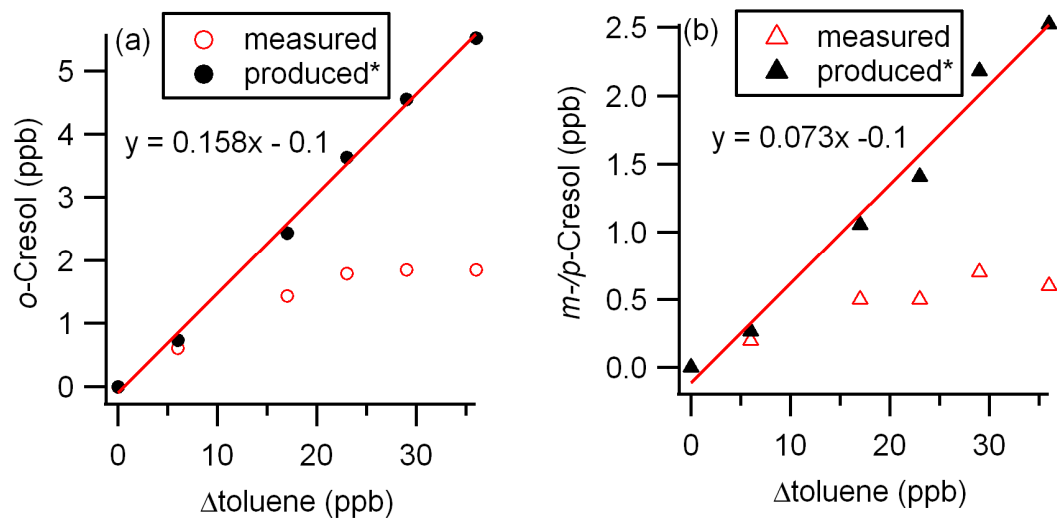
Figure 2.2 Formation of cresols from OH reaction with toluene.
*measured cresol concentrations were corrected for secondary reaction

40
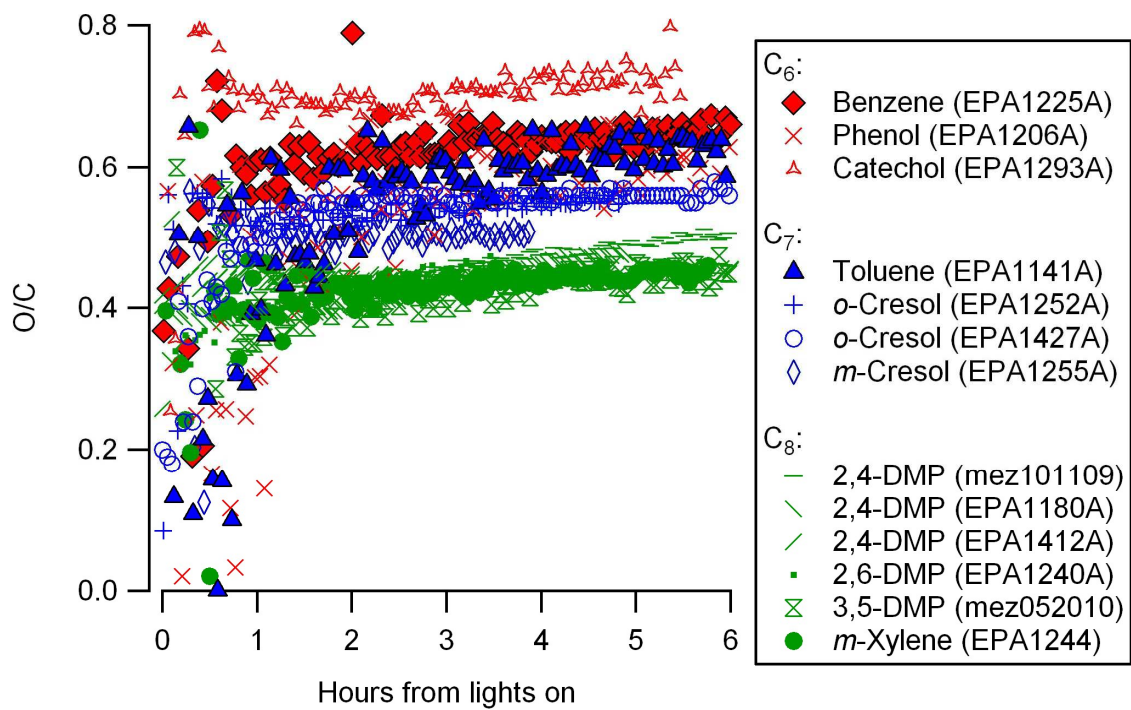
Figure 2.3 Time series of the O/C ratio of SOA formed from aromatic hydrocarbons and phenolic compounds
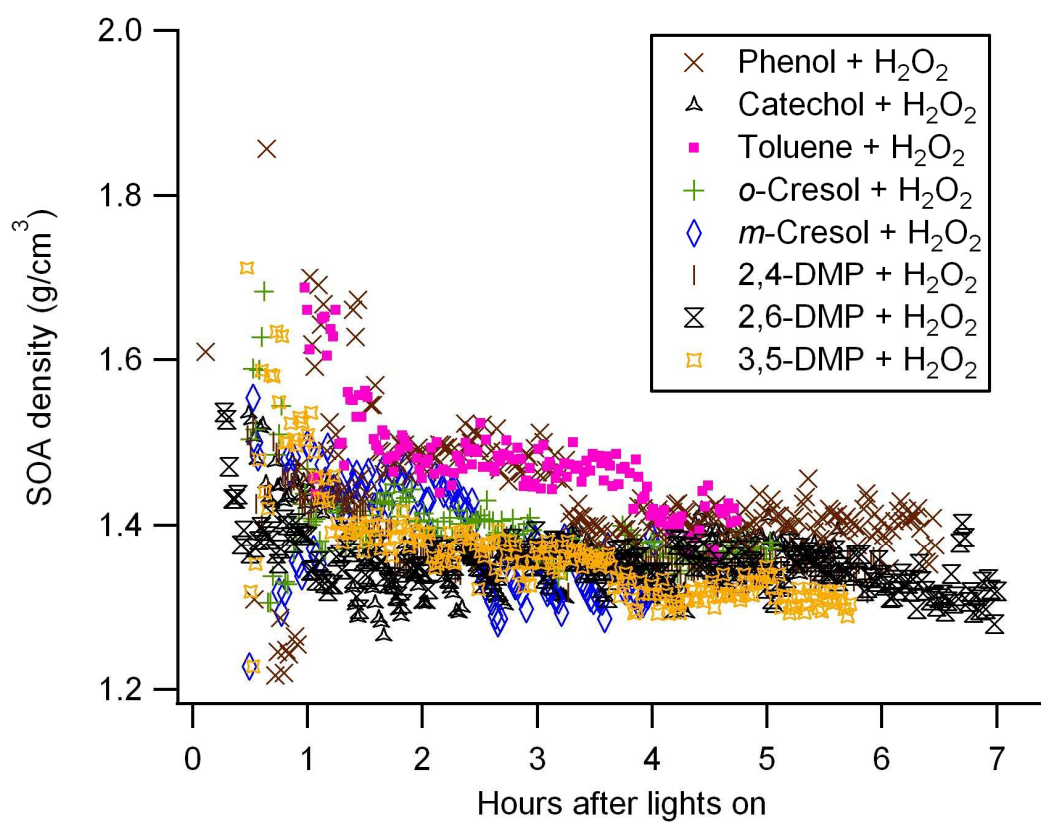
Figure 2.4 Time series of the density of SOA formed from aromatic hydrocarbons and phenolic compounds
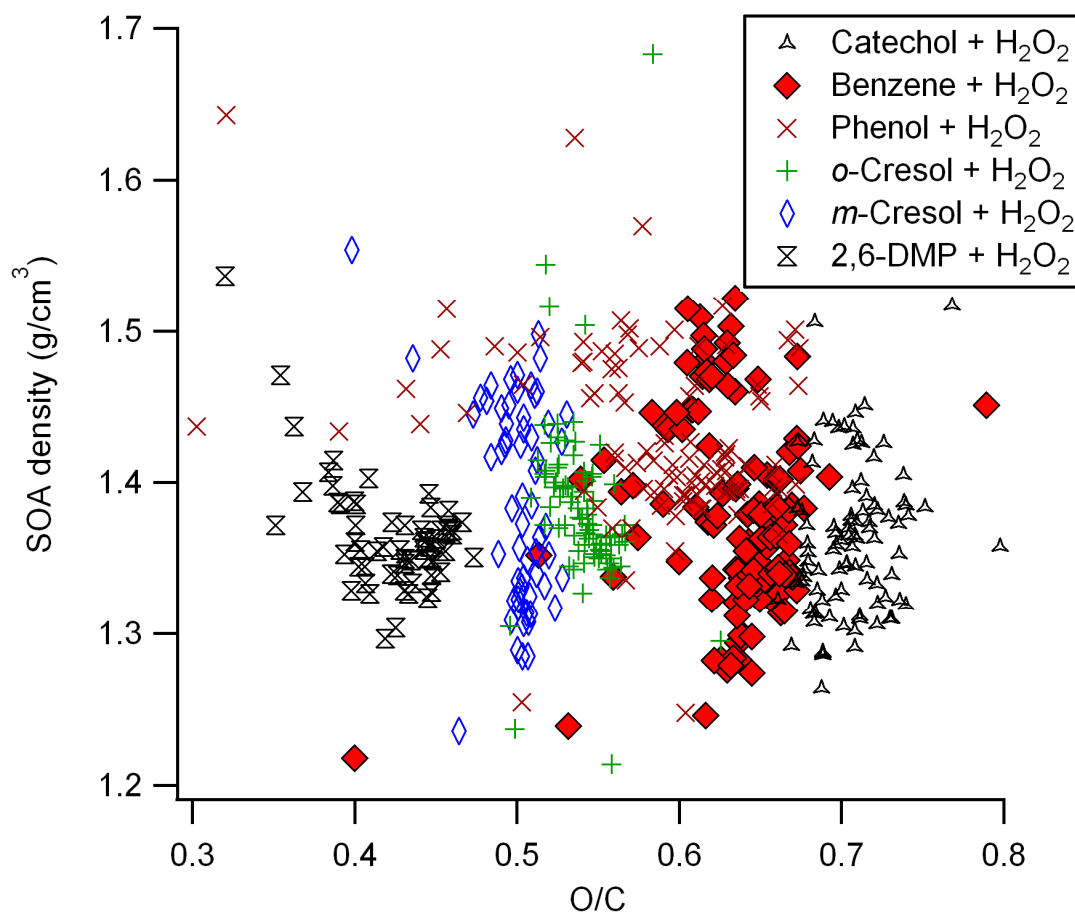
Figure 2.5 The relationship between density and elemental compositions of SOA formed from aromatic hydrocarbons and phenolic compounds
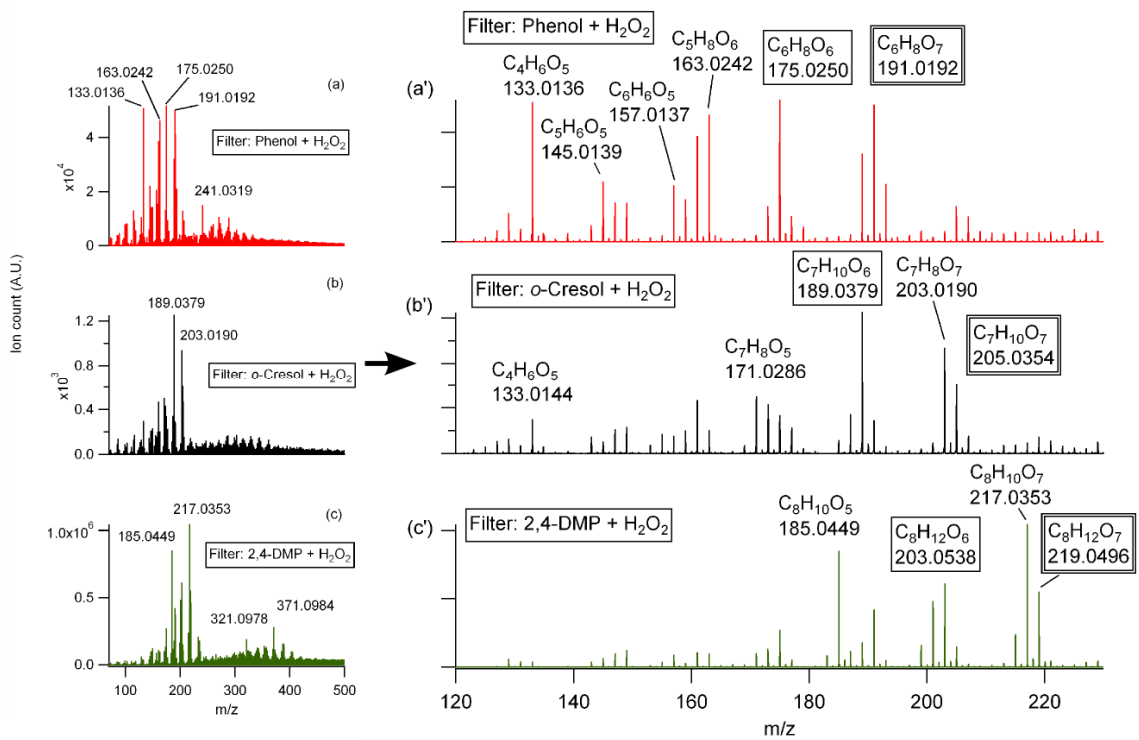
Figure 2.6 ESI/APCI-ToF mass spectrums of SOA formed by OH reaction with phenolic compounds
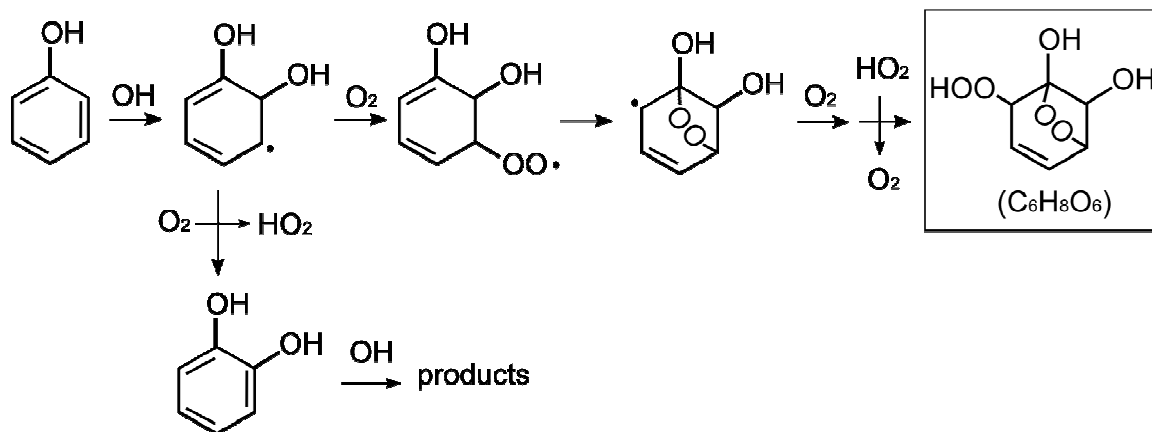
Figure 2.7 Possible formation pathway of a bicyclic hedroperoxide (C6H8O6) from OH reaction with phenol in the absence of NOx inferred from aromatics oxidation mechanisms
 (e.g., Calvert et al., 2002; Johnson et al., 2005). Catechol formation from phenol is reported to be approximately 80% (Olariu et al., 2002).
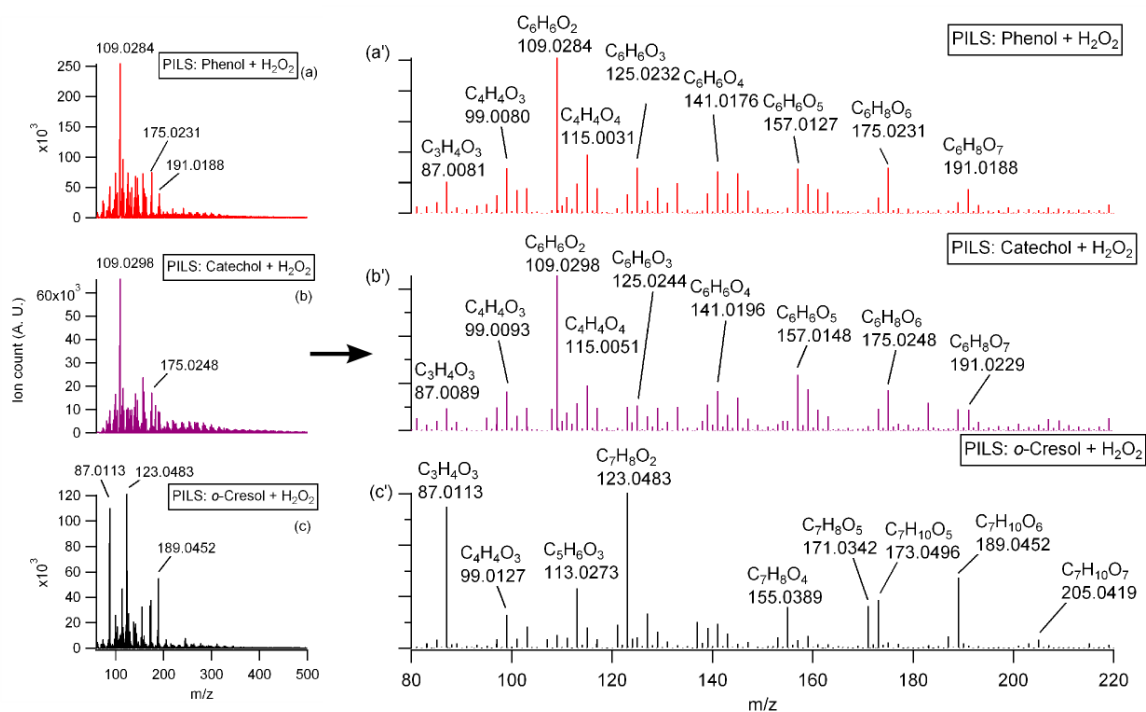
Figure 2.8 PILS-ESI-ToF mass spectrums of SOA formed by OH reaction with phenolic compounds
 (The spectrum for phenol (a) and catechol (b) is taken when SOA concentration was highest. For *o*-cresol (c), spectrum at highest $C_7H_8O_2$ is shown.)

## 3 Chamber studies of SOA formation from aromatic hydrocarbons: observation of limited glyoxal uptake

### 3.1 Introduction

Aerosol contributes to climate change and adversely affects air quality (Finlayson-Pitts and Pitts, 1999; Seinfeld and Pandis, 2006). Secondary organic aerosol (SOA) is formed from oxidative processing of volatile organic compounds in the atmosphere. Previous researchers have estimated approximately 70% of organic aerosols are secondary in nature (Hallquist et al., 2009 and references therein). Traditionally, SOA formation is described solely by gas-to-particle partitioning of semi-volatile oxidation products of volatile organic compounds (VOCs) (Odum et al., 1996; Pankow, 1994). However, recent works have observed enhanced SOA formation from the oligomerization of volatile species (Kalberer et al., 2004; Tolocka et al., 2004).

Glyoxal was previously ignored as a SOA precursor due to its high vapor pressure (6 orders of magnitude too high (Volkamer et al., 2007)); however, the current view is that glyoxal can contribute to SOA formation by uptake into water (cloud, fog, and wet aerosols) followed by radical and non-radical reactions to produce low volatility products (Lim et al., 2010 and references therein). The global emission of glyoxal is estimated to be 45 Tg/yr (Fu et al., 2008); globally, the major precursor of glyoxal is isoprene (21

Tg/yr) (Fu et al., 2008), while aromatic hydrocarbons are the main precursors in urban areas (e.g., 70~79% in Mexico City (Volkamer et al., 2007)).

The liquid water content of typical cloud droplets are orders of magnitude higher than that of aerosols (Seinfeld and Pandis, 2006); therefore, early work on glyoxal SOA formation focused on aqueous reactions in cloud and fog water (e.g., Ervens et al., 2004). However, SOA formation from glyoxal uptake onto wet aerosols has attracted increasing attention during the last few years. Volkamer et al. (2007) observed significantly lower glyoxal concentration than model predictions for Mexico City, indicating a large missing sink of glyoxal. The discrepancy was resolved by introducing glyoxal uptake onto aerosols; ~15% of the SOA formation in Mexico City was attributed to glyoxal uptake onto aerosols (Volkamer et al., 2007). Additionally, recent laboratory studies suggest formation of SOA via oligomerization of glyoxal in aerosol aqueous phase (Corrigan et al., 2008; Galloway et al., 2009; Galloway et al., 2011; Kroll et al., 2005; Liggio et al., 2005b; Volkamer et al., 2009).

Glyoxal uptake onto particles is observed to be strongly dependent on seed composition. Acidity is suggested to enhance glyoxal partitioning to the aqueous phase (Jang and Kamens, 2001). However, Kroll et al. (2005) did not observe the acidity effect; instead they suggested that ionic strength of the seed aerosols ("salting in") could explain the enhanced glyoxal uptake onto aqueous ammonium sulfate seeds (by a factor of ~70 compared to uptake by water). A more recent work by Ip et al. (2009) suggested that

sulfate was a more important factor than ionic strength in affecting glyoxal's Henry's law constant. Organic seeds are also reported to enhance glyoxal uptake (e.g., Volkamer et al. (2009): fulvic acid, humic acid sodium salt, and amino acids; Corrigan et al. (2008): amino acids and carboxylic acids). However, understanding of the composition of SOA formed from aromatic hydrocarbon oxidation is currently limited; typically only less than ~10% of aromatic SOA composition is identified (Cocker et al., 2001b; Hamilton et al., 2005; Sato et al., 2007). Therefore, the impact of organic aerosol on glyoxal uptake is highly uncertain.

Glyoxal is a major product of aromatic hydrocarbon photooxidation (e.g., 8~24% from toluene-$NO_x$ photooxidation, Calvert et al. (2002)). Aromatic hydrocarbons comprise ~20% of nonmethane hydrocarbons in the urban atmosphere and are considered to be one of the major precursors to urban SOA (Calvert et al., 2002). A large number of studies have investigated gas-phase photooxidation of aromatic hydrocarbons (e.g., Arey et al., 2009; Birdsall et al., 2010; Calvert et al., 2002 and references therein; Coeur-Tourneur et al., 2006; Johnson et al., 2004; Johnson et al., 2005; Olariu et al., 2002; Takekawa et al., 2003; Volkamer et al., 2002). Although multigenerational reactions have been suggested to contribute to aromatic SOA formation (Hurley et al., 2001; Nakao et al., 2011a; Ng et al., 2007; Sato et al., 2007), the extent of the contribution from second or later generation products to SOA is poorly understood. Based on previous studies on SOA formation by glyoxal uptake, glyoxal oligomerization has been inferred to be a substantial intermediate reaction in SOA formation from aromatic hydrocarbon under humid conditions (Kalberer

et al., 2004; Kamens et al., 2011; Zhou et al., 2011). According to previous studies on glyoxal uptake, glyoxal is expected to partition to aqueous phase of SOA and subsequently undergo free-radical initiated and various condensation reactions to produce low-volatility products. However, the applicability of these previous studies of relatively pure systems (wet inorganic/organic seed) to complex aromatic SOA system remains uncertain. The aim of this work is to shed light on the role of glyoxal in SOA formation from aromatic hydrocarbon oxidation – specifically as an OH radical source or an oligomer precursor.

## 3.2  Experimental

### 3.2.1  Environmental chamber

The experiments were conducted in the UC Riverside/CE-CERT environmental chamber described in detail in Carter et al. (2005). In short, this facility consists of dual 90 m$^3$ Teflon® reactors suspended by rigid frames in a temperature controlled enclosure (27 ± 1 °C) continuously flushed with dry (a dew point below -40 °C) purified air generated by an Aadco 737 series (Cleves, Ohio) air purification system. The top frames are slowly lowered during the experiments to maintain a slight positive differential pressure (~7.5 Pa) between the reactors and the enclosure, to minimize dilution and possible contamination of the reactors. Black lights (272 bulbs, 115 W Sylvania 350BL, NO$_2$ photolysis rate 0.4 min$^{-1}$) are used as the light source for all the experiments reported herein.

### 3.2.2 Chemicals

NO (UHP grade, Matheson) was used for $NO_x$ photooxidation experiments. The following chemicals were all purchased from Sigma-Aldrich: toluene (>99.5%), 2-tert-butylphenol (>99%), perfluorohexane (>99%), $H_2O_2$ (50wt% solution in water), glyoxal trimer dihydrate (>95%), $P_2O_5$ (>98%), glyoxal water solution (40wt%), hexanedioic acid (>99.5%), decanedioic acid (>99), and ammonium sulfate (>99%).

### 3.2.3 Gas analysis

Glyoxal was measured by a custom-built, incoherent broadband Cavity Enhanced Absorption Spectrometer (CEAS) (Langridge et al., 2006; Washenfelder et al., 2008). In CEAS, a continuous wave incoherent light is injected into a cavity, where the intensity reaches its limiting value and absorption spectra are obtained (Engeln et al., 1998). The absorption coefficient is obtained from (Fiedler et al., 2005)

$$\alpha(\lambda) = \frac{1}{d}\left(\frac{I_0(\lambda)}{I(\lambda)} - 1\right)(1 - R(\lambda))$$

Eq. 1

where $\alpha$ is the absorption coefficient, d is the length of the cavity, $I_0$ is the intensity of light exiting the cavity without any absorber present, I is the light intensity of the cavity with absorber, and R is the reflectivity of the mirrors. In CEAS, the transmitted light intensity through the optical cavity of two high reflectivity mirrors provides sensitive measurements of trace species with a long effective optical path (Engeln et al., 1998; Fiedler, 2003; Langridge et al., 2006; Paul, 2001; Washenfelder, 2008). CEAS

allows for simultaneous analysis of multiple absorbers in the same spectral region (e.g., both $NO_2$ and glyoxal in the 440 – 460 nm region).

In this work, the CEAS system for the glyoxal measurements was based on the previous work by Langridge et al. (2006) and Washenfelder et al. (2008). The major components of the CEAS system include a glass cell housing the optical cavity (65 cm long, 2.54 cm diameter with 1/16 inch wall thickness), two high reflectivity (R=0.9998) mirrors (Los Gatos), a light emitting diode (LED) (Luxeon) light source, a monochromator and a charge-coupled device (CCD) light detector (Andor). The light from the LED was focused and coupled into the optical cavity; the output light from the cavity was dispersed by the monochromator and collected by the CCD detector. Gas flow rate through the CEAS was 1 LPM, while the pressure inside the optical cavity ranged from 714-720 Torr (0.939-0.947 atm). The CCD collected the transmission spectra from the cavity using an exposure time of 0.5 second, with 112 samples accumulated during an overall sampling time of 1 minute. The 0.5 second exposure time was chosen to prevent saturation of the signal at the peak LED emission spectrum at the maximum operating power of 200 mW for this CEAS system. The background signal, under the same acquisition conditions, was collected with the LED off and the background spectra was subtracted from the transmission spectra from the cavity.

The glyoxal number density was calculated from

$$\alpha(\lambda) = b_0 + b_1 \cdot \lambda + b_2 \cdot \lambda^2 + b_3 \cdot \lambda^3 + \sigma_{NO_2}(\lambda) \cdot n_{NO_2} + \sigma_{gly}(\lambda) \cdot n_{gly} \qquad \text{Eq.2}$$

where $\lambda$ is the wavelength, $\sigma_{gly}$ is glyoxal absorption cross-section, $n_{gly}$ is the glyoxal number density, $\alpha(\lambda)$ is the measured absorption coefficient for a given $\lambda$, the polynomial terms of the equation account for light extinction by background molecules (e.g., $N_2$ and $O_2$), and $\sigma_{NO_2}$ and $n_{NO_2}$ account for light absorption by $NO_2$. Wavelength-dependent absorption cross-sections ($\sigma(\lambda)$) were obtained from literature and data evaluation web sites (e.g., IUPAC, 2006, NASA, 2006, and Volkamer et al. (2005)). The glyoxal number densities were extracted using the spectra between 446.5 and 450.0 nm.

The Agilent 6890 Gas Chromatograph – Flame Ionization Detector was used to measure concentrations of parent hydrocarbons (toluene and 2-tert-butylphenol) and an inert tracer (perfluorohexane). A GS-Alumina column (30 m x 0.53 mm) and a DB-5 column (30 m x 0.53 mm) were used for perfluorohexane and toluene analysis, respectively. 2-tert-butylphenol was collected on a sorbent tube packed with Tenax-TA/Carbopack/Carbosive (CDS Analytical, Inc, MX062171) and was thermally desorbed at 290°C (CDS Analytical, Inc, ACEM9305) onto a Restek® Rtx-35 Amine (30m x 0.53 mm ID, 1.00 micron) column. Toluene measurements were calibrated using a dilute gas cylinder (SCOTT-MARIN, Inc); perfluorohexane was calibrated by introducing a known amount of the liquid into the reactor; and 2-tert-butylphenol was calibrated by impregnation of the glass tube and subsequent thermal desorption.

### 3.2.4 Particle analysis

Particle size distribution between 27 nm and 686 nm was monitored by a custom built

Scanning Mobility Particle Sizer (SMPS) similar to that described by Cocker et al.

(2001a). The chemical evolution of organic particulate matter was observed by a high-

resolution time-of-flight aerosol mass spectrometer (HR-ToF-AMS) (DeCarlo et al.,

2006; Jayne et al., 2000). The HR-ToF-AMS operation was alternated between the high

resolution W-mode and high sensitivity V-mode. The high resolution capability allowed

determination of molecular formula of ion fragments of SOA (e.g., $C_4H_9^+$). SQUIRREL

v1.49 and PIKA v1.08 were used for data analysis. The default fragmentation table was

used without modification. Particle volatility was monitored with a volatility tandem

differential mobility analyzer (VTDMA) (Nakao et al., 2011b; Qi et al., 2010b; Rader

and McMurry, 1986), in which monodisperse particles of mobility diameter $D_{mi}$ were

selected by the 1st differential mobility analyzer (DMA) followed by transport through a

Dekati thermodenuder (TD, residence time: ~17 s, typically at 100$^\circ$C). The particle size

after the TD ($D_{mf}$) was then measured by fitting a log-normal size distribution curve

acquired by the 2nd DMA. Volume fraction remaining (VFR) was calculated by taking a

(cubed) ratio of particle mobility diameter after the TD ($D_{mf}$) to initial particle size ($D_{mi}$),

i.e., VFR = $(D_{mf}/D_{mi})^3$. $D_{mi}$ was adjusted during the experiment according to mode

diameters of particle size distribution within the environmental chamber to maximize the

signal-to-noise ratio (typically $D_{mi}$ = 50~150nm). Particle hygroscopicity as a function of

RH was monitored with a hygroscopicity TDMA (HTDMA) (Cocker et al., 2001a; Qi et

al., 2010a; Warren et al., 2009). Volume based hygroscopic growth factor was monitored in a similar way as VFR, i.e., by taking a cubed ratio of particle mobility diameter after a humidification column to initially selected particle size.

### 3.2.5   Thermodenuder characterization

As a basis to evaluate the VFR in terms of vapor pressure, thermodenuder characterization was performed by measuring the VFR of select compounds with known vapor pressure ($D_{mi}$ = 150 nm). The vaporization profile was previously evaluated based on the temperature at which 50% of the mass evaporates ($T_{50}$) (Faulhaber et al., 2009). The vaporization profiles for hexanedioic acid and decanedioic acid acquired in this study agreed reasonably with Fualhaber et al. (2009) ($T_{50}$ agreed within 2°C), consistent with the similar residence times of the thermodenuders (This study: ~17 sec, Fualhaber et al. (2009): ~15 sec). Therefore we applied their vapor pressure calibration for approximate evaluation of SOA vapor pressure in this study (Figure 3.1).

The volatility of glyoxal oligomer was evaluated by generating glyoxal oligomer from evaporating droplets (De Haan et al., 2009a). Glyoxal solution in water (40wt%) was aerosolized by an atomizer into a 0.6 $m^3$ Teflon chamber. As water evaporated from the droplet, dihydrated glyoxal lost water to form more reactive monohydrated glyoxal, which then self-oligomerized to form low-volatility compounds (De Haan et al., 2009a). The vaporization profile suggested that the vapor pressure of dried glyoxal oligomer was much lower than $10^{-8}$ Pa, where reliable vapor pressure measurement is not possible.

Since dehydration is the key process of this oligomer formation, vapor pressure of oligomers could be higher if water is retained in particles. Vapor pressure of organosulfates (Galloway et al., 2009; Surrat et al., 2007) or nitrogen-containing species (De Haan et al., 2009b; Galloway et al., 2009) remains uncertain.

### 3.2.6 Chamber experiments

The experimental test matrix is summarized in Table 3.1. A known volume of high purity liquid hydrocarbon was injected through a heated glass injection manifold system and flushed into the chamber with pure $N_2$. Injection of 2-tert-butylphenol and $H_2O_2$ was performed in the same way as described in Nakao et al. (2011a). Since phenolic compounds are less volatile than hydrocarbons typically used for chamber experiments, injections into the chambers were carefully performed using a heated oven (50~80°C) through a heated transfer line maintained at a temperature higher than the oven. The glass manifold inside the oven was packed with glass wool to increase the mass transfer surface area. $H_2O_2$ was used as an additional OH radical source to test the role of glyoxal. $H_2O_2$ 50wt% solution was injected through the same oven system. Particle-free water vapor was injected using a two-unit system (Warren et al., 2009). Unit one contained Milli-Q water (Millipore, 18.2MΩ) with submerged heaters to maintain a desired water temperature, which determined the water vapor concentration in the air stream, while unit two contained a 1 μm filter. Purified air was bubbled through the water and then passed through the filter before entering the reactors. Humidity in the reactor was monitored by a humidity and temperature transmitter (VAISALA HMT334). Deliquesced $(NH_4)_2SO_4$

seed particles were generated by aerosolizing dilute $(NH_4)_2SO_4$ solution in Milli-Q water

by a custom-built atomizer, followed by Kr-85 neutralizer (TSI, model 3077) without

drying. Seed particles were confirmed to be deliquesced by using VTDMA; evaporation

of water from particles was observed by loss of volume after passing particles through a

thermodenuder. Particle wall-loss correction was performed by using exponential decay

rates of particle numbers (Carter et al., 2005).

## 3.3 Results and Discussion

### 3.3.1 Glyoxal uptake onto deliquesced $(NH_4)_2SO_4$

Significant SOA formation by glyoxal uptake onto deliquesced $(NH_4)_2SO_4$ was observed

under dark conditions (Figure 3.2). Wet ammonium sulfate seed particles were injected

into the chamber (RH=74%) and allowed to equilibrate, followed by glyoxal injection.

Immediately following the glyoxal injection, the organic/sulfate ratio measured by the

AMS increased due to glyoxal uptake, reaching a maximum value of ~0.4 around 6 hours

after glyoxal injection. After reaching maximum organic/sulfate ratio, the environmental

chamber was diluted; organic/sulfate ratio decreased due to evaporation of glyoxal

oligomers, suggesting glyoxal oligomerization is reversible, as also observed by

Galloway et al. (2009). The slower decrease of glyoxal concentration than tracer

concentration is consistent with the large glyoxal-reservoir effect of chamber surface

(Loza et al., 2010). In a separate experiment (not shown), no increase in organic/sulfate

ratio is observed for a similar experiment conducted under dry conditions (RH<0.1%),

confirming the critical role of aqueous phase of $(NH_4)_2SO_4$ seed particles in glyoxal oligomerization (Galloway et al., 2009; Kroll et al., 2005; Liggio et al., 2005b).

### 3.3.2 Evaluation of glyoxal uptake onto toluene SOA

Glyoxal uptake during SOA formation from toluene photooxidation was investigated under humid conditions (RH 40-80%). Previous studies observed oligomers in aromatic SOA formed within this RH range (e.g., RH 40-50%, Kalberer et al., 2004; Kalberer et al., 2006); heterogeneous reactions or particle-phase reaction of dicarbonyls, in particular glyoxal and methylglyoxal, were proposed to be important reaction mechanisms (Healy et al., 2008; Kalberer et al., 2004). However, the significance of glyoxal uptake in the aromatic SOA system has not been evaluated directly; this section evaluates the significance of glyoxal uptake onto toluene SOA during irradiated and dark conditions.

#### 3.3.2.1 Irradiated conditions

A representative toluene photooxidation experiment including toluene decay, SOA formation, and glyoxal formation is shown in Figure 3.3. Typically, glyoxal concentration remained below 10 ppb. The impact of glyoxal on SOA formation for the toluene photooxidation system was evaluated by injecting 80 ppb additional glyoxal into the system (Figure 3.4). The addition of 80 ppb glyoxal in the toluene + $NO_x$ oxidation system resulted in faster toluene decay and higher SOA formation (green trace in Figure 3.4). Since toluene predominantly reacts with OH radicals (reactions of toluene with $O_3$

or $NO_3$ are slow (Calvert et al., 2002)), the faster toluene decay indicates that OH radical concentration was enhanced by glyoxal photolysis. OH radical also influences aqueous chemistry (Volkamer et al., 2009) in addition to gas-phase chemistry (Calvert et al., 2002). To elucidate the role of increased OH radical versus glyoxal uptake, another toluene-$NO_x$ photooxidation experiment with elevated $H_2O_2$ concentration (added to match OH levels in the additional glyoxal experiment) was performed (red trace in Figure 3.4). Addition of $H_2O_2$ resulted in practically identical toluene decays between the $H_2O_2$ and glyoxal experiments. The similar toluene decay rates in these additional glyoxal/$H_2O_2$ experiments indicate successful matching of OH levels. For these two experiments, SOA formation was nearly identical, suggesting that the major impact of glyoxal was enhanced OH level, with insignificant contributions of glyoxal to SOA formation by direct uptake.

In addition to particle volume, particle volatility was monitored to evaluate glyoxal uptake onto SOA during irradiation. The evolution of VFR at 100°C of toluene SOA was monitored by VTDMA (Figure 3.5). The VFR of toluene SOA rapidly increased and plateaued after ~6 hours. The addition of glyoxal to the photooxidation system resulted in increased VFR. One might interpret this as contribution of glyoxal oligomer. However, the addition of $H_2O_2$ as a radical source resulted in nearly an identical profile, again suggesting that the role of glyoxal in toluene SOA formation (under irradiation) in this study was as a radical source, not an oligomer precursor.

### 3.3.2.2 Dark conditions

The absence of glyoxal uptake onto the toluene SOA was further investigated by the addition of glyoxal after SOA formation in the dark as a "SOA seed" experiment (Figure 3.6). Blacklights were turned off after ~9 hours of irradiation and nearly 100 ppb glyoxal was injected; no significant increase in particle volume concentration was observed. The absence of glyoxal uptake onto SOA seed is in contrast with the aforementioned significant glyoxal uptake onto deliquesced $(NH_4)_2SO_4$; the difference highlights the importance of liquid water content (LWC) and/or electrolytes in glyoxal uptake as discussed below.

### 3.3.2.3 Impact of LWC and electrolytes

Previous studies proposed LWC as a major contributor to SOA formation via aqueous reactions (Kamens et al., 2011; Volkamer et al., 2009; Zhou et al., 2011). LWC for toluene SOA at a given RH was estimated using a humidogram acquired from a dry toluene + $NO_x$ experiment (Figure 3.7) and shown in Table 3.1 (a volume ratio taken from the humidogram is converted into a mass fraction assuming SOA density 1.4 $g/cm^3$). LWC for deliquesced $(NH_4)_2SO_4$ was estimated using ISORROPIA (Nenes et al., 1998). The absence of significant glyoxal uptake onto toluene SOA can be interpreted as a result of smaller LWC of SOA than that of $(NH_4)_2SO_4$ (Table.1), which is in agreement with the growing belief that liquid water is needed for glyoxal uptake (e.g., Kamens et al., 2011; Volkamer et al., 2009). In order for glyoxal uptake to significantly occur during the irradiated conditions in this study, higher LWC, rather than higher RH, might be required

(Kamens et al., 2011). In addition, the composition of the aqueous phase matters to glyoxal uptake; previous studies reported enhanced partitioning of glyoxal into water containing sulfate ion (Ip et al., 2009) and catalytic effect of ammonium ion on glyoxal oligomerization (Nozière et al., 2008). Kroll et al. (2005) observed far higher (by a factor of ~70) glyoxal uptake onto deliquesced $(NH_4)_2SO_4$ than by pure water. The absence of glyoxal uptake onto toluene SOA shown in Figure 3.6 suggests that aqueous phase of toluene SOA may not be preferable for glyoxal uptake.

### 3.3.3    Effect of deliquesced $(NH_4)_2SO_4$ seed on toluene SOA formation

Deliquesced $(NH_4)_2SO_4$ was confirmed to rapidly form SOA in the presence of glyoxal (Figure 3.2). If glyoxal uptake onto deliquesced $(NH_4)_2SO_4$ is a major mechanism of toluene SOA formation, the presence of deliquesced $(NH_4)_2SO_4$ seed particles is expected to enhance the toluene SOA formation significantly. SOA growth curves (SOA formation vs. hydrocarbon consumption) for non-seeded (nucleation) experiments and deliquesced $(NH_4)_2SO_4$ seeded experiments are shown in Figure 3.8. No significant difference in those two systems was observed, suggesting that non-glyoxal routes dominated the aromatic SOA formation pathways.

Although the presence of deliquesced $(NH_4)_2SO_4$ seed particles results in higher LWC, SOA formation from toluene photooxidation is not enhanced (Figure 3.8). This is in contrast with the aforementioned impact of LWC and electrolytes on glyoxal uptake (section 3.2.3). A possible explanation is that the high concentration of SOA overwhelmed the preexisting seed particles thereby reducing the apparent seed effects;

61

assuming the same extent of glyoxal uptake onto ammonium sulfate occurred as in the glyoxal + seed experiment, glyoxal SOA would comprise only a minor mass fraction of toluene SOA since the seed mass fraction dropped to approximately 10% in six hours (not shown) and glyoxal oligomer/sulfate ratio would be approximately 0.4 (Figure 3.2). Applying the results of dark glyoxal uptake to irradiated conditions is uncertain due to the possibility of fast photochemical uptake of glyoxal (Volkamer et al., 2009); however, Galloway et al. (2011) did not observe fast photochemical uptake, and hence the significance of the fast photochemical uptake is highly uncertain. Another possible explanation for the absence of seed effects is core-shell morphology of SOA-deliquesced $(NH_4)_2SO_4$ particles (e.g., Anttila et al., 2006; Bertram et al., 2011; Smith et al., 2011); an organic coating around deliquesced $(NH_4)_2SO_4$ core may slow down the uptake of glyoxal induced by LWC and the electrolytes, resulting in reduction of the seed effects.

### 3.3.4    Evaluation of glyoxal uptake onto 2-tert-butylphenol SOA

The absence of significant SOA formation from glyoxal uptake onto toluene SOA is further probed by using 2-tert-butylphenol as a parent aromatic compound. When SOA formed from 2-tert-butylphenol was introduced into the HR-ToF-AMS, significant signals of the $C_4H_9^+$ fragment from the tert-butyl substituent were observed. Since glyoxal oligomerization can not produce $C_4H_9^+$, $C_4H_9^+$ can be used as a tracer for the SOA from 2-tert-butylphenol oxidation. The phenolic functionality (-OH) was used to enhance the reactivity of aromatic ring (e.g., *o*-cresol is seven times more reactive than toluene, Calvert et al. (2002)) and to minimize the reaction of the tert-butyl substituent. Although the steric hindrance by the tert-butyl group remains uncertain, adequately

similar aromatic oxidation reaction is expected for the purpose of evaluating glyoxal uptake. The result of 2-tert-butylphenol oxidation is shown in Figure 3.9. Glyoxal addition to this system during photooxidation (at 10 hours after lights on) resulted in enhanced SOA formation; however the fraction of $C_4H_9^+$ in the total organics ($fC_4H_9$) did not change significantly indicating that aerosol formation from products not containing $C_4H_9^+$ fragments (glyoxal and its products) was not enhanced after glyoxal injection and oxidation. This further confirms that glyoxal's influence on SOA formation in the aromatic photooxidation systems under humid conditions (RH 51% for this experiment) is limited to increasing SOA formation by increasing gas-phase OH radical concentrations and not by reactive uptake of glyoxal into the SOA.

### 3.3.5    Comparison with previous studies

Consistencies and differences with previous studies are summarized in this section. Under dark conditions, this study observed significant SOA formation from glyoxal uptake onto deliquesced $(NH_4)_2SO_4$ seed, consistent with previous studies (e.g., Galloway et al., 2009; Kroll et al., 2005; Liggio et al., 2005a; Volkamer et al., 2009). However, glyoxal uptake onto SOA seed was not observed under dark/humid conditions (section 3.2.2); this is in agreement with the importance of LWC and electrolytes (Ip et al., 2009; Kamens et al., 2011; Volkamer et al., 2009).

Recent studies by Zhou et al. (2011) and Kamens et al. (2011) observed that particle water concentration was highly related to SOA formation from aromatic hydrocarbons

(toluene and xylenes), which was largely explained by oligomerization of glyoxal (to a lesser extent, methylglyoxal) in aqueous phase. Since this study also observed higher SOA formation for high RH and LWC experiments (e.g., Run 1499B vs., 1497A, Table 3.1), our results are partly in agreement with their study. However, our direct measurement of glyoxal by CEAS, along with experiments using synthesized glyoxal, strongly indicates glyoxal uptake was insignificant during aromatic SOA formation, at least in our experimental conditions (e.g., LWC, SOA loadings).

One of the differences between this study and their study is particle concentration ranges: Zhou et al. (2011) and Kamens et al. (2011) – from ~1 to ~30 $\mu g/m^3$; this study - from ~30$\mu g/m^3$ to over 100 $\mu g/m^3$. Since glyoxal uptake is not driven by partitioning to organics but by dissolution into water (Volkamer et al., 2009), glyoxal uptake might preferentially occur in their low organic aerosol / high RH experiments (over 90% for some experiments). Also, the higher SOA formation in the higher LWC experiments (observed in both their study and this study) could be explained by aqueous reactions of water-soluble products other than glyoxal, such as phenolic compounds (Sun et al., 2010). Different experimental conditions such as light sources (natural vs. blacklights) or background composition may also contribute to the different observations.

Applicability of this study on aromatics to other compounds, such as biogenic compounds, remains uncertain. However, assuming LWC is the key parameter in glyoxal uptake (Kamens et al., 2011), similar results are expected for biogenic SOA since

hygroscopic growth factors of biogenic SOA were often observed to be approximately same as (or slightly less than) those of aromatic SOA (Jimenez et al. (2009) – α-pinene, isoprene, and trimethylbenzene; Cocker et al. (2001b) - α-pinene, *m*-xylene, and 1,3,5-trimethylbenzene; Qi et al. (2010a) – α-pinene and *m*-xylene; Prenni et al. (2007) – α-pinene, β-pinene, $\Delta^3$-carene, and toluene). Thus, further evaluation of glyoxal uptake onto biogenic SOA would be beneficial.

## 3.4 Conclusion

The significance of glyoxal uptake in SOA formation from aromatic hydrocarbon photooxidation was evaluated for the first time. Glyoxal uptake onto deliquesced $(NH_4)_2SO_4$ seed resulted in rapid SOA formation as shown in previous studies; however, no significant glyoxal uptake onto SOA formed from aromatic hydrocarbon oxidation was observed. Instead of contributing to SOA formation by reactive uptake, glyoxal acted as an OH radical source following photolysis. This study suggests that the uptake and/or subsequent reaction of glyoxal in aqueous phase of aerosol to form low-volatility compounds contributes to only minor fraction of aromatic SOA in an environmental chamber (RH less than 80%). This study highlights the need for evaluating glyoxal uptake onto SOA seed. This study does not preclude glyoxal uptake onto aromatic SOA at RH above 80% (or higher LWC), uptake onto non-aromatic SOA, or glyoxal cloud processing.

## 3.5    References

Anttila, T., Kiendler-Scharr, A., Tillmann, R., Mentel, T. F.: On the reactive uptake of gaseous compounds by organic-coated aqueous aerosols: theoretical analysis and application to the heterogeneous hydrolysis of N2O5, J. Phys. Chem. A, 110, 10435-10443, 2006

Arey, J., Obermeyer, G., Aschmann, S. M., Chattopadhyay, S., Cusick, R. D., Atkinson, R.: Dicarbonyl products of the OH radical-initiated reaction of a series of aromatics hydrocarbons, Environmental Science & Technology, 43, 683-689, 2009

Bertram, A. K., Martin, S. T., Hanna, S. J., Smith, M. L., Bodsworth, A., Chen, Q., Kuwata, M., Liu, A., You, Y., Zorn, S. R.: Predicting the relative humidities of liquid-liquid phase separation, efflorescence, and deliquescence of mixed particles of ammonium sulfate, organic material, and water using the organic-to-sulfate mass ratio of the particle and the oxygen-to-carbon elemental ratio of the organic component, Atmos. Chem. Phys., 11(21), 10995-11006, 2011

Birdsall, A. W., Andreoni, J. F., Elrod, M. J.: Investigation of the role of bicyclic peroxy radicals in the oxidation mechanism of toluene, J. Phys. Chem., 114, 10655-10663, 2010

Calvert, J. G., Atkinson, R., Becker, K. H., Kamens, R. M., Seinfeld, J. H., Wallington, T. J., Yarwood, G.: The mechanism of atmospheric oxidation of aromatics hydrocarbons. New York, Oxford University Prss. 2002.

Carter, W. P. L., Cocker, D. R., Fitz, D. R., Malkina, I. L., Bumiller, K., Sauer, C. G., Pisano, J. T., Bufalino, C., Song, C.: A new environmental chamber for evaluation of gas-phase chemical mechanisms and secondary aerosol formation, Atmospheric Environment, 39, 7768-7788, 2005

Cocker, D. R., Flagan, R. C., Seinfeld, J. H.: State-of the art chamber facility for studying atmospheric aerosol chemistry, Environmental Science & Technology, 35(12), 2594-2601, 2001a

Cocker, D. R., Mader, B. T., Kalberer, M., Flagan, R. C., Seinfeld, J. H.: The effect of water on gas-particle partitioning of secondary organic aerosol: 2. m-xylene and 1,3,5-

trimethylbenzene photooxidation systems, Atmospheric Environment, 35, 6073-6085, 2001b

Coeur-Tourneur, C., Henry, F., Janquin, M.-A., Brutier, L.: Gas-phase reaction of hydroxyl radicals with m-, o- and p-cresol, International Journal of Chemical Kinetics, 38(9), 553-562, 2006

Corrigan, A. L., Hanley, S. W., De Haan, D. O.: Uptake of Glyoxal by Organic and Inorganic Aerosol, Environmental Science & Technology, 42(12), 4428-4433, 2008

De Haan, D. O., Corrigan, A. L., Tolbert, M. A., Jimenez, J. L., Wood, S. E., Turley, J. J.: Secondary Organic Aerosol Formation by Self-Reactions of Methylglyoxal and Glyoxal in Evaporating Droplets, Environ. Sci. Technol., 43(21), 8184-8190, 2009a

De Haan, D. O., Tolbert, M. A., Jimenez, J. L.: Atmospheric condensed-phase reactions of glyoxal with methylamine, Geophys. Res. Lett., 36(11), L11819, 2009b

DeCarlo, P. F., Kimmel, J. R., Trimborn, A. M., Northway, M., Jayne, J. T., Aiken, A. C., Gonin, M., Fuhrer, K., Horvath, T., Docherty, K., Worsnop, D. R., Jimenez, J. L.: Field-deployable, high-resolution, Time-of-Flight Aerosol Mass Spectrometer, Anal. Chem., 78, 8281-8289, 2006

Engeln, R., Berden, G., Peeters, R., Meijer, G.: Cavity enhanced absorption and cavity enhanced magnetic rotation spectroscopy, Review of Scientific Instruments, 69(11), 3763-3769, 1998

Ervens, B., Feingold, G., Frost, G. J., Kreidenweis, S. M.: A modeling study of aqueous production of dicarboxylic acids: 1. Chemical pathways and speciated organic mass production, Journal of Geophysical Research, 109, D15205, 2004

Faulhaber, A. E., Thomas, B. M., Jimenez, J. L., Jayne, J., Worsnop, D. R., Ziemann, P. J.: Characterization of a thermodenuder-particle beam mass specrometer system for the study of organic aerosol volatility and composition, Atmospheric Measurement Techniques, 2, 15-31, 2009

Fiedler, S. E., A. Hese, A. A. Ruth: Incoherent broad-band cavity-enhanced absorption spectroscopy, Chemical Physics Letters, 371(284-294) 2003

Fiedler, S. E., Hese, A., Ruth, A. A.: Incoherent broad-band cavity-enhanced absorption spectroscopy of liquids, Review of Scientific Instruments, 76(2), 023107-023107-7, 2005

Finlayson-Pitts, B. J., Pitts, J. N.: Chemistry of the upper and lower atmosphere: Theory, experiments, and applications. San Diego, Academic Press. 1999.

Fu, T.-M., Jacob, D. J., Wittrock, F., Burrows, J. P., Vrekoussis, M., Henze, D. K.: Global budgets of atmospheric glyoxal and methylglyoxal and implications for formation of secondary organic aerosols, Journal of Geophysical Research, 113, D15303, 2008

Galloway, M. M., Chhabra, P., Chan, A. W. H., Surratt, J. D., Flagan, R. C., Seinfeld, J. H., Keutsch, F. N.: Glyoxal uptake on ammonium sulphate seed aerosol: reaction products and reversibility of uptake under dark and irradiated conditions, Atmospheric Chemistry and Physics, 9, 3331-3345, 2009

Galloway, M. M., Loza, C. L., Chhabra, P. S., Chan, A. W. H., Yee, L. D., Seinfeld, J. H., Keutsch, F. N.: Analysis of photochemical and dark glyoxal uptake: Implications for SOA formation, Geophys. Res. Lett., 38(17), L17811, 2011

Hallquist, M., Wenger, J. C., Baltensperger, U., Rudich, Y., Simpson, D., Claeys, M., Dommen, J., Donahue, N. M., George, C., Goldstein, A. H., Hamilton, J. F., Herrmann, H., Hoffmann, T., Iinuma, Y., Jang, M., Jenkin, M., Jimenes, J. L., Kiendler-Scharr, A., Maenhaut, W., McFiggans, G., Mentel, T. F., Monod, A., Prevot, A. S., Seinfeld, J. H., Surratt, J. D., Szmigielski, R., Willdt, J.: The formation, properties and impact of secondary organic aerosol: current and emerging issues, Atmospheric Chemistry and Physics, 9, 5155-5236, 2009

Hamilton, J. F., Webb, P. J., Lewis, A. C., Reviejo, M. M.: Quantifying small molecules in secondary organic aerosol formation during the photo-oxidation of toluene with hydroxyl radicals, Atmospheric Environment, 39, 7263-7275, 2005

Healy, R. M., Wenger, J. C., Metzger, A., Duplissy, J., Kalberer, M., Dommen, J.: Gas/particle partitioning of carbonyls in the photooxidation of isoprene and 1,3,5-trimethylbenzene, Atmospheric Chemistry and Physics, 8, 3215-3230, 2008

Hurley, M. D., Sokolov, O., Wallington, T. J., Takekawa, H., Karasawa, M., Klotz, B.: Organic aerosol formation during the atmospheric degradation of toluene, Environmental Science & Technology, 35(7), 1358-1366, 2001

Ip, H. S. S., Huang, X. H. H., Yu, J. Z.: Effective Henry's law constants of glyoxal, glyoxylic acid, and glycolic acid, Geophysical Research Letters, 36, L01802, 2009

Jang, M., Kamens, R. M.: Atmospheric Secondary Aerosol Formation by Heterogeneous Reactions of Aldehydes in the Presence of a Sulfuric Acid Aerosol Catalyst, Environmental Science & Technology, 35(24), 4758-4766, 2001

Jayne, J. T., Leard, D. C., Zhang, X., Davidovits, P., Smith, K. A., Kolb, C. E., Worsnop, D. R.: Development of an Aerosol Mass Spectrometer for size and composition analysis of sibmicron particles, Aerosol Science and Technology, 33, 49-70, 2000

Jimenez, J. L., Canagaratna, M. R., Donahue, N. M., Prevot, A. S. H., Zhang, Q., Kroll, J. H., DeCarlo, P. F., Allan, J. D., Coe, H., Ng, N. L., Aiken, A. C., Docherty, K. S., Ulbrich, I. M., Grieshop, A. P., Robinson, A. L., Duplissy, J., Smith, J. D., Wilson, K. R., Lanz, V. A., Hueglin, C., Sun, Y. L., Tian, J., Laaksonen, A., Raatikainen, T., Vaattovaara, P., Ehn, M., Kulmala, M., Tomlinson, J. M., Collins, D. R., Cubison, M. J., Dunlea, E. J., Huffman, J. A., Onasch, T. B., Alfarra, M. R., Williams, P. I., Bower, K., Kondo, Y., Schneider, J., Drewnick, F., Borrmann, S., Weimer, S., Demerjian, K., Salcedo, D., Cottrell, L., Griffin, R. J., Takami, A., Miyoshi, T., Hatakeyama, S., Shimono, A., Sun, J. Y., Zhang, Y. M., Dzepina, K., Kimmel, J. R., Sueper, D., Jayne, J. T., Herndon, S. C., Trimborn, A. M., Williams, L. R., Wood, E. C., Middlebrook, A. M., Kolb, C. E., Baltensperger, U., Worsnop, D. R.: Evolution of organic aerosols in the atmosphere, Science, 326, 1525-1529, 2009

Johnson, D., Jenkin, M., Wirtz, K., Martin-Reviejo, M.: Simulating the formation of secondary organic aerosol from the photooxidation of toluene, Environ. Chem., 1, 150-165, 2004

Johnson, D., Jenkin, M. E., Wirtz, K., Martin-Reviejo, M.: Simulating the formation of secondary organic aerosol from the photooxidation of aromatics hydrocarbons, Environ. Chem., 2, 35-48, 2005

Kalberer, M., Paulsen, D., Sax, M., Steinbacher, M., Dommen, J., Prevot, A. S., Fisseha, R., Weingartner, E., Frankevich, V., Zenobi, R., Baltensperger, U.: Identification of polymers as major components of atmospheric organic aerosols, Science, 303, 1659-1662, 2004

Kalberer, M., Sax, M., Samburova, V.: Molecular size evolution of oligomers in organic aerosols collected in urban atmospheres and generated in a smog chamber, Environmental Science & Technology, 40(19), 5917-5922, 2006

Kamens, R. M., Zhang, H., Chen, E. H., Zhou, Y., Parikh, H. M., Wilson, R. L., Galloway, K. E., Rosen, E. P.: Secondary organic aerosol formation from toluene in an atmospheric hydrocarbon mixture: Water and particle seed effects, Atmospheric Environment, 45(13), 2324-2334, 2011

Kroll, J. H., Ng, N. L., Murphy, S. M., Varutbangkul, V., Flagan, R. C., Seinfeld, J. H.: Chamber studies of secondary organic aerosol growth by reactive uptake of simple carbonyl compounds, Journal of Geophysical Research, 110, D23207, 2005

Langridge, J. M., Ball, S. M., Jones, R. L.: A compact broadband cavity enhanced absorption spectrometer for detection of atmospheric NO2 using light emitting diodes, Analyst, 131(8), 916-922, 2006

Liggio, J., Li, S.-M., Mclaren, R.: Heterogeneous reactions of glyoxal on particulate matter: identification of acetals and sulfate esters, Environmental Science & Technology, 39, 1532-1541, 2005a

Liggio, J., Li, S.-M., McLaren, R.: Reactive uptake of glyoxal by particulate matter, Journal of Geophysical Research, 110, D10304, 2005b

Lim, Y. B., Tan, Y., Perri, M. J., Seitzinger, S. P., Turpin, B. J.: Aqueous chemistry and its role in secondary organic aerosol (SOA) formation, Atmospheric Chemistry and Physics, 10(21), 10521-10539, 2010

Loza, C. L., Chan, A. W. H., Galloway, M. M., Keutsch, F. N., Flagan, R. C., Seinfeld, J. H.: Characterization of vapor wall loss in laboratory chambers, Environmental Science & Technology, 44, 5074-5078, 2010

Nakao, S., Clark, C., Tang, P., Sato, K., Cocker III, D.: Secondary organic aerosol formation from phenolic compounds in the absence of NOx, Atmos. Chem. Phys., 11(20), 10649-10660, 2011a

Nakao, S., Shrivastava, M., Nguyen, A., Jung, H., Cocker, D.: Interpretation of Secondary Organic Aerosol Formation from Diesel Exhaust Photooxidation in an Environmental Chamber, Aerosol Science and Technology, 45(8), 954-962, 2011b

Nenes, A., Pandis, S. N., Pilinis, C.: ISORROPIA: A New Thermodynamic Equilibrium Model for Multiphase Multicomponent Inorganic Aerosols, Aquatic Geochemistry, 4(1), 123-152, 1998

Ng, N. L., Kroll, J. H., Chan, A. W. H., Chhabra, P., Flagan, R. C., Seinfeld, J. H.: Secondary organic aerosol formation from m-xylene, toluene, and benzene, Atmospheric Chemistry and Physics, 7, 3909-3922, 2007

Nozière, B., Dziedzic, P., Córdova, A.: Products and Kinetics of the Liquid-Phase Reaction of Glyoxal Catalyzed by Ammonium Ions (NH4+), The Journal of Physical Chemistry A, 113(1), 231-237, 2008

Odum, J. R., Hoffman, T., Bowman, F., Collins, D., Flagan, R. C., Seinfeld, J. H.: Gas/particle partitioning and secondary organic aerosol yields, Environmental Science & Technology, 30(8), 2580-2585, 1996

Olariu, R. I., Klotz, B., Barnes, I., Becker, K. H., Mocanu, R.: FT-IR study of the ring-retaining products from the reaction of OH radicals with phenol, o-, m-, and p-cresol, Atmospheric Environment, 36, 3685-3697, 2002

Pankow, J. F.: An absorption model of gas/particle partitioning of organic compounds in the atmosphere, Atmospheric Environment, 28(2), 185-188, 1994

Paul, J. B., L. Lapson, and J. G. Anderson: Ultrasensitive absorption spectroscopy with a high-finesse optical cavity and off-axis alignment, Applied Optics, 40(27), 4904-4910, 2001

Prenni, A. J., Petters, M. D., Kreidenweis, S. M., DeMott, P. J., Ziemann, P. J.: Cloud droplet activation of secondary organic aerosol, Journal of Geophysical Research, 112(D10223), doi:10.1029/2006JD007963, 2007

Qi, L., Nakao, S., Malloy, Q., Warren, B., Cocker, D. R.: Can secondary organic aerosol formed in an atmospheric simulation chamber continuously age?, Atmospheric Environment, 44, 2990-2996, 2010a

Qi, L., Nakao, S., Tang, P., Cocker III, D. R.: Temperature effect on physical and chemical properties of secondary organic aerosol from m-xylene photooxidation, Atmos. Chem. Phys., 10(8), 3847-3854, 2010b

Rader, D. J., McMurry, P. H.: Application of the Tandem Differential Mobility Analyzer to studies of droplet growth or evaporation, Journal of Aerosol Science, 17(5), 771-787, 1986

Sato, K., Hatakeyama, S., Imamura, T.: Secondary organic aerosol formation during the photooxidation of toluene: NOx dependence of chemical composition, J. Phys. Chem. A, 111, 9796-9808, 2007

Seinfeld, J. H., Pandis, S. N.: Atmospheric Chemistry and Physics: From Air Pollution to Climate Change - 2nd ed. New Jersey, A Wiley-Interscience publication. 2006.

Smith, M. L., Kuwata, M., Martin, S. T.: Secondary Organic Material Produced by the Dark Ozonolysis of α-Pinene Minimally Affects the Deliquescence and Efflorescence of Ammonium Sulfate, Aerosol Science and Technology, 45(2), 244-261, 2011

Sun, Y. L., Zhang, Q., Anastasio, C., Sun, J.: Insights into secondary organic aerosol formed via aqueous-phase reactions of phenolic compounds based on high resolution mass spectrometry, Atmospheric Chemistry and Physics, 10, 4809-4822, 2010

Surrat, J. D., Kroll, J. H., Kleinsienst, T. E., Edney, E. O., Claeys, M., Sorooshian, A., Ng, N. L., Offenberg, J. H., Lewandowski, M., Jaoui, M., Jaouri, R., Flagan, R. C., Seinfield, J. H.: Evidence for organosulfates in secondary organic aerosol, Environmental Science & Technology, 41(2), 517-527, 2007

Takekawa, H., Minoura, H., Yamazaki, S.: Temperature dependence of secondary organic aerosol formation by photo-oxidation of hydrocarbons, Atmospheric Environment, 37, 3413-3424, 2003

Tolocka, M. P., Jang, M., Ginter, J. M., Cox, F. J., Kamens, R. M., Johnston, M. V.: Formation of oligomers in secondary organic aerosol, Environmental Science & Technology, 38, 1428-1434, 2004

Volkamer, R., Klotz, B., Barnes, I., Imamura, T., Washida, N.: OH-initiated oxidation of benzene Part 1. Phenol formation under atmospheric conditions, Phys. Chem. Chem. Phys., 4, 1598-1610, 2002

Volkamer, R., Martini, F. S., Molina, L. T., Salcedo, D., Jimenez, J. L., Molina, M. J.: A missing sink for gas-phase glyoxal in Mexico city: Formation of secondary organic aerosol, Geophysical Research Letters, 34, L19807, 2007

Volkamer, R., Spietz, P., Burrows, J., Platt, U.: High-resolution absorption cross-section of glyoxal in the UV-vis and IR spectral ranges, Journal of Photochemistry and Photobiology a-Chemistry, 172(1), 35-46, 2005

Volkamer, R., Ziemann, P. J., Molina, L. T.: Secondary organic aerosol formation from acetylene (C2H2): seed effect on SOA yields due to organic photochemistry in the aerosol aqueous phase, Atmospheric Chemistry and Physics, 9, 1907-1928, 2009

Warren, B., Malloy, Q., Yee, L. D., Cocker, D. R.: Secondary organic aerosol formation from cyclohexene ozonolysis in the presence of water vapor and dissolved salts, Atmospheric Environment, 43, 1789-1795, 2009

Washenfelder, R. A., A. O. Langford, H. Fuchs, and S. S. Brown Measurements of glyoxal using an incoherent broadband cavity enhanced absorption spectrometer, Atmospheric Chemistry and Physics, 8, 7779-7793, 2008

Washenfelder, R. A., Langford, A. O., Fuchs, H., Brown, S. S.: Measurement of glyoxal using an incoherent broadband cavity enhanced absorption spectrometer, Atmospheric Chemistry and Physics, 8, 7779-7793, 2008

Zhou, Y., Zhang, H., Parikh, H. M., Chen, E. H., Rattanavaraha, W., Rosen, E. P., Wang, W., Kamens, R. M.: Secondary Organic Aerosol Formation from Xylenes and Mixtures of Toluene and Xylenes in an Atmospheric Urban Hydrocarbon Mixture: Water and Particle Seed Effects (II), Atmospheric Environment, 45, 3882-3890, 2011

Table 3.1 Experimental test matrix

| Run ID | Run type | Aromatic,$_{ii}$[a] (ppb) | Aromatic,$_f$[b] (ppb) | ΔAromatic (μg/m³) | $M_{org+water}$[c] (μm³/cm³) | NO[a] (ppb) | $H_2O_2$[d] (ppm) | Glyoxal[a] (ppb) | RH (%) | Seed volume[a] (μm³/cm³) | LWC[c] (%mass) |
|---|---|---|---|---|---|---|---|---|---|---|---|
| 1368A | glyoxal + AS[e] | - | - | - | 12.0 | - | - | 46 | 74 | 101.0 | 51[f] |
| 1499B | toluene + $NO_x$ | 70.5 | 9.4 | 230 | 25.5 | 46.3 | - | - | <0.1 | - | 0 |
| 1503A | toluene + $NO_x$ | 100.7 | 16.8 | 316 | 57.1 | 41.5 | - | - | 40 | - | 1[g] |
| 1497A | toluene + $NO_x$ | 94.9 | 39.6 | 208 | 65.9 | 47.1 | - | - | 65 | - | 6[g] |
| 1497B | toluene + $NO_x$ | 94.8 | 47.4 | 179 | 65.9 | 22.5 | - | - | 65 | - | 6[g] |
| 1498A | toluene + $NO_x$ | 100.0 | 30.4 | 262 | 65.0 | 40.2 | - | - | 75 | - | 10[g] |
| 1500B | toluene + $NO_x$ | 104.2 | 30.4 | 278 | 77.7 | 45.3 | - | - | 70 | - | 8[g] |
| 1501A | toluene + $NO_x$ + glyoxal | 101.7 | 20.5 | 306 | 107.0 | 43.2 | - | 80 | 75 | - | 10[g] |
| 1501B | toluene + $NO_x$ + $H_2O_2$ | 100.9 | 22.8 | 294 | 98.2 | 43.2 | 0.3 | - | 75 | - | 10[g] |
| 1509A | toluene + $NO_x$ + $H_2O_2$ | 98.3 | 26.4 | 271 | 89.0 | 42.6 | 0.3 | - | 72 | - | 9[g] |
| 1510A | toluene + $NO_x$ + AS | 102.0 | 25.2 | 289 | 82.4 | 42.8 | - | - | 79 | 56.9 | 56[f] |
| 1510B | toluene + $NO_x$ + AS | 102.3 | 24.1 | 295 | 104.2 | 42.8 | - | - | 79 | 83.1 | 56[f] |
| 1511A | toluene + $NO_x$ + AS | 95.6 | 29.0 | 251 | 71.2 | 40.5 | - | - | 78 | 61.5 | 55[f] |
| 1511B | toluene + $NO_x$ + AS | 95.6 | 27.9 | 255 | 94.3 | 40.7 | - | - | 78 | 59.1 | 55[f] |
| 1489A | 2t-BP + $H_2O_2$ | 124.0 | 26.2 | 601 | 52.8 | - | 0.3 | 720[d] | 51 | - | 1[g] |

a: Initial concentration
b: Final concentration
c: Wall-loss corrected organic (+ water) volume measured by SMPS
d: Calculated using injected amount
e: AS: ammonium sulfate
f: Calculated using ISORROPIA (Nenes et al., 1998)
g: Calculated using $M_{org+water}$ and humidogram for toluene SOA

## 3.7    Figures
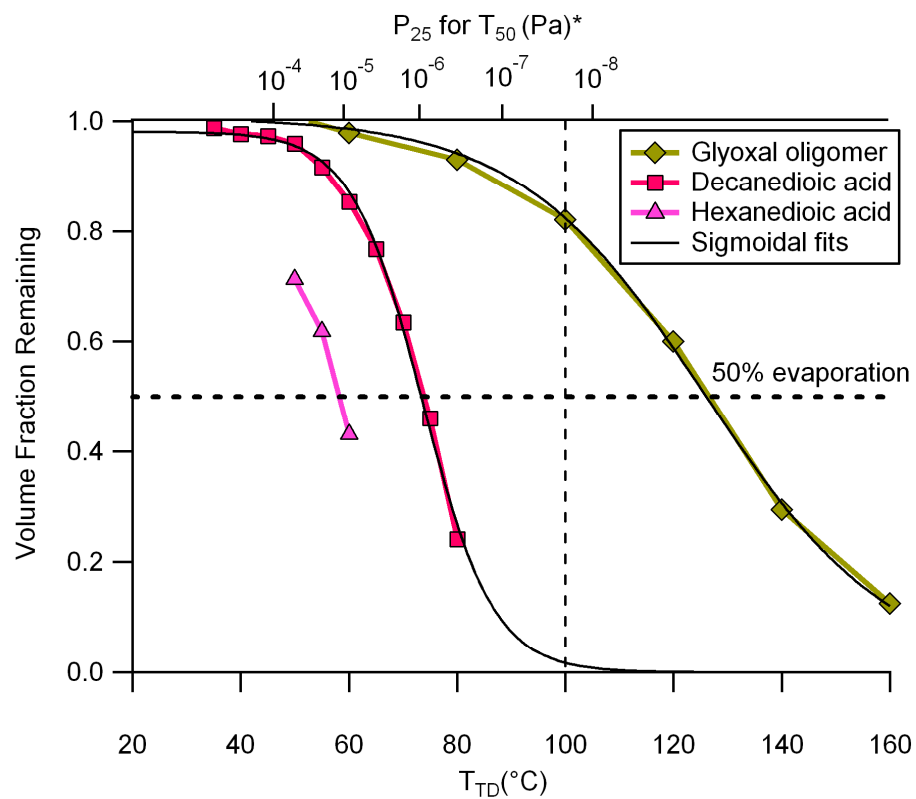


Figure 3.1 Thermograms of hexanedioic acid, decanedioic acid, and glyoxal oligomer (produced from evaporating droplets of glyoxal/water solution) where $T_{TD}$ is the set temperature of the thermodenuder and $P_{25}$ is the vapor pressure of a compound at 25°C (*calibration taken from Faulhaber et al. (2009))
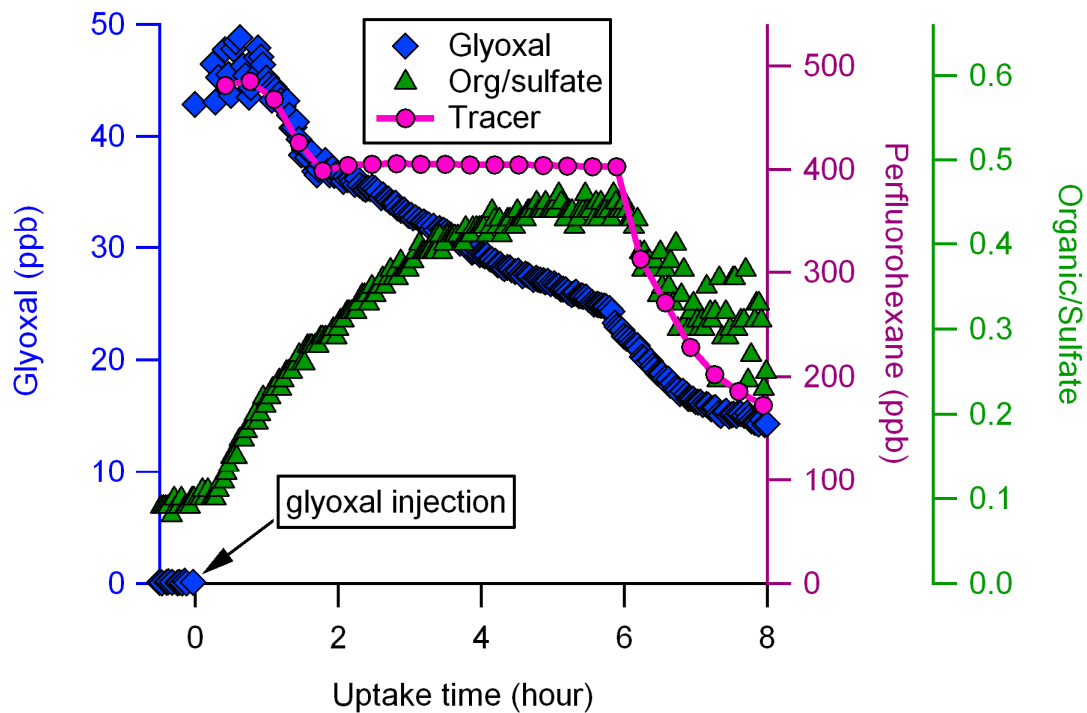
Figure 3.2 Typical time traces of glyoxal, organic/sulfate ratio, and tracer (perfluorohexane) during toluene-$NO_x$ photooxidation (EPA1368A). Immediately after glyoxal injection, organic/sulfate ratio increased. Upon dilution at 6 hours after injection, organic/sulfate ratio decreased due to evaporation of organics, consistent with Galloway et al. (2009).
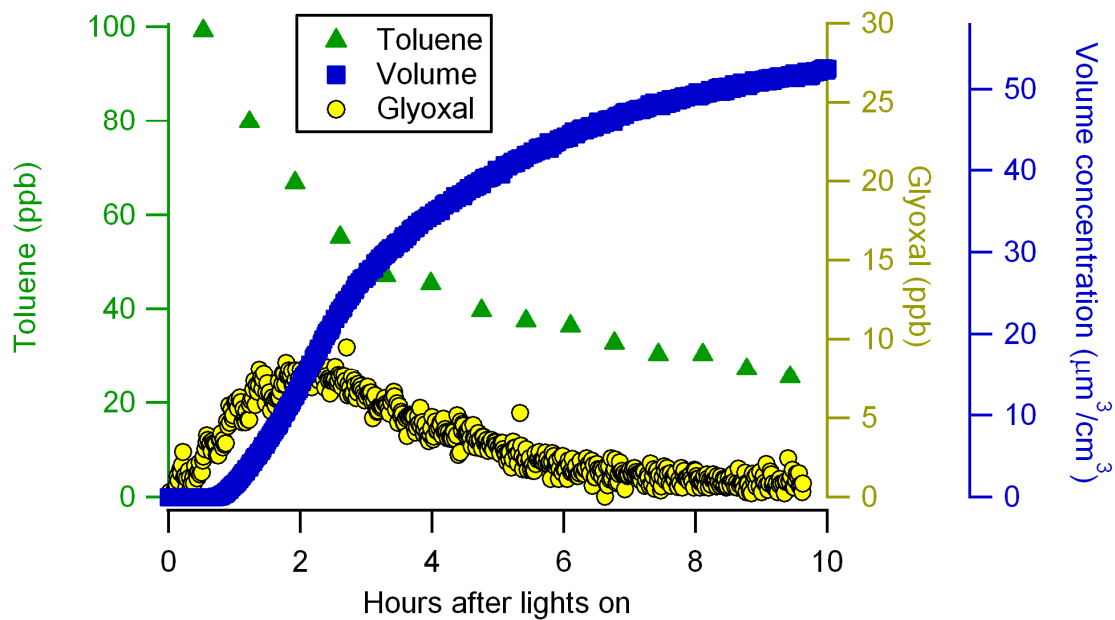
Figure 3.3 The time traces of toluene, particle volume concentration, and glyoxal concentration during toluene-$NO_x$ photooxidation. (EPA1503A). Typically glyoxal concentration was below 10ppb.
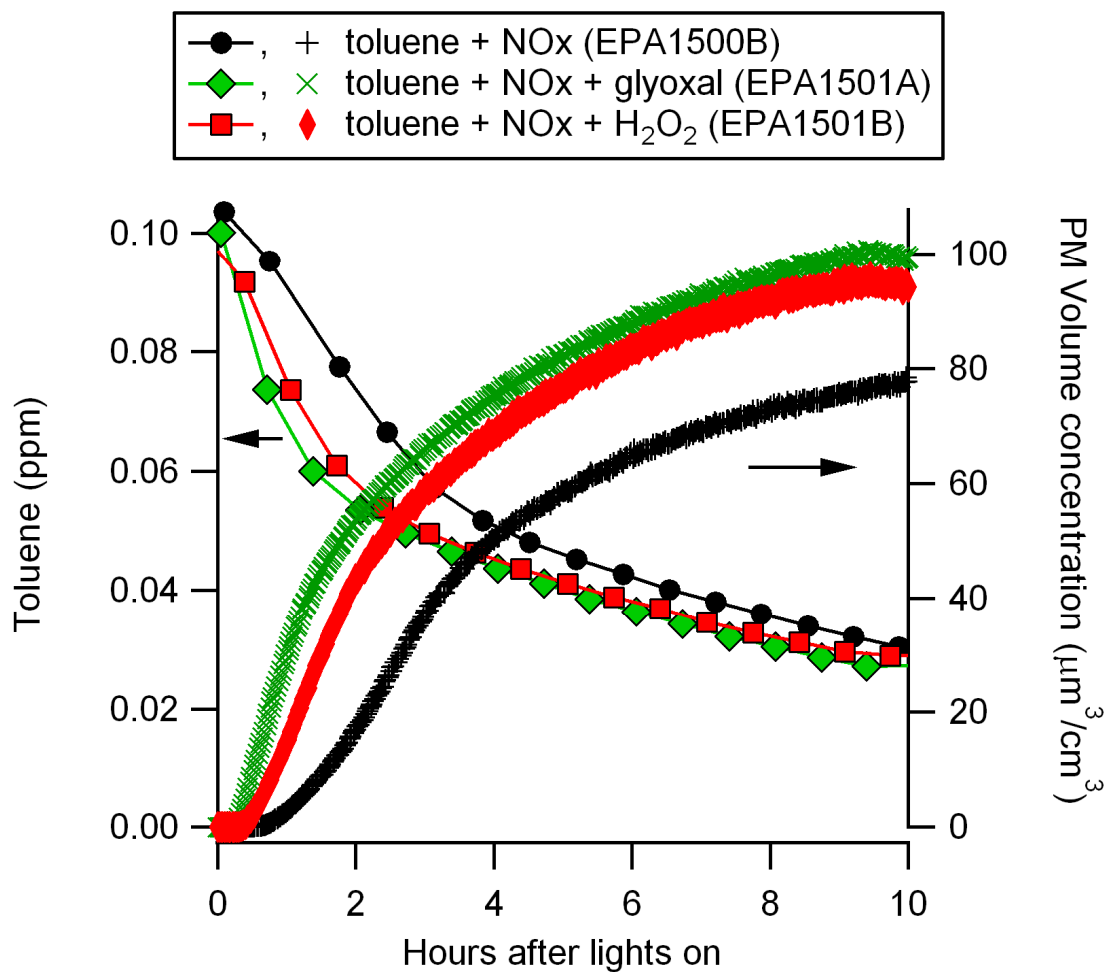
Figure 3.4 Evaluation of glyoxal impact as a radical source. Addition of glyoxal (green trace) and $H_2O_2$ (red trace) resulted in nearly identical toluene decay and SOA formation, indicating that glyoxal acted as a radical source, instead of an oligomer precursor.
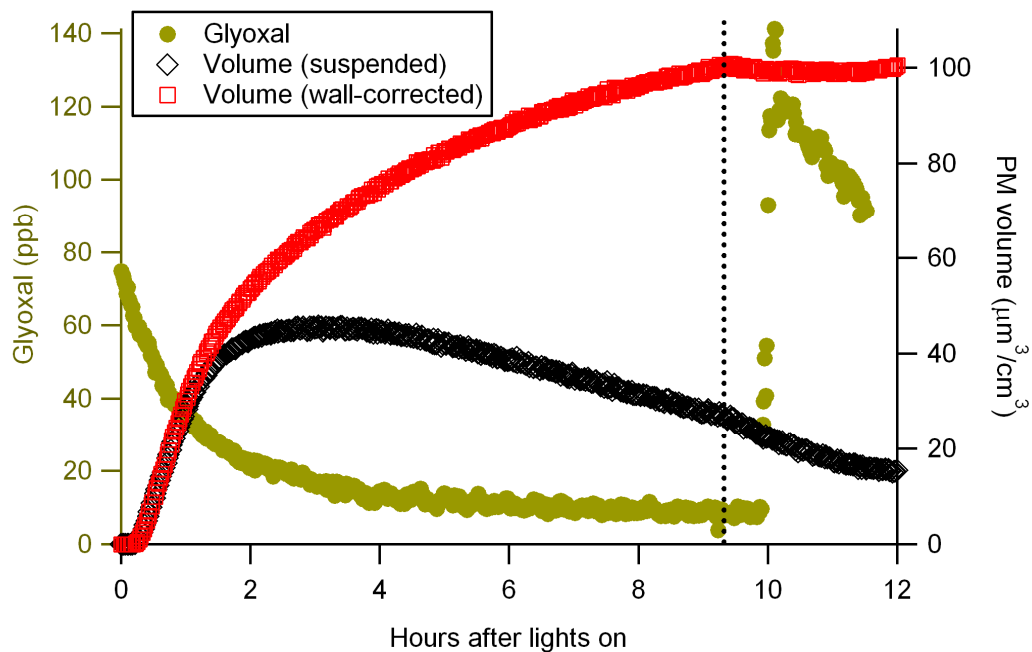
Figure 3.5 The time traces of glyoxal and particle volume concentration (suspended and wall-loss corrected) (EPA1501A). The dashed line indicates the time blacklights were turned off. Addition of glyoxal (~100 ppb) at 10 hours into SOA seed system did not form significant SOA.
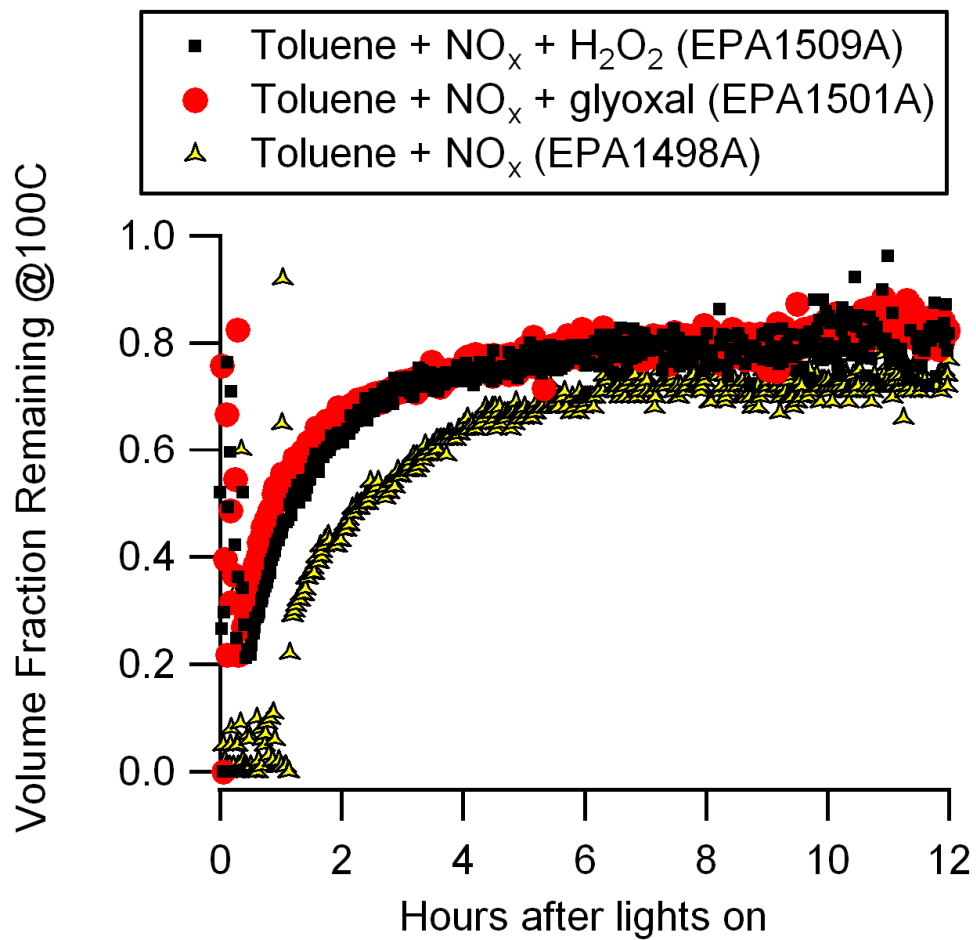
Figure 3.6 The time traces of particle volume fraction remaining at 100°C. Addition of both glyoxal and $H_2O_2$ resulted in faster reaction and slightly less volatile particles, indicating that glyoxal acted as a radical source.

The equation shown on the figure:

$$\text{Volume Gf} = 9.14 \times 10^{-5} \times [\text{RH}(\%)]^2 - 5.39 \times 10^{-3} \times [\text{RH}(\%)] + 1.06$$
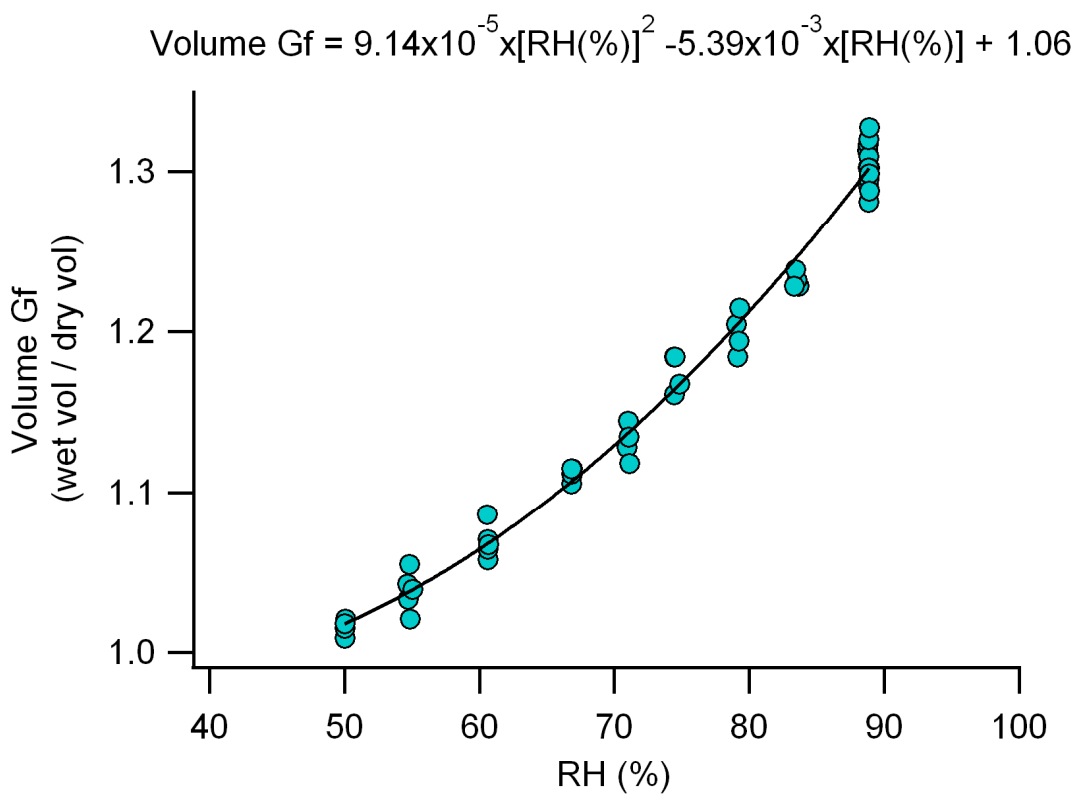
Figure 3.7 Humidogram of SOA formed by the photooxidation of toluene + $NO_x$ under a dry condition (Run 1499B).
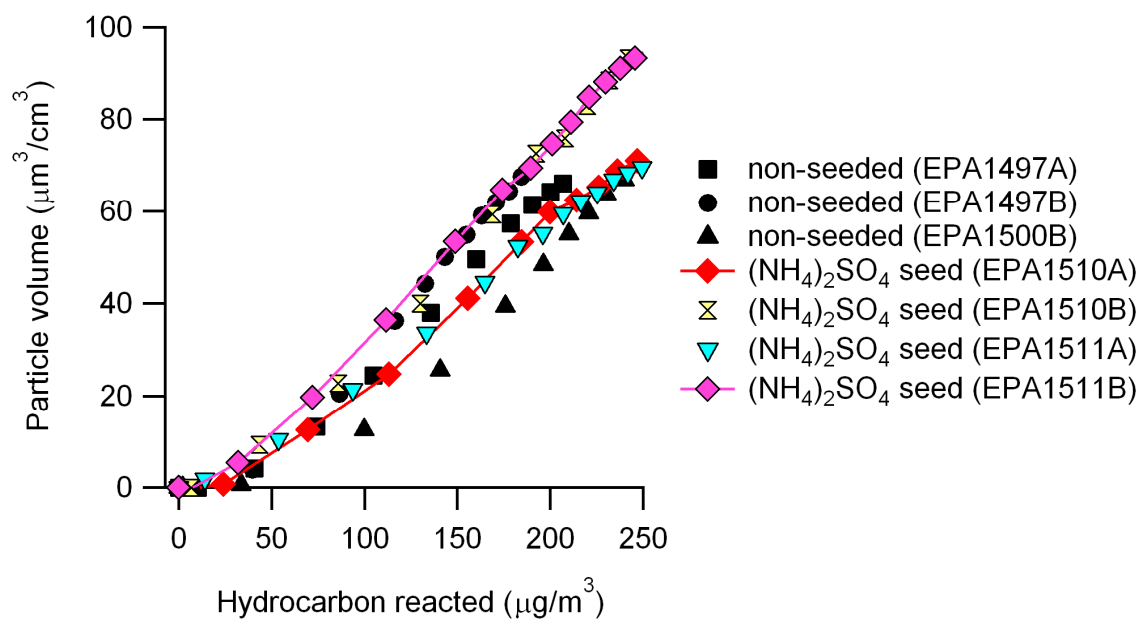
Figure 3.8 SOA growth curves (particle volume vs. toluene reacted) of non-seeded experiments and deliquesced ammonium sulfate seed experiments. No significant difference in particle growth between those two systems was observed, indicating that contribution from glyoxal uptake onto deliquesced ammonium sulfate was minor in this system.
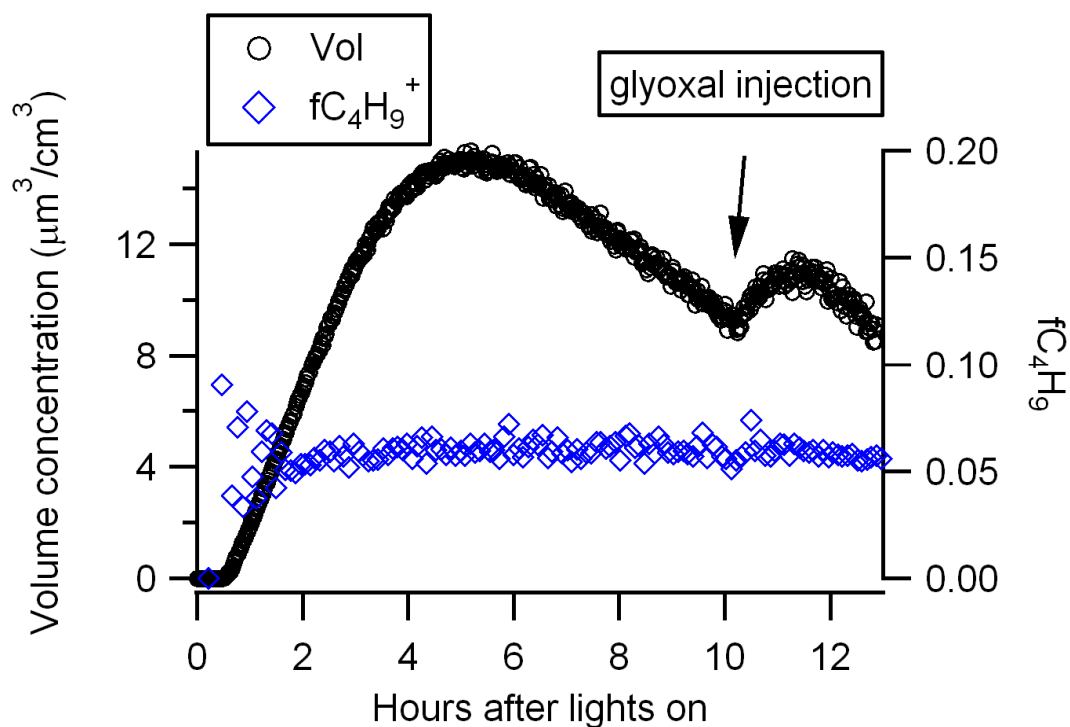
Figure 3.9 The time traces of particle volume formed from 2-tert-butylphenol photooxidation and $C_4H_9^+$ fragment in particles (EPA1489A). Particle volume increased immediately after glyoxal injection while the fraction of $C_4H_9^+$ in organics was unaffected, indicating the increase of particle volume was due to enhanced reaction of 2-tert-butylphenol, as opposed to glyoxal uptake.

# 4 Real-Time Aerosol Density Determination Utilizing a Modified Scanning Mobility Particle Sizer – Aerosol Particle Mass Analyzer System

## 4.1 Introduction

In environmental chamber experiments, aerosol density is required to convert size distribution data into mass concentrations. Early environmental chambers, in the absence of density measurements, estimated mass loadings assuming an aerosol density equal to 1 g/cm$^3$. Many SOA studies have characterized SOA (Jaoui et al., ; Surratt et al., 2006; Yu et al., 1999). However, the data concerning the density associated with these aerosol are limited and vary widely. Recent studies have estimated secondary organic aerosol (SOA) densities ranging from 0.9 g/cm$^3$ to 1.6 g/cm$^3$ for a variety of SOA forming systems (Bahreini et al., 2005; Jaoui et al., 2004; Kalberer et al., 2000; Kostenidou et al., 2007; Surratt et al., 2006; Yu et al., 1999; Zelenyuk et al., 2008). Of particular interest is the wide variability in reported data from similar experimental conditions. For example, Bahreini et al. (2005) have reported the density from β-pinene ozonlysis in unseeded experiments of 1.20 g/cm$^3$. However, Kostenidou et al. (2007) reported the average aerosol density from this same system under similar experimental conditions as 1.41-1.50 g/cm$^3$. The first aerosol density measurements were obtained using pycnometers, however the data collection was slow and of low quality (Hanel and Thudium, 1977). Kelly and McMurry (1992) used a combination of a Differential Mobility Analyzer (DMA) and impactor allowing for size segregated densities to be determined with fairly

good accuracy (Kelly and McMurry, 1992). More recently, density is reported using particle time of flight (PTOF)–SMPS and APM-SMPS comparisons (Jimenez et al., 2003; Kostenidou et al., ; McMurry et al., 2002; Song et al., 2007). Furthermore, recent work by Shilling et al. (2008) has shown aerosol vacuum effective densities from α-pinene ozonolysis are a function of the mass loading. The relationship between mass loading and aerosol density is thought to arise from the relative contribution of highly oxygenated species to the total aerosol mass. Shilling reported densities ranging from 1.73 g/cm$^3$ at a mass loading of 0.46 μg/m$^3$ to 1.23 g/cm$^3$ at mass loadings of 15.9 μg/m$^3$. This work evaluates high time resolution density evolution for SOA as it evolves for two classic SOA experiments. We also evaluate density estimates using AMS-SMPS to the more direct APM-SMPS measurements.

## 4.2    Vacuum Effective Density

Use of PTOF instruments for measurement of aerosol size has been in existence for some time (Sinha). Aerosol mass spectrometers such as the Aerosol Time of Flight Mass Spectrometer (ATOFMS, TSI) and the AMS (Aerodyne) are two common instruments with PTOF modes that report vacuum aerodynamic diameter. Used in combination with a SMPS, these time of flight sizing instruments allow for determination of the vacuum effective density based upon the electrical mobility diameter (SMPS, operating in the transition regime) and the vacuum aerodynamic diameter (operating in free molecular regime) using the following equation (DeCarlo et al., 2004)

$$\frac{d_m}{C_c(d_m)} = \frac{\dfrac{d_{va}\chi^v\chi^t\rho_0}{\rho_p}}{C_c\left(\dfrac{d_{va}\chi^v\rho_0}{\rho_p}\right)}$$ (4.1)

where $d_m$ is the electrical mobility diameter as measured by the SMPS, $C_c$ is the Cunningham slip correction factor, $d_{va}$ is the vacuum aerodynamic diameter, $\chi^v$ is the vacuum dynamic shape factor, $\chi^t$ is the transition regime dynamic shape factor, $\rho_0$ is unit density (1 g/cm$^3$), and $\rho_p$ is the particle density. In the free molecular regime, the Cunningham slip correction factor is approximated as

$$C_c(d) \approx \frac{2\lambda}{d}(\alpha + \beta)$$ (4.2)

where $\lambda$, $\alpha$, and $\beta$ are empirically determined constants (Allen and Raabe, 1982).

Chamber aerosol is commonly assumed to be spherical, leading equation 1 to simplify to (DeCarlo et al., 2004)

$$\rho_p = \frac{d_{va}}{d_m}\rho_0.$$ (4.3)

### 4.2.1    DMA-APM Density Calculation Theory

Ehara and Shin (1996) developed an aerosol particle mass analyzer (APM) which enables selection of aerosol based on mass by balancing the centrifugal and electrostatic forces on a particle passing through a small annular gap between two cylinders. A differential voltage applied between the two cylinders with the outer cylinder rotating at a set angular momentum, classifies particles according to mass described by the following equation

$$m_p \omega^2 r = \frac{\pi d_m^3}{6} \rho_p \omega^2 r = neE_{APM} = \frac{neV}{r \ln\left(r_1 / r_2\right)} \quad (4.4)$$

where $m_p$ is the mass of the particle, $\omega$ is the angular rotational speed, $r$ is the radial

distance from the axis of rotation to the annular gap, $d_m$ is the mobility diameter, $\rho_p$ is the

particle density, $n$ is number of elementary charges per particle, $e$ is the unit electrical

charge, $E_{APM}$ is the magnitude of the electric field applied between the two cylinders, $V$ is

the voltage applied to the APM, $r_1$ is the radius of the outer cylinder, and $r_2$ is the radius

of the inner cylinder.

The APM, in series with a DMA, allows for direct determination of mobility effective

density.

$$\rho_{eff} = \frac{m_p}{\frac{\pi d_m^3}{6}} \quad (4.5)$$

Traditionally, the DMA has been placed ahead of the APM to first select the aerosol

based on electrical mobility followed by the APM mass to charge classification (Figure

4.1). The DMA-APM configuration was successfully utilized by McMurry et al. (2002)

who sampled ambient particles from Atlanta and laboratory generated particles. However,

when diameters are changing rapidly, as in aerosol chamber experiments, the DMA-APM

setup suffers from the slow APM response due to long settling times when $\omega$ or applied

voltage is changed. For example, an α-pinene/ozone (100 ppb α-pinene/ 350 ppb ozone)

experiment will have particle diameter growth rate of change of approximately 2 nm/min

during the first 2-3 hours of an experiment. The traditional DMA-APM transmission

curve incorporates discrete data points associated with step changes in the applied voltage

within the APM, after which, one must wait for the CPC to produce a reading. Therefore, in order to obtain an APM transmission curve, a time of approximately 35 minutes is required using default parameters. An additional problem commonly encountered in environmental chamber experiments using the traditional DMA-APM is the low signal to noise ratio due to the narrow transfer function of the DMA.

## 4.3 Modified APM-SMPS System

We have reversed the order of the traditional DMA-APM system to reduce sampling time, reduce the need to vary $\omega$ or V, and to take advantage of the rapid classifying properties of the SMPS (Figure 4.2). An additional advantage of this setup is that it makes use of the broader transfer function of the APM to increase the system signal to noise ratio. The SMPS used is built in house (scan time = 60 sec, voltage range negative 40 to negative 7000, TSI 3081L DMA, TSI 3077 Kr[85] neutralizer, and TSI 3771 particle counter), allowing for sizing of particles from 28-730 nm. The APM (Kanomax model 3600) is capable of angular rotation speeds up to 10000 rpm and electrical potential up to 5000 V, enabling selection of particles as light as 0.01 fg (particles of ~ 26 nm assuming unit density and perfect spheres). In addition to reversing the SMPS and APM order, custom Labview[®] programming was developed to enable continuous operation of both the APM and SMPS.

Signal to noise is improved by utilizing a independent SMPS, which identifies the mode particle diameter of the aerosol sampled and relays this information to the APM-SMPS. The mass of the particles to be transmitted through the APM is estimated using the information of the mode particle diameter from the independent SMPS and an initial

assumed density (typically 1.2 to 1.4 g/cm$^3$). This estimated mass is then used to set $\omega$

and V of the APM, which are re-evaluated every 4 minutes during the course of an

experiment. The mobility aerosol density is then determined from the mass selected by

the APM (Eq 4.) and the peak diameter from a second SMPS located directly

downstream of the APM.

### 4.3.1 Data Reduction

Mobility size distributions are recorded every 78 seconds along with the corresponding

mass of particles which the APM transmitted. Custom Matlab$^®$ programming enables for

automated fitting of a lognormal curve to the mobility distribution from the SMPS

located downstream of the APM and determination of the mode diameter. The mode

diameter as determined from the lognormal curve is then combined with the recorded

corresponding APM mass to calculate a mobility effective density using equation 5.

### 4.4 Evaluation

The APM-SMPS system performance was first evaluated with 100 nm (as selected by a

DMA) dry ammonium sulfate particles (Sigma-Aldrich, purity > 99%, $\rho$=1.77 g/cm$^3$,)

which were transmitted to the APM-SMPS system in order to ensure the method of

estimating initial densities does not bias the final density calculations. Initial densities

were varied from 1.4-2.2 g/cm$^3$ in 0.2 g/cm$^3$ increments. Figure 4.3 (frame A) shows a

sample of the raw output from this testing with an assumed density of 1.80 g/cm$^3$, results

from this testing revealed no inherent bias in the APM-SMPS, with measured densities

(1.78 to 1.81 g/cm$^3$, Figure 4.3 frame B). Reasons for the slight over estimation of

ammonium sulfate is unknown, however it should be noted that the APM does not have a

shape effect. Never the less, the results from the ammonium sulfate are in reasonable agreement with the published density. Accurate APM-SMPS performance was also confirmed with polystyrene latex spheres (Duke Scientific, $\rho=1.05$ g/cm$^3$) and aerosolized dioctyl phthalate (Sigma-Aldrich, purity $> 99\%$, $\rho=0.985$ g/cm$^3$) in order to evaluate its performance with solid and liquid aerosol (Table 4.1).

## 4.5   Experimental

### 4.5.1   Chamber Experiments

The APM-SMPS system sampled SOA generated from a series of environmental chamber experiments conducted at the UCR/CE-CERT environmental chamber facility. The UC-Riverside/CE-CERT Environmental Chamber has been described in detail elsewhere (Carter et al., 2005). Briefly the facility consists of two 90 m$^3$ Teflon reactors located in a temperature controlled room, which is continuously flushed with purified air. The reactors are attached to a rigid collapsible frame to minimize diffusion of contaminants into the reactors by maintaining a positive differential pressure with respect to the chambers surroundings. The chamber has two banks of black lights (80 lights in total). Each light source emits a sufficiently high 360 nm wavelength photon flux to drive $NO_2$ photolysis. Connected to the chamber are two in house built SMPS's identical to the one detailed above, along with an AMS and APM-SMPS. Compounds of interest are introduced to the chamber by passing a stream of pure $N_2$ over a known volume liquid contained in a glass injection manifold or by flushing pure $N_2$ through a calibrated glass

bulb filled with the gaseous compound to the desired partial pressure. In cases where a ozonolysis experiment was performed, ozone was introduced into the dark chamber by passing 20 psig of pure air through two UV ozone generators, CO was added in sufficient quantities to consume >99 % of the hydroxyl radicals produced. All experiments were conducted in the absence of seed. In all experiments, the relative humidity (RH) was below 0.1%.

## 4.6    Results

### 4.6.1    α-Pinene-Ozone SOA Density

An α-pinene ozonoylsis experiment was conducted at 27 °C (400 ppb α-pinene/ 800 ppb $O_3$/ excess CO as the hydroxyl scavenger). Mass loadings from this experiment were in excess of 2000 μg/m$^3$ as measured by an SMPS. This mass loading is especially high; however during this experiment, the SMPS was programmed to remain at a single voltage (essentially a DMA) so as to transmit only a single diameter particle to the AMS located downstream. Due to the narrow transmission curve of the DMA, large mass loadings were needed to obtain a substantial signal from the AMS. The mobility aerosol density remained a nearly constant $1.24 \pm 0.03$ g/cm$^3$ throughout the course of the experiment (~ 7 hrs) (Figure 4.4). During the course of the same experiment, the vacuum effective density was also determined from a DMA-AMS setup as described above and found to be $1.26 \pm 0.03$ g/cm$^3$. This effective density value closely matches that determined previously from Bahreini et al. (2005), Zelenyuk et al. (2008), and Shilling et al. (2008)

at mass loadings > 15 μg/m$^3$. It is worth noting that in the experiments of Bahreini, initial

hydrocarbon concentrations were approximately an order or magnitude lower than that

reported here and used seed particles, while the experiments of Shilling had initial

hydrocarbon concentrations even lower. In addition to these differences, the experiments

of Shilling contained dry ammonium sulfate seed particles and a relative humidity of

40%. The work of Zelenyuk contained no seed and was conducted at an RH below 1%.

Despite these dramatic differences in experimental conditions, the aerosol density

reported here matches extremely well with that of Shilling (1.23 g/cm$^3$), Zelenyuk (1.198

g/cm$^3$), and Bahreini (1.19 g/cm$^3$). As mentioned previously, Shilling has shown aerosol

density to be a function of the mass loadings, while work of Zelenyuk and Bahreini do

not indicate final mass loadings, it is assumed that they are much lower then those

reported here. Therefore, this may explain the small differences between our results and

those of Zelenyuk and Bahreini.


### 4.6.2    *m*-Xylene NO$_X$ SOA Density

Additional chamber experiments were carried out to examine the aerosol density of SOA

formed from the irradiation of *m*-xylene and NO$_x$ (70 ppb *m*-xylene, and 11 ppb NO),

resulting in a final mass loading of 25 μg/m$^3$. The experiment was conducted in the same

manner to that of the α-pinene/O$_3$ however, the irradiation necessary for the reaction was

provided by the 80 black lights. Additionally, the vacuum effective density during this

experiment was determined using an SMPS in parallel with the AMS. This setup enabled

collection of data from the AMS under the low mass loadings encountered in this

experiment, which would not have been possible with the SMPS upstream of the AMS. The aerosol density measured by both the APM-SMPS and SMPS-AMS follows the α-pinene/$O_3$ trend with little change in the density throughout the experiment except for a slight decrease during the first 4 hours. Similar to the α-pinene/$O_3$ experiments, the APM-SMPS recorded density matched that of the SMPS-AMS, reaching a plateau at a value of $1.35 \pm 0.03$ g/cm$^3$ compared to a value of $1.36 \pm 0.03$ g/cm$^3$ as measured by the SMPS-AMS.

For similar aromatic systems, Alfarra et al. (2006) have reported aerosol density values of $1.35$-$1.40$ g/cm$^3$ from 1,3,5-trimethylbenzene photo-oxidation with $NO_x$, while Martin-Reviejo et al. (2005) reported the density of aerosol generated from benzene at $1.35$ g/cm$^3$. The only work in which density was reported from *m*-xylene was performed by Song et al. (2007) who found the density of the aerosol as $1.41$ g/cm$^3$. It should be noted that the work of Song also employed an APM for density measurements. However, differences in the experimental conditions under which the experiments of Song were performed, namely the absence of $NO_x$ in the reaction system, make drawing conclusions based on differences in these two experiments difficult.

### 4.7    Summary and Discussion

We have demonstrated the applicability of a modified APM-SMPS system for the real-time density analysis of chamber generated SOA. This new system obtains data 30 times faster than a traditional DMA-APM setup. Very little change in aerosol density was observed for α-pinene ozonolysis experiments with densities measured by our APM-

SMPS and SMPS-AMS agreeing well over the course of the entire experiment (1.24 and 1.26 g/cm$^3$ respectively), while in m-xylene experiments a slight decrease in aerosol density was observed during the initial course of the experiment with both an SMPS-APM and SMPS-AMS (1.35 and 1.36 g/cm$^3$, respectively) determined densities agreeing throughout the experiment. Furthermore, in environmental chamber applications, use of the SMPS-AMS is found to be more than adequate for aerosol density determination, with vacuum effective densities agreeing extremely well with those determined from an APM-SMPS setup. Deployment of the APM-SMPS for ambient measurements would present difficulties not encountered here due the externally mixed nature of ambient aerosol. In particular, the broad transfer function of the APM would lead to transmission of multiple masses to the SMPS, additionally the SMPS would observe aerosol with a varied distribution of mobility diameters. However, the results reported here are consistent with previously reported ambient particle densities of 1.0-1.5 g/cm$^3$ (Pitz et al., 2003; Spencer et al., 2007). Furthermore, this method utilizing both AMS and APM data can be extended to examine particle shape factors as described by Schmid et al. (2007), in which a DMA+APM+AMS are setup in series. This method would allow for determination of the mobility and vacuum effective density simultaneously from direct measurements of $d_m$, $m_p$, and $d_{va}$.

## 4.8    References

Allen, M. D., Raabe, O. G.: Re-Evaluation of Millikan Oil Drop Data for the Motion of Small Particles in Air, Journal of Aerosol Science, 13(6), 537-547, 1982

Bahreini, R., Keywood, M. D., Ng, N. L., Varutbangkul, V., Gao, S., Flagan, R. C., Seinfeld, J. H., Worsnop, D. R., Jimenez, J. L.: Measurements of secondary organic aerosol from oxidation of cycloalkenes, terpenes, and m-xylene using an Aerodyne aerosol mass spectrometer, Environmental Science & Technology, 39(15), 5674-5688, 2005

Carter, W. P. L., Cocker, D. R., Fitz, D. R., Malkina, I. L., Bumiller, K., Sauer, C. G., Pisano, J. T., Bufalino, C., Song, C.: A new environmental chamber for evaluation of gas-phase chemical mechanisms and secondary aerosol formation, Atmospheric Environment, 39(40), 7768-7788, 2005

DeCarlo, P. F., Slowik, J. G., Worsnop, D. R., Davidovits, P., Jimenez, J. L.: Particle morphology and density characterization by combined mobility and aerodynamic diameter measurements. Part 1: Theory, Aerosol Science and Technology, 38(12), 1185-1205, 2004

Hanel, G., Thudium, J.: Mean Bulk Densities of Samples of Dry Atmospheric Aerosol-Particles - Summary of Measured Data, Pure and Applied Geophysics, 115(4), 799-803, 1977

Jaoui, M., Kleindienst, T. E., Lewandowski, M., Edney, E. O.: Identification and quantification of aerosol polar oxygenated compounds bearing carboxylic or hydroxyl groups. 1. Method development, Analytical Chemistry, 76(16), 4765-4778, 2004

Jimenez, J. L., Bahreini, R., Cocker, D. R., Zhuang, H., Varutbangkul, V., Flagan, R. C., Seinfeld, J. H., O'Dowd, C. D., Hoffmann, T.: New particle formation from photooxidation of diiodomethane (CH2I2), Journal of Geophysical Research-Atmospheres, 108(D10) 2003

Kalberer, M., Yu, J., Cocker, D. R., Flagan, R. C., Seinfeld, J. H.: Aerosol formation in the cyclohexene-ozone system, Environmental Science & Technology, 34(23), 4894-4901, 2000

Kelly, W. P., McMurry, P. H.: Measurement of Particle Density by Inertial Classification of Differential Mobility Analyzer Generated Monodisperse Aerosols, Aerosol Science and Technology, 17(3), 199-212, 1992

Kostenidou, E., Pathak, R. K., Pandis, S. N.: An algorithm for the calculation of secondary organic aerosol density combining AMS and SMPS data, Aerosol Science and Technology, 41(11), 1002-1010, 2007

McMurry, P. H., Wang, X., Park, K., Ehara, K.: The relationship between mass and mobility for atmospheric particles: A new technique for measuring particle density, Aerosol Science and Technology, 36(2), 227-238, 2002

Pitz, M., Cyrys, J., Karg, E., Wiedensohler, A., Wichmann, H. E., Heinrich, J.: Variability of apparent particle density of an urban aerosol, Environmental Science & Technology, 37(19), 4336-4342, 2003

Sinha, M. P.: Laser-Induced Volatilization and Ionization of Microparticles, Review of Scientific Instruments, 55(6), 886-891, 1984

Song, C., Na, K., Warren, B., Malloy, Q., Cocker, D. R.: Secondary organic aerosol formation from m-xylene in the absence of NOx, Environmental Science & Technology, 41(21), 7409-7416, 2007

Spencer, M. T., Shields, L. G., Prather, K. A.: Simultaneous measurement of the effective density and chemical composition of ambient aerosol particles, Environmental Science & Technology, 41(4), 1303-1309, 2007

Surratt, J. D., Murphy, S. M., Kroll, J. H., Ng, N. L., Hildebrandt, L., Sorooshian, A., Szmigielski, R., Vermeylen, R., Maenhaut, W., Claeys, M., Flagan, R. C., Seinfeld, J. H.: Chemical composition of secondary organic aerosol formed from the photooxidation of isoprene, Journal of Physical Chemistry A, 110(31), 9665-9690, 2006

Yu, J. Z., Cocker, D. R., Griffin, R. J., Flagan, R. C., Seinfeld, J. H.: Gas-phase ozone oxidation of monoterpenes: Gaseous and particulate products, Journal of Atmospheric Chemistry, 34(2), 207-258, 1999

Zelenyuk, A., Yang, J., Song, C., Zaveri, R. A., Imre, D.: A New Real-Time Method for Determining Particles' Sphericity and Density: Application to Secondary Organic Aerosol Formed by Ozonolysis of alpha-Pinene, Environmental Science & Technology, 42(21), 8033-8038, 2008

## 4.9    Tables


Table 4.1 Comparison of densities of various laboratory generated particles as measured by the modified APM-SMPS and SMPS-AMS

| APM-SMPS | Ave. (g/cm$^3$) | S.D. (g/cm$^3$) | n | RSD (%) | reported density (g/cm$^3$) | error (%) |
|---|---|---|---|---|---|---|
| (NH$_4$)SO$_4$ | 1.81 | 0.04 | 15 | 2.0 | 1.77 | 2.4 |
| PSL | 1.04 | 0.02 | 18 | 2.0 | 1.05 | -0.8 |
| DOP | 0.97 | 0.01 | 7 | 1.3 | 0.99 | -2 |
| SMPS-AMS | | | | | | |
| PSL | 1.07 | | 9 | | 1.05 | 1.9 |
| DOP | 0.98 | 0.03 | 4 | 3.3 | 0.99 | -0.8 |

## 4.10  Figures



| Aerosol Source | DMA | APM | Condensation Particle Counter (CPC) |
|---|---|---|---|
| | DMA classifies aerosol based on electrical mobility | APM classifies narrow size distribution based on mass | CPC counts number of particles that pass through DMA-APM |
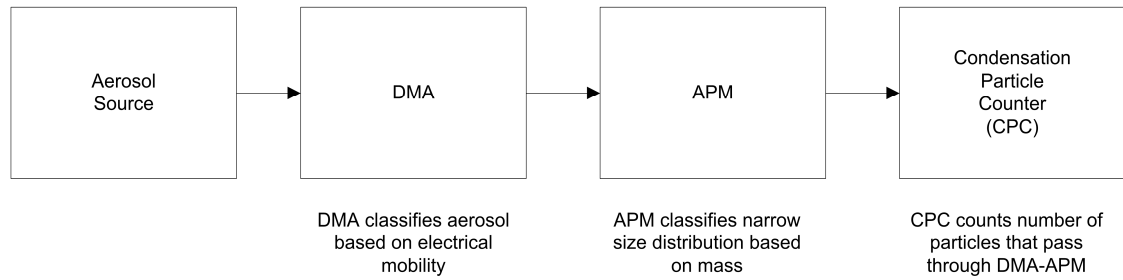
Figure 4.1 Typical DMA-APM setup indicating units and functions of each unit
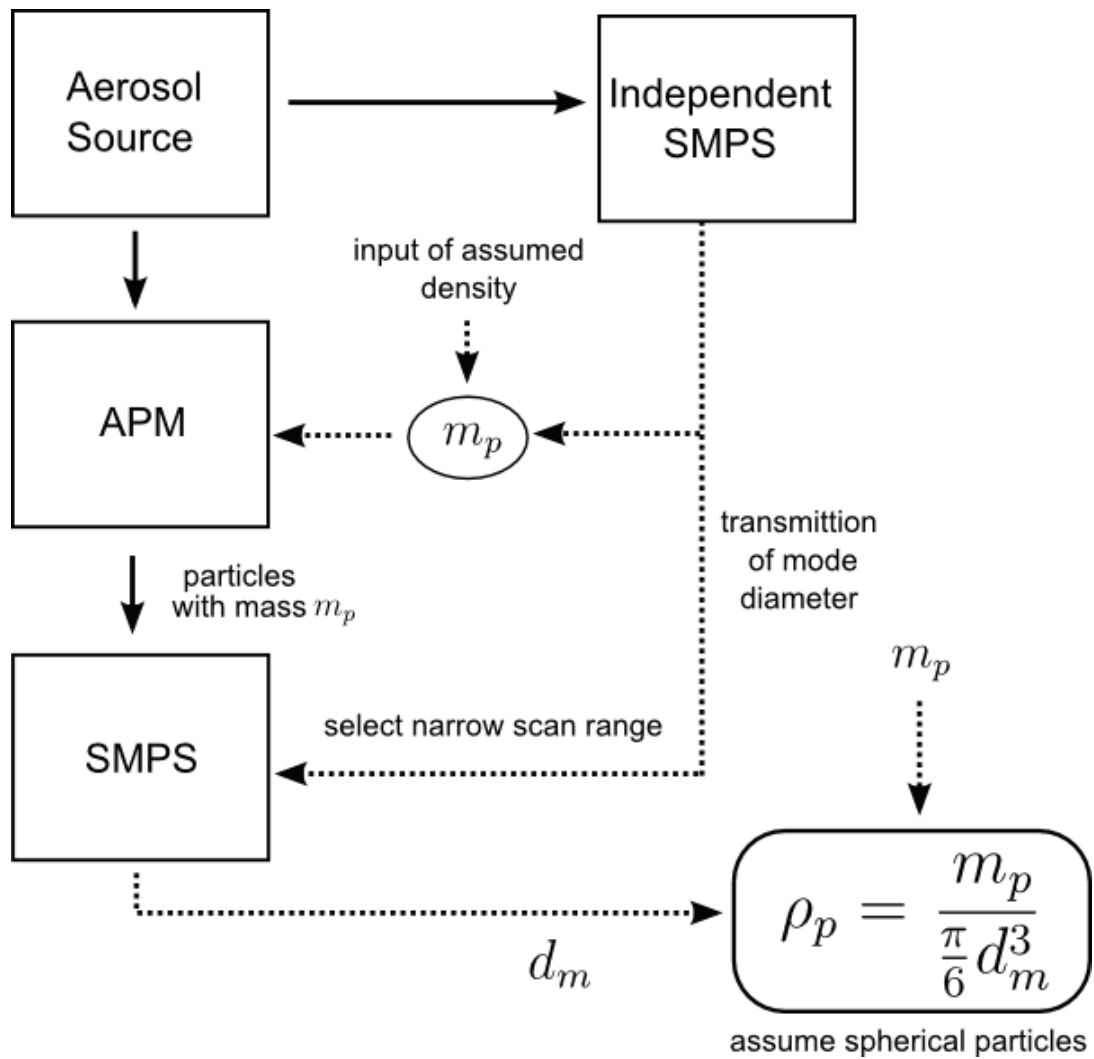
Figure 4.2 Modified APM-SMPS setup indicating placement of units and functions of each unit along with inputs needed. Solid lines indicate flow of aerosol, dotted lines represent flow of data. Note ρp is only equal to the true particle density if the aerosol is spherical, otherwise it is a measure of the mobility effective density
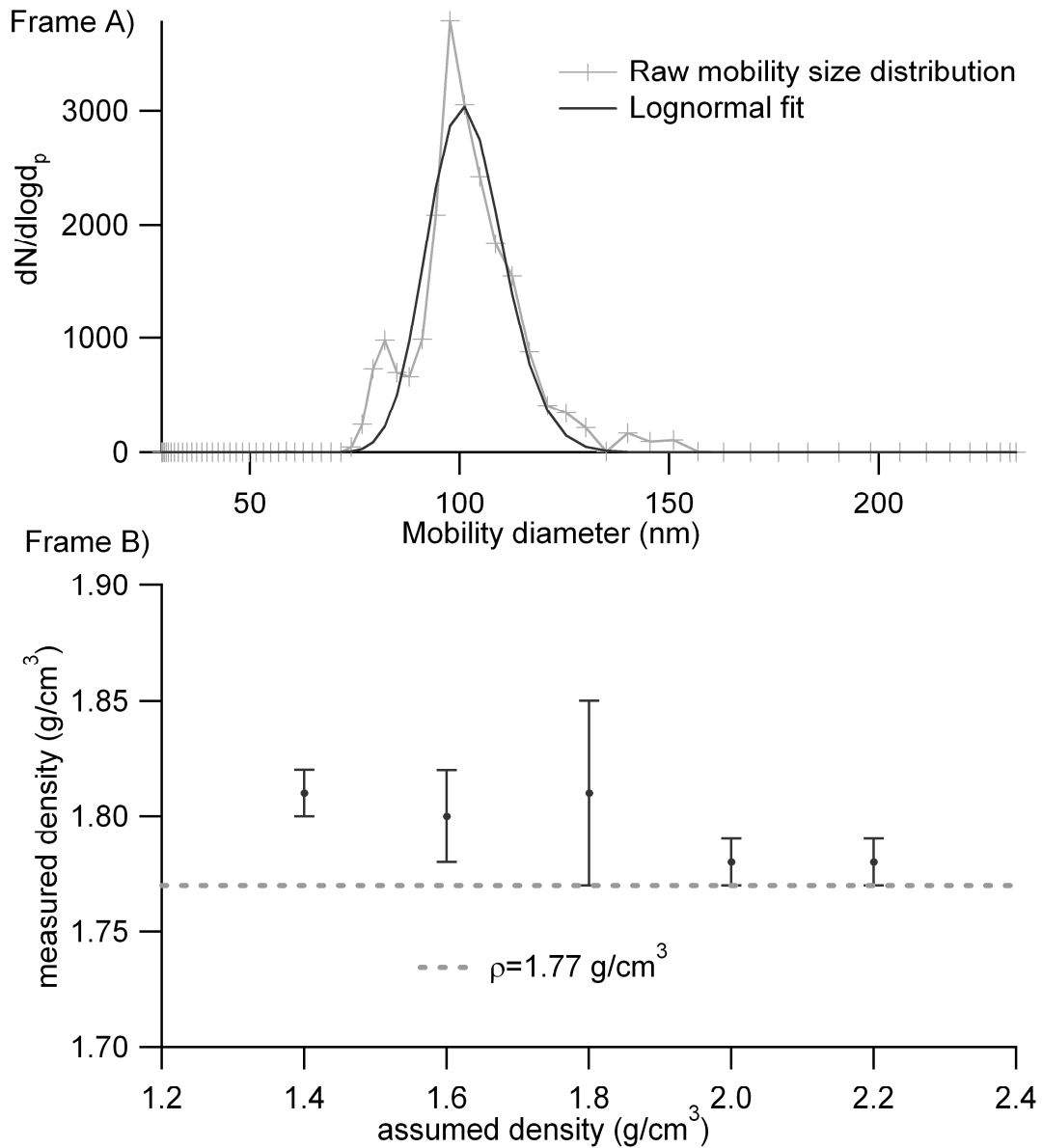
Figure 4.3 Frame A) Mobility size distribution of 100 nm ammonium sulfate particles (assumed density equal to 1.80 g/cm3) after passing through an APM set to transmit particles of 0.942 fg. Frame B) APM-SMPS validation results indicating good agreement between measured density and true density of dry ammonium sulfate and the insensitivity of the system to initial assumed density
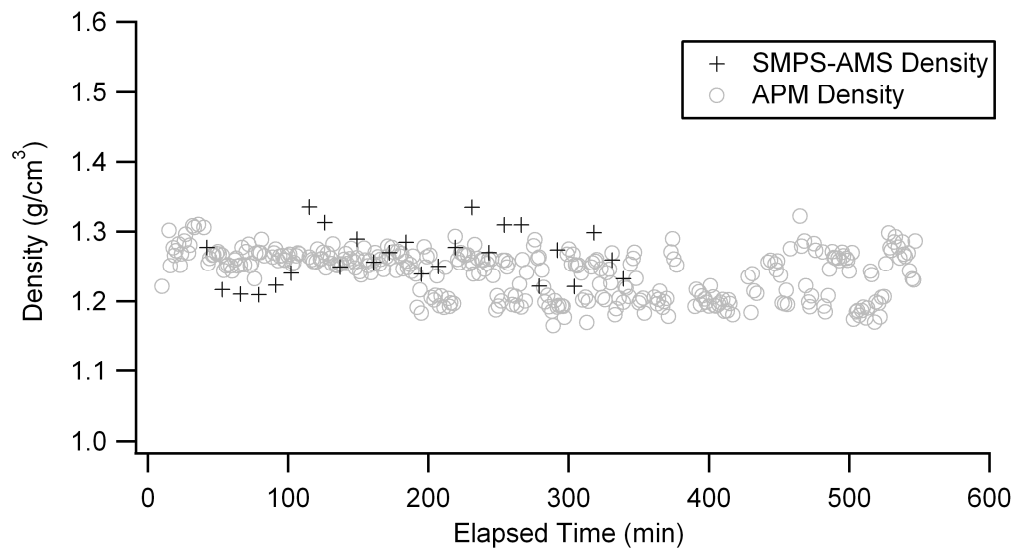
Figure 4.4 Aerosol density for an α-pinene/O3 experiment as measured by the APM-SMPS and an SMPS-AMS setup
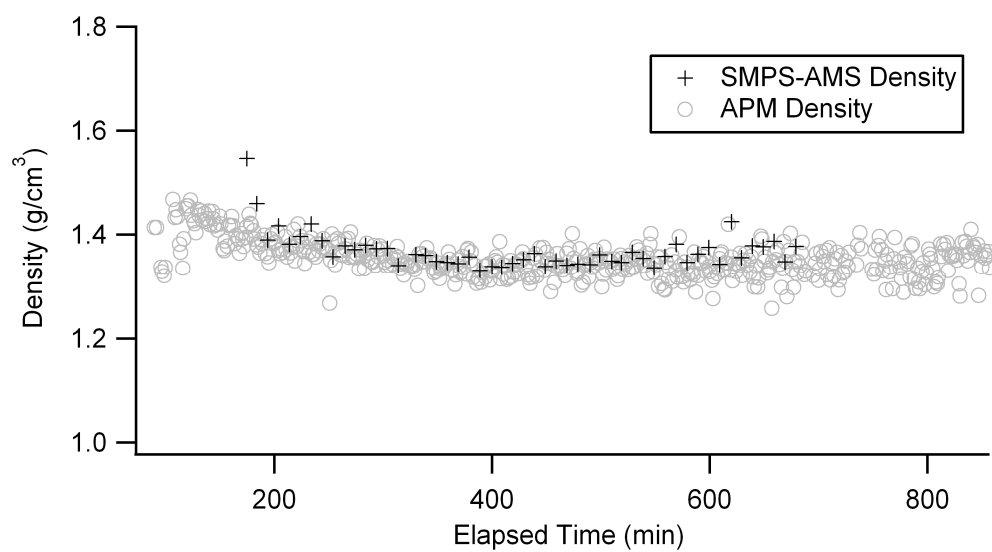
Figure 4.5 Aerosol density for and m-xylene/NOx experiment as measured by the APM-SMPS and an SMPS-AMS setup

# 5 Density and elemental ratios of secondary organic aerosol: application of a density prediction method

## 5.1 Introduction

Aerosol contributes to climate change and adversely affects air quality (Seinfeld and Pandis, 2006). SOA volume concentration formed in environmental chambers or flow tube reactors are often quantified using a scanning mobility particle sizer (SMPS) based on particle electrical mobility diameter. Current air quality regulation for aerosol is based on mass concentrations (e.g., National Ambient Air Quality Standards for annual $PM_{2.5}$ concentration $< 15$ μg/m$^3$), hence particle effective density is necessary to convert SOA volume concentrations to mass concentrations. Density must to be estimated when a direct measurement is not available; however, the estimation of the density of organic aerosols is highly uncertain, mostly due to lack of chemical identification (Hallquist et al., 2009).

Kuwata et al.(2011) proposed an estimation method for density of organic material based on elemental ratios (O/C and H/C) determined by an Aerodyne High-Resolution Time-of-Flight Aerosol Mass Spectrometer (HR-ToF-AMS) (DeCarlo et al., 2006). Considering the recent wide-spread use of the HR-ToF-AMS in the aerosol science community, the estimation method has the potential to be applied to a large number of laboratory and field studies. However the experimental verification of the semi-empirical relationship

was limited to a selective few biogenic systems (isoprene, α-pinene, central Amazon Basin); therefore, further verification covering an expanded range of systems is needed. This study aims to evaluate the applicability of the Kuwata et al (2011) estimation method to 23 different SOA forming systems, including oxidation of aromatic hydrocarbons, phenolic compounds, and biogenic compounds.

## 5.2   Experimental

### 5.2.1   Environmental chamber

All experiments were conducted in the UC Riverside/CE-CERT environmental chamber described in detail in Carter et al. (2005). In short, this facility consists of dual 90 m$^3$ Teflon® reactors suspended by rigid frames in a temperature controlled enclosure (27 ± 1 °C) continuously flushed with dry purified air (a dew point below -40 °C) air generated by an Aadco 737 series (Cleves, Ohio) air purification system. Blacklights (272 bulbs, 115 W Sylvania 350 BL, $NO_2$ photolysis rate 0.4 min$^{-1}$) are used as the light source for all the photooxidation experiments reported herein; ozonolysis experiments were carried out in the dark.

### 5.2.2   Gas and particle analysis

The Agilent 6890 Gas Chromatograph – equipped with a flame ionization detector was used to measure concentrations of precursor hydrocarbons and an inert tracer (perfluorohexane). Analytical conditions are described elsewhere (Nakao et al., 2011ab).

Particle effective density was directly measured with an Aerosol Particle Mass Analyzer (APM, Kanomax) (Ehara et al., 1996) coupled to a custom-built Scanning Mobility Particle Sizer (SMPS) (Cocker et al., 2001) in series. A detailed description of the APM-SMPS system and data algorithms are described elsewhere (Malloy et al., 2009; Nakao et al., 2011c). Chemical composition of SOA was monitored by HR-ToF-AMS (DeCarlo et al., 2006); the elemental ratios (O/C, H/C) of SOA were acquired by the elemental analysis (EA) described by Aiken et al. (2008). The default species list in the high-resolution data analysis toolkit, PIKA (v1.08) was used for EA.

### 5.2.3    Chamber experiments

The reactants used for the chamber experiments are summarized in Fig. 1. NO (UHP grade, Matheson) was used for $NO_x$ photooxidation experiments. All other chemicals were purchased from Sigma-Aldrich at the highest purity available. All experiments were performed under dry (RH<0.1%) conditions. The experimental procedure has been described elsewhere (Nakao et al., 2011ab; Tang et al., 2012). Reactants were oxidized under the following three conditions: 1) photooxidation in the presence of $NO_x$, 2) photooxidation using $H_2O_2$ (50wt% solution in water) as a radical source, or 3) dark ozonolysis. Produced SOA concentrations were typically within 5~150 $\mu g/m^3$.

### 5.2.4    Density prediction method

Previous methods to estimate material density require information on chemical structures (e.g., Girolami, 1994), which is practically infeasible for SOA consisting of many

unknown species (Hallquist et al., 2009). Recently, Kuwata et al. (2011) proposed a semi-empirical relationship between organic material density ($\rho_{org}$), O/C, and H/C as follows:

$$\rho_{org} = \frac{12 + H/C + 16 \cdot O/C}{7 + 5 \cdot H/C + 4.15 \cdot O/C}$$

Eq-1

The relationship was optimized for 31 individual atmospherically relevant organic species with known densities, and was further evaluated against chamber results using two reactants ($\alpha$-pinene and isoprene) and an Amazon field data set. The stated accuracy of the prediction is within 12% (Kuwata et al., 2011). Kuwata et al. (2011) performed calibration of $(CO^+)_{org}$:$(CO_2^+)_{org}$ and $(H_2O^+)_{org}$:$(CO_2^+)_{org}$ fragment ratios of HR-ToF-AMS data as described by Chen et al. (2011). The calibration resulted in enhanced O/C and H/C ratios for three biogenic SOA forming systems (isoprene, $\alpha$-pinene, and $\beta$-caryophyllene) due to higher $(CO^+)_{org}$ and $(H_2O^+)_{org}$ than the default values; a possible explanation for higher $(CO^+)_{org}$ and $(H_2O^+)_{org}$ is the fragmentation of multifunctional organic hydroperoxides (ROOH) (Chen et al., 2011).

Since $(CO^+)_{org}$:$(CO_2^+)_{org}$ and $(H_2O^+)_{org}$:$(CO_2^+)_{org}$ calibration resulted in higher O/C and H/C, the impact of the calibration on density prediction using equation 1 needs to be evaluated. The O/C and H/C data reported by Chen et al. (2011) with and without $(CO^+)_{org}$ and $(H_2O^+)_{org}$ calibration is shown in Fig. 2. Although the calibration enhances O/C and H/C, the data points are shifted along the isopleths of density and thus changes in predicted densities are small (within 5%). Since SOA-specific calibration factors for the oxidation products of the 23 different reactants in this study are unavailable, and since

the vast majority of previously reported HR-ToF-AMS data has been acquired without the calibrations described by Chen et al. (2011), this study applies equation 1 without introducing the $(CO^+)_{org}$ and $(H_2O^+)_{org}$ calibration.

## 5.3    Results and Discussion

### 5.3.1    Measurement of SOA density and elemental ratios

The effect of oxidation conditions ($HC:NO_x$, $H_2O_2$, or $O_3$) on SOA density are observed to be minor (Fig.3). Therefore, results were grouped by each reactant without regard for oxidation route in the following discussion. Previous studies reported loading-dependent $\alpha$-pinene SOA elemental composition and density (Kuwata et al., 2011; Shilling et al., 2009); however, in our experimental conditions (SOA concentration: 5~150 $\mu g/m^3$), density and elemental ratios were nearly constant (see Fig. 4; ethyltoluene SOA for example). The different observations could be due to different reactants ($\alpha$-pinene vs. aromatics) and chamber types (continuously mixed flow reactor vs. batch reactor) as well as higher SOA minimum concentrations reported in this study. Measured effective density, H/C, and O/C are shown in Table 1 and Fig. 5. SOA density ranged between 1.06 and 1.47 $g/cm^3$, with phenol yielding the highest SOA density (average: 1.42 $g/cm^3$) and 4-octylphenol the lowest (1.06 $g/cm^3$). The measured density and O/C followed a similar trend; density (and O/C) decreased slightly as the carbon number of reactants increased, except for isoprene. The trend of H/C was opposite to O/C. These observations support previous findings of the correlation between density and the extent of oxidation

of SOA (Katrib et al., 2005). The elemental ratios and densities for benzene, phenol, and catechol SOA were similar, in spite of the different oxygen contents in the three reactants, suggesting that these aromatic SOA were formed via multigenerational reactions and thus the additional oxygen in reactants did not significantly change the oxygen contents of final products.

### 5.3.2 Density prediction vs. measurement

A Van Krevelen diagram with a density color scale is shown in Fig. 6. The region for elemental ratios of ambient organic aerosols (Ng et al., 2011) suggests that densities of ambient organic aerosols range widely from 1.0 to 1.8 $g/cm^3$ as the result of oxidative processing, highlighting the importance of accurate representation of density. Data points generally fell into the region bounded between the line of slope equal -1 (carboxylic acid or alcohol + carbonyl formation) and the line of slope equal -2 (ketone/aldehyde formation). Reasonable agreement of background color and data point color was observed except for high O/C data (phenol, C6).

Predicted densities are compared with measured densities in Fig. 5. The predictions agreed with measurements within 20% for more than 90% of experiments. The 20% accuracy of this study was larger than the 12% accuracy reported by Kuwata et al. (2011), which is due to the much wider range of experimental systems investigated in this study (this study: 23 different reactants, Kuwata et al.: 2 reactants, 1 field data). However, the 20% accuracy is still considered to be reasonable.

As reported by Kuwata et al. (2011), the effect of nitrogen or sulfur containing species on the density prediction needs further investigation. For these experiments, effect of nitrogen is expected to be minor since N/C ratios of SOA in even high-$NO_x$ chamber experiments are small: toluene-high $NO_x$ 0.07, isoprene-high $NO_x$ 0.04 (Chhabra et al., 2011). No reactant in this study includes sulfur and thus the effect of sulfur is not probed.

## 5.4    Conclusion

A recent study proposed a semi-empirical relationship between organic aerosols density, O/C, and H/C (Kuwata et al., 2011). SOA density was a weak function of oxidant used in chamber experiments. This study applied the semi-empirical relationship to the extensive data set of elemental compositions and densities of SOA formed by the oxidation of 23 different reactants including terpenes, aromatic hydrocarbons, and phenolic compounds, in an environmental chamber. The semi-empirical relationship successfully predicted density of SOA within 20% error for more than 90% of experiments; therefore, the range of application has been further extended to include anthropogenic systems.

## 5.5    References

Aiken, A. C., DeCarlo, P. F., Kroll, J. H., Worsnop, D. R., Huffman, J. A., Docherty, K., Ulbrich, I., Mohr, C., Kimmenl, J. R., Sun, Y., Zhang, Q., Trimborn, A. M., Northway, M., Ziemann, P. J., Canagaratna, M. R., Onasch, T. B., Alfarra, M. R., Prevot, A. S., Dommen, J., Duplissy, J., Metzger, A., Baltensperger, U., Jimenez, J. L.: O/C and OM/OC ratios of primary, secondary, and ambient organic aerosols with High-Resolution Time-of-Flight Aerosol Mass Spectrometry, Environmental Science & Technology, 42, 4487-4485, 2008

Carter, W. P. L., Cocker, D. R., Fitz, D. R., Malkina, I. L., Bumiller, K., Sauer, C. G., Pisano, J. T., Bufalino, C., Song, C.: A new environmental chamber for evaluation of gas-phase chemical mechanisms and secondary aerosol formation, Atmospheric Environment, 39, 7768-7788, 2005

Chen, Q., Liu, Y., Donahue, N. M., Shilling, J. E., Martin, S. T.: Particle-Phase Chemistry of Secondary Organic Material: Modeled Compared to Measured O:C and H:C Elemental Ratios Provide Constraints, Environmental Science & Technology, 45(11), 4763–4770, 2011

Chhabra, P. S., Ng, N. L., Canagaratna, M. R., Corrigan, A. L., Russell, L. M., Worsnop, D. R., Flagan, R. C., Seinfeld, J. H.: Elemental composition and oxidation of chamber organic aerosol, Atmos. Chem. Phys., 11(17), 8827-8845, 2011

Cocker, D. R., Flagan, R. C., Seinfeld, J. H.: State-of the art chamber facility for studying atmospheric aerosol chemistry, Environmental Science & Technology, 35(12), 2594-2601, 2001

DeCarlo, P. F., Kimmel, J. R., Trimborn, A. M., Northway, M., Jayne, J. T., Aiken, A. C., Gonin, M., Fuhrer, K., Horvath, T., Docherty, K., Worsnop, D. R., Jimenez, J. L.: Field-deployable, high-resolution, Time-of-Flight Aerosol Mass Spectrometer, Anal. Chem., 78, 8281-8289, 2006

Ehara, K., Hagwood, C., Coakley, K. J.: Novel method to classify aerosol particles according to their mass-to-charge ratio-Aerosol particle mass analyzer, Journal of Aerosol Science, 27(2), 217-234, 1996

Girolami, G. S.: A simple "back of the envelope" method for estimating the densities and molecular volumes of liquids and solids, Journal of Chemical Education, 71(11), 962-964, 1994

Hallquist, M., Wenger, J. C., Baltensperger, U., Rudich, Y., Simpson, D., Claeys, M., Dommen, J., Donahue, N. M., George, C., Goldstein, A. H., Hamilton, J. F., Herrmann, H., Hoffmann, T., Iinuma, Y., Jang, M., Jenkin, M., Jimenes, J. L., Kiendler-Scharr, A., Maenhaut, W., McFiggans, G., Mentel, T. F., Monod, A., Prevot, A. S., Seinfeld, J. H., Surratt, J. D., Szmigielski, R., Willdt, J.: The formation, properties and impact of secondary organic aerosol: current and emerging issues, Atmospheric Chemistry and Physics, 9, 5155-5236, 2009

Katrib, Y., Martin, S. T., Rudich, Y., Davidovits, P., Jayne, J. T., Worsnop, D. R.: Density changes of aerosol particles as a result of chemical reaction, Atmospheric Chemistry and Physics, 5, 275-291, 2005

Kuwata, M., Zorn, S. R., Martin, S. T.: Using Elemental Ratios to Predict the Density of Organic Material Composed of Carbon, Hydrogen, and Oxygen, Environmental Science & Technology, 46(2), 787-794, 2011

Malloy, Q., Nakao, S., Qi, L., Austin, R. L., Stothers, C., Hagino, H., Cocker, D. R.: Real-time aerosol density determination utilizing a modified Scanning Mobility Particle Sizer - Aerosol Particle Mass Analyzer system, Aerosol Science and Technology, 43, 673-678, 2009

Nakao, S., Clark, C., Tang, P., Sato, K., Cocker III, D.: Secondary organic aerosol formation from phenolic compounds in the absence of NOx, Atmos. Chem. Phys., 11(20), 10649-10660, 2011a

Nakao, S., Liu, Y., Tang, P., Chen, C. L., Zhang, J., Cocker III, D.: Role of glyoxal in SOA formation from aromatic hydrocarbons: gas-phase reaction trumps reactive uptake, Atmos. Chem. Phys. Discuss., 11(11), 30599-30625, 2011b

Nakao, S., Shrivastava, M., Nguyen, A., Jung, H., Cocker, D.: Interpretation of Secondary Organic Aerosol Formation from Diesel Exhaust Photooxidation in an Environmental Chamber, Aerosol Science and Technology, 45(8), 954-962, 2011c

Ng, N. L., Canagaratna, M. R., Jimenez, J. L., Chhabra, P. S., Seinfeld, J. H., Worsnop, D. R.: Changes in organic aerosol composition with aging inferred from aerosol mass spectra, Atmos. Chem. Phys., 11(13), 6465-6474, 2011

Seinfeld, J. H., Pandis, S. N.: Atmospheric Chemistry and Physics: From Air Pollution to Climate Change - 2nd ed. New Jersey, A Wiley-Interscience publication. 2006.

Shilling, J. E., Chen, Q., King, S. M., Rosenoern, T., Kroll, J. H., Worsnop, D. R., DeCarlo, P. F., Aiken, A. C., Sueper, D., Jimenes, J. L., Martin, S. T.: Loading-dependent elemental composition of a-pinene SOA particles, Atmospheric Chemistry and Physics, 9, 771-782, 2009

Tang, X., Cocker III, D. R., Asa-Awuku, A.: Are sesquiterpenes good secondary organic cloud condensation nuclei (CCN)?, Atmospheric Chemistry and Physics Discussions, submitted 2012

## 5.6    Table

Table 5.1 Elemental composition, predicted density, and measured density of SOA formed in an environmental chamber

| Parent species | Experimental condition[a] | Elemental ratio[b,c] O/C | Elemental ratio[b,c] H/C | Effective density (g/cm$^3$)[c] AMS EA prediction[d] | Effective density (g/cm$^3$)[c] APM-SMPS measurement | Error (%) | n[e] |
|---|---|---|---|---|---|---|---|
| Isoprene | $NO_x$; $H_2O_2$; $O_3$ | 0.32 ± 0.13 | 1.43 ± 0.13 | 1.20 ± 0.09 | 1.33 ± 0.02 | -10 | 13 |
| Benzene | $NO_x$; $H_2O_2$ | 0.69 ± 0.04 | 1.08 ± 0.07 | 1.58 ± 0.05 | 1.37 ± 0.06 | 15 | 7 |
| Phenol | $NO_x$; $H_2O_2$ | 0.73 ± 0.13 | 1.08 ± 0.15 | 1.60 ± 0.13 | 1.42 ± 0.02 | 13 | 5 |
| Catechol | $H_2O_2$ | 0.73 | 1.04 | 1.62 | 1.37 | 18 | 1 |
| Toluene | $NO_x$; $H_2O_2$ | 0.65 ± 0.05 | 1.24 ± 0.04 | 1.49 ± 0.03 | 1.40 ± 0.02 | 6 | 3 |
| o-/m-Cresol | $NO_x$; $H_2O_2$ | 0.55 ± 0.04 | 1.18 ± 0.03 | 1.45 ± 0.02 | 1.34 ± 0.03 | 8 | 5 |
| Ethylbenzene | $NO_x$; $H_2O_2$ | 0.52 ± 0.09 | 1.35 ± 0.14 | 1.36 ± 0.10 | 1.39 ± 0.08 | -2 | 3 |
| o-/m-/p-Xylene | $NO_x$; $H_2O_2$ | 0.53 ± 0.08 | 1.39 ± 0.08 | 1.35 ± 0.07 | 1.42 ± 0.03 | -5 | 4 |
| 2,4-Dimethylphenol | $NO_x$; $H_2O_2$ | 0.49 ± 0.05 | 1.26 ± 0.02 | 1.38 ± 0.03 | 1.33 ± 0.03 | 4 | 3 |
| Trimethylbenzenes[f] | $NO_x$; $H_2O_2$ | 0.42 ± 0.07 | 1.45 ± 0.12 | 1.26 ± 0.08 | 1.32 ± 0.05 | -5 | 10 |
| o-/m-/p-Ethyltoluene | $NO_x$; $H_2O_2$ | 0.44 ± 0.04 | 1.35 ± 0.05 | 1.31 ± 0.04 | 1.28 ± 0.09 | 2 | 15 |
| n-Propylbenzene | $NO_x$ | 0.48 ± 0.02 | 1.29 ± 0.09 | 1.36 ± 0.04 | 1.31 ± 0.01 | 4 | 2 |
| α-Pinene | $O_3$ | 0.27 | 1.44 | 1.16 | 1.28 | -9 | 1 |
| 2-tert-Butylphenol | $H_2O_2$ | 0.26 | 1.60 | 1.11 | 1.22 | -9 | 1 |
| 4-Octylphenol | $H_2O_2$ | 0.17 | 1.54 | 1.05 | 1.06 | 0 | 1 |
| β-Caryophyllene | $O_3$; $H_2O_2$ | 0.33 ± 0.09 | 1.45 ± 0.09 | 1.20 ± 0.05 | 1.20 ± 0.04 | 0 | 12 |

a: $NO_x$: photooxidation with $NO_x$, $H_2O_2$: photooxidation using $H_2O_2$ as a radical source, $O_3$: ozonolysis
b: molar ratio
c: Average ± standard deviation
d: Density predicted by Eq1
e: Number of chamber experiments
f: 1,2,3-/1,2,4-/1,3,5-Trimethylbenzene isomers
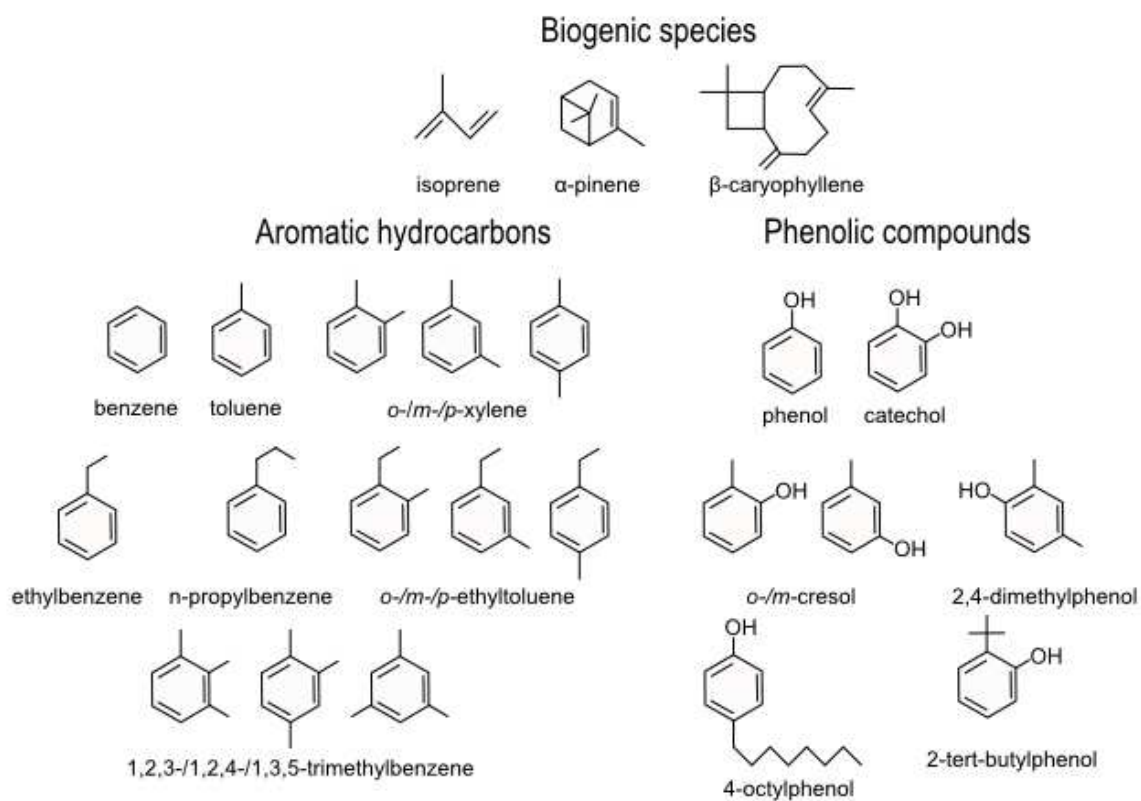
Figure 5.1 Reactants used for chamber experiments
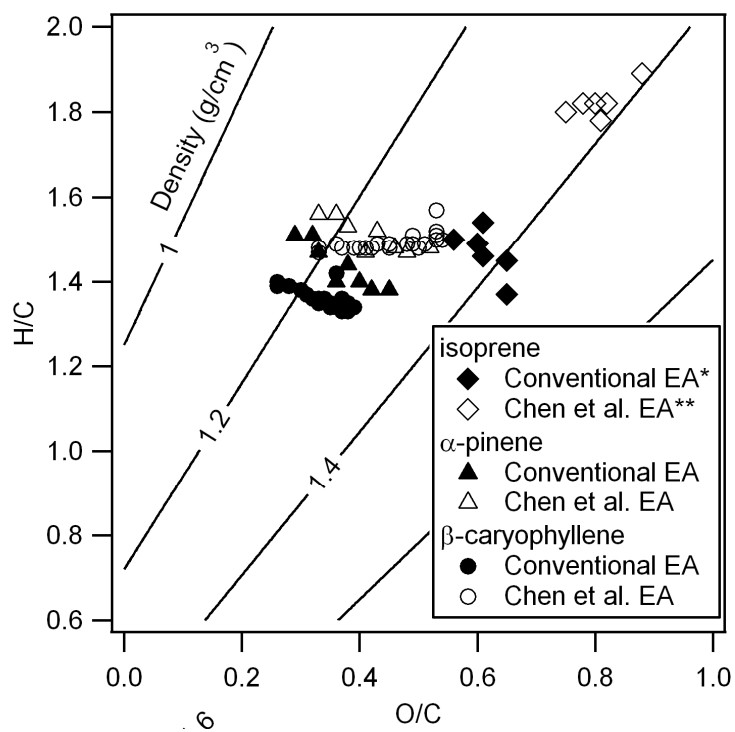
Figure 5.2 Analysis of Chen et al. (2011) data set in terms of density prediction: effect of
$(CO^+)_{org}$ and $(H_2O^+)_{org}$ calibration
*Elemental analysis using the method of Aiken et al. (2008)
**Elemental analysis using the method with $(CO^+)_{org}$ and $(H_2O^+)_{org}$ calibration
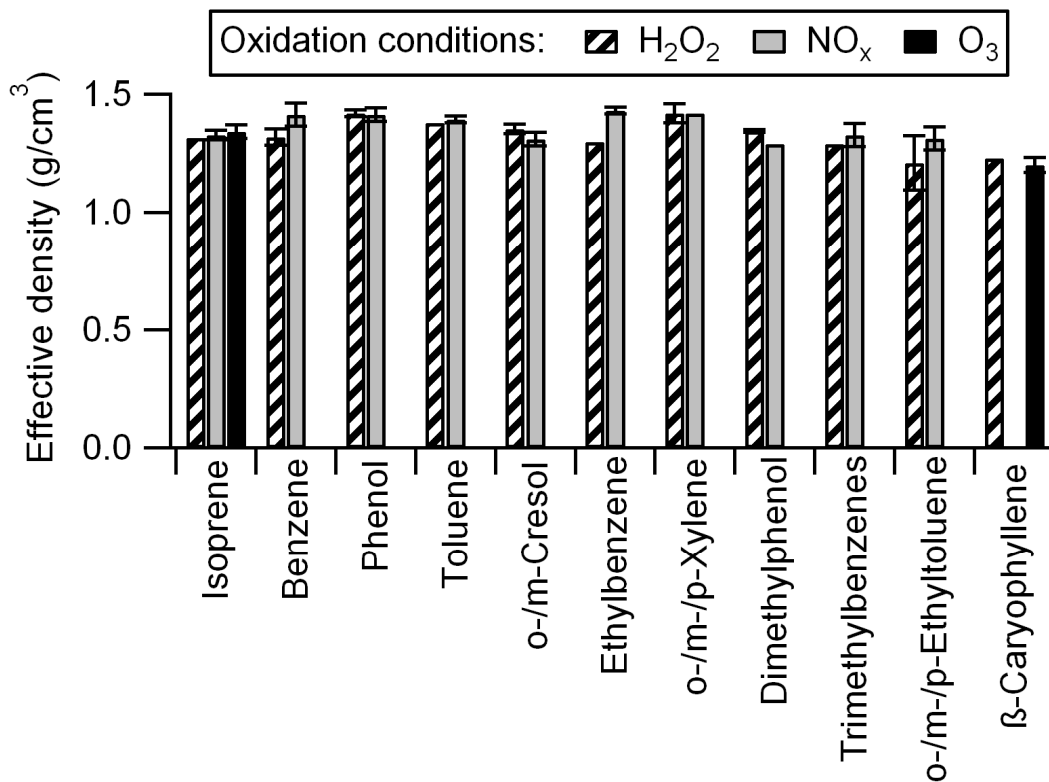
Figure 5.3 Effective density of secondary organic aerosol formed in different oxidation conditions: photooxidation with $NO_x$, photooxidation using $H_2O_2$ as a radical source, and dark ozonolysis.
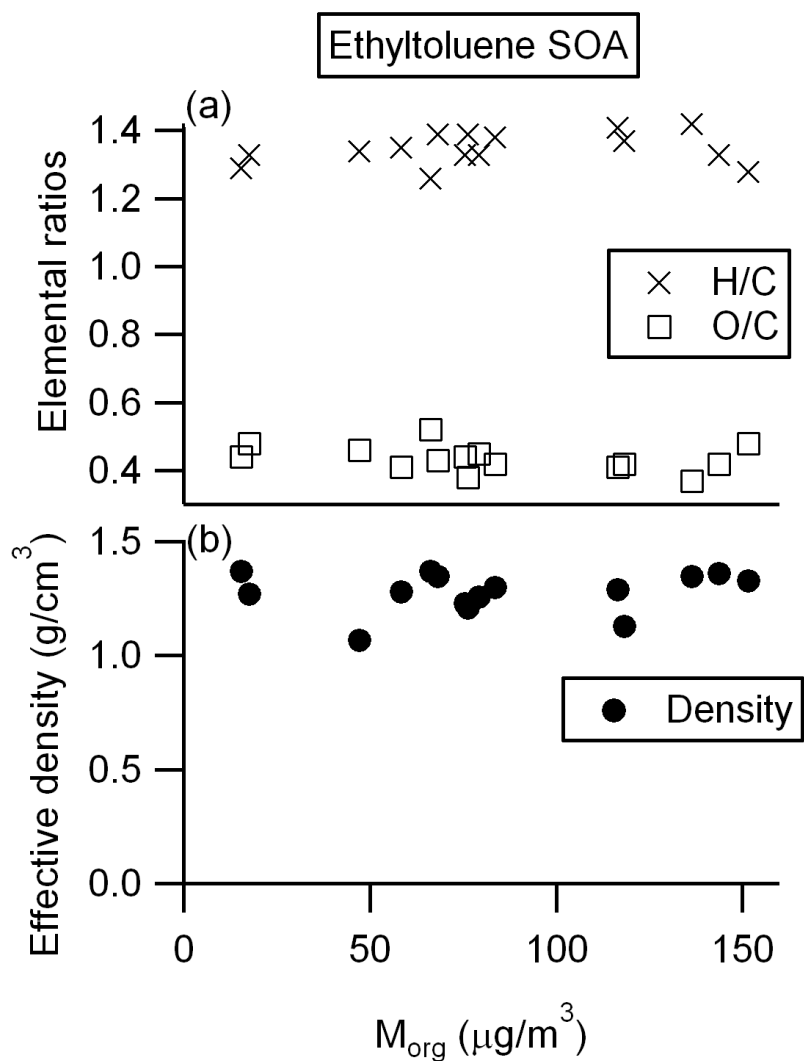
Figure 5.4 (a) Elemental ratios (O/C and H/C) and (b) effective density of secondary organic aerosol formed by oxidation of ethyltoluene isomers as functions of aerosol mass loading ($M_{org}$).

Figure 5.5 Effective density, H/C, and O/C of secondary organic aerosol as functions of carbon number of parent species
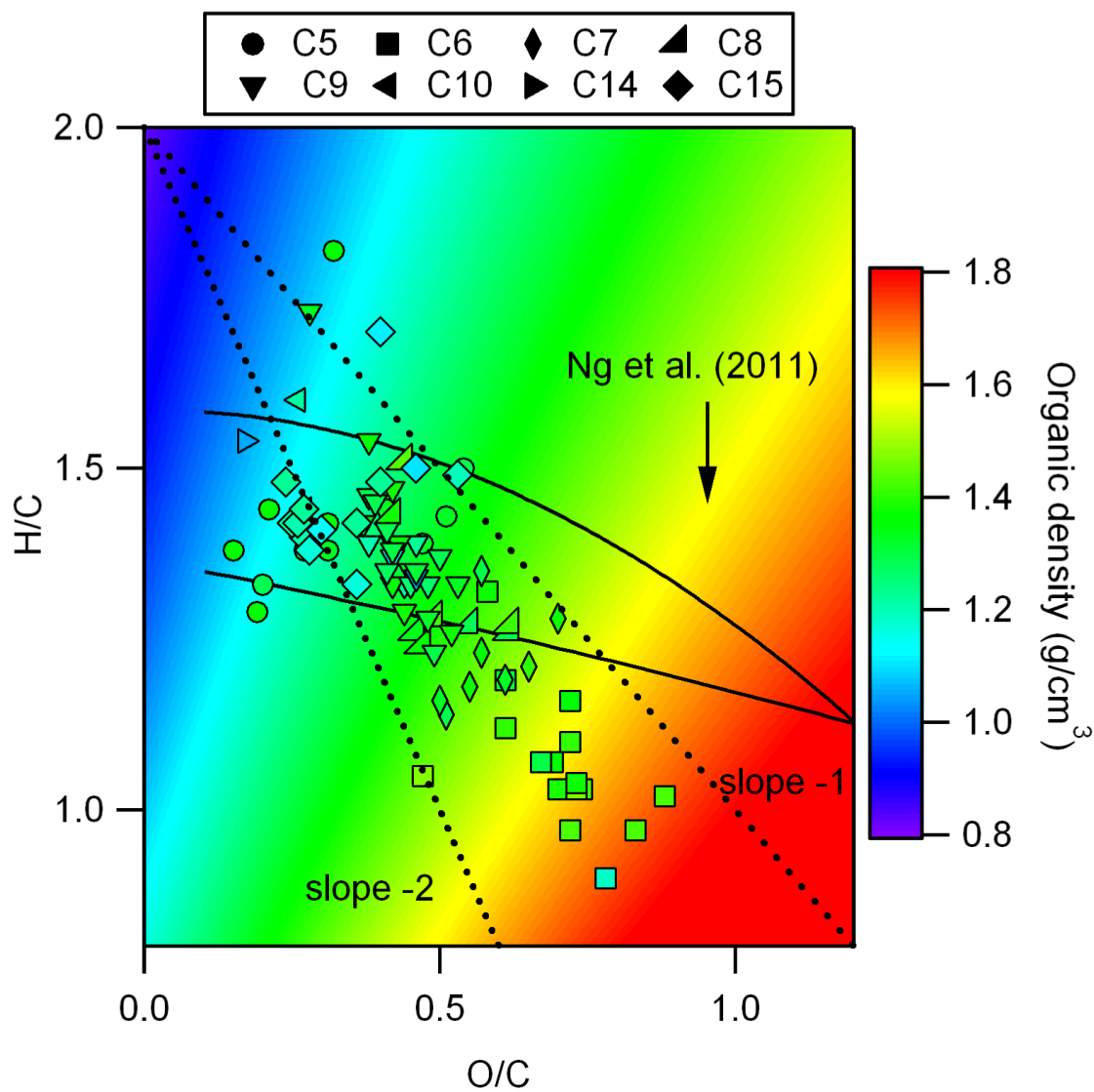
Figure 5.6 Van Krevelen diagram with predicted and measured density of secondary organic aerosol. Ng et al. lines represent range of O/C and H/C of ambient aerosol. Dashed lines represent O/C vs. H/C slopes of -1 and -2. Data point shape represents carbon number of parent species; Data point color and background color represent measured and predicted density, respectively.
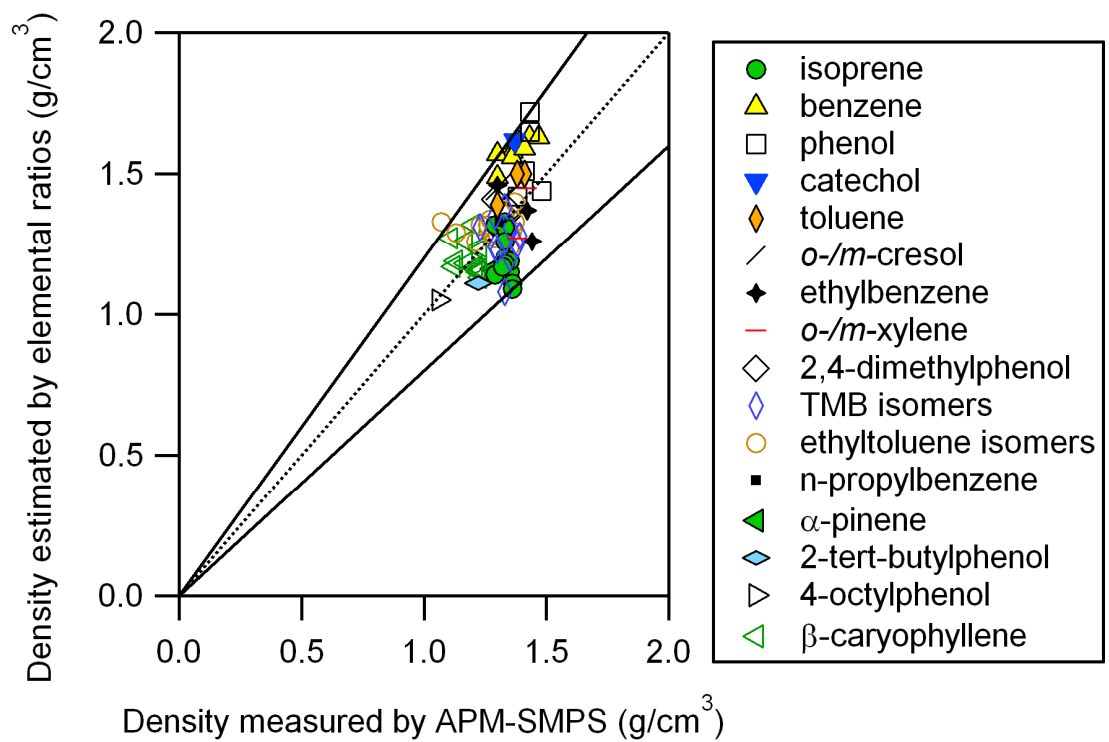
Figure 5.7 Comparison of predicted and measured density of secondary organic aerosol. Solid lines indicate ±20% lines.

# 6 Interpretation of secondary organic aerosol formation from diesel exhaust photooxidation in an environmental chamber

## 6.1 Introduction

Organic aerosol (OA) accounts for ~20-90% of aerosol mass in the lower troposphere (Kanakidou et al., 2005). OA contributes to global climate change (IPCC, 2007; Kanakidou et al., 2005), adverse human health risks (Davidson et al., 2005; Pope and Dockery, 2006), and visibility reduction (Eldering and Cass, 1996). Air quality models using parameters developed from environmental chamber studies severely underpredict OA in the atmosphere pointing towards large uncertainties including "missing precursors" and physico-chemical processes governing formation and evolution of OA in the atmosphere (Volkamer et al., 2006).

OA is classified into two categories: 1) primary OA (POA) that is directly emitted from sources as particles, and 2) secondary OA (SOA) that is formed in the atmosphere from photochemical oxidation of organic vapors followed by gas to particle partitioning. Additionally, semivolatile components of POA evaporate to release semivolatile organic compounds (SVOCs) and intermediate volatility organic compounds (IVOCs), which easily form SOA in the atmosphere due to their lower volatility (Chan et al., 2009; Donahue et al., 2009; Grieshop et al., 2009; Presto et al., 2009; Robinson et al., 2007; Shrivastava et al., 2006). Diesel exhaust is a major source of urban POA (Schauer et al., 1996). Additionally, Robinson et al. (2007) observed rapid and high SOA formation from photooxidation of diesel exhaust in an environmental chamber. However, recent studies

by Samy and Zielinska (2010) and Chirico et al. (2010) observed insignificant SOA formation from diesel exhaust without the addition of radical sources or additional hydrocarbons. As a result, further investigation is required to identify causes of this discrepancy.

The mass of SOA formed from diesel exhaust is often calculated based on increase of wall-loss-corrected particle volume concentration multiplied by a unit density (1.0 g/cm$^3$) with the assumption of spherical particles (Chirico et al., 2010; Robinson et al., 2007; Samy and Zielinska, 2010; Weitkamp et al., 2007). However, this assumption is often not valid for diesel agglomerate particles. Park et al. (2003) and Maricq et al. (2000) reported that effective density decreases as particle size increases because of increasing void space due to agglomeration. Weitkamp et al. (2007) observed that coating SOA onto a fractal-like diesel particle increases particle density.

This study investigated the changes in effective density of diesel agglomerates during partitioning of secondary organic species onto particles. Also, the impact of different dilution methodologies on the diesel particles' effective density evolution in an environmental chamber was investigated for the first time. Furthermore, chemical evolution (aging) of diesel exhaust was examined to evaluate the importance of multi-generational photochemical oxidation of diesel exhaust leading to SOA formation.

## 6.2    Experimental

All experiments were conducted in the mezzanine chamber located at CE-CERT/UC Riverside. A schematic diagram is shown in Figure 7.7.1.  The chamber is in a 2.5 m x 3

m x 7.8 m enclosure covered with reflective aluminum sheets and is illuminated with 170 of 40W blacklights with peak intensity at 350 nm (SYLVANIA, 350 BL) with the $NO_2$ photolysis rate of 0.6 min$^{-1}$. Within this enclosure is a 12 m$^3$ volume 2 mil (50.8 μm) FEP Teflon® chamber. A minimum of 1 m space between the chamber surface and blacklights was maintained to avoid excessive heating at the surface of the film. Additionally, six fans are used to mix the air inside the enclosure with conditioned room air to minimize heating within the enclosure. The enclosure temperature is typically within 25~28°C. Prior to every experiment, the chamber is flushed overnight with pure air (Aadco 737 series air purification system (Cleves, Ohio)). Background particle concentration is below the detection limit of 0.2 cm$^{-3}$.

Dilution of diesel exhaust was performed in two ways: 1) "ejector-dilution" in which a custom built two-stage ejector dilution system as described by Khalek et al. (2000) was used, and 2) "in-chamber dilution" in which raw exhaust was injected into the chamber already filled with clean air. The "ejector-dilution" involves intensive mixing of raw exhaust and compressed clean filtered air. On the other hand, during the "in-chamber dilution", dilution occurs only by slow mixing of the raw exhaust and the clean air inside the chamber. The ejector-dilution is followed by transfer in either a short (2m) or long transfer line (16m, ~5cm I.D., copper) (A and C in Figure 7.1). The in-chamber dilution occurs after transfer of undiluted exhaust in a short transfer line (B in Figure 7.1).

Diesel exhaust was obtained from a Pramac 3.6 kW generator (Yanmar Engine, E3750 MYHDI). This is the similar type of engine as used by Robinson et al.(2007). The engine was connected to a resistive load bank (Swift-E STD, Simplex Inc.). The engine was

operated on ULSD fuel (<15 ppmS) at 50% (medium) load, 30% (low) load, and for idling condition. The engine was warmed-up for45 minutes prior to injection to allow the diesel exhaust to reach steady state.

Particle size distribution between 27 and 685 nm was monitored by a Scanning Mobility Particle Sizer (SMPS) similar to that described by Cocker et al. (2001). Particle sizing was periodically verified by aerosolized polystyrene latex (PSL) particles (90, 220, and 350 nm) (Thermo Scientific, 3000 series Nanosphere Size Standards).

Particle effective density was measured with a Aerosol Particle Mass Analyzer (APM, Kanomax) (Ehara et al., 1996) and a SMPS in series. The APM is located upstream of the SMPS for improved time resolution (~1 minute) over the more common configuration of the Differential Mobility Analyzer (DMA) – APM (Khalizov et al., 2009; McMurry et al., 2002; Xue et al., 2009). A detailed description of the APM-SMPS system and data algorithms are described elsewhere (Malloy et al., 2009). The 0.01~100 fg measurement range of the APM is equivalent to approximately 30 nm to 580 nm for particles with unit density (Kanomax Japan, Inc.). In this study, the APM setting was programmed to select 3~5 different particle masses (typically in 20 minutes) to obtain particle density as a function of particle mass. Fractal-like dimension was obtained by fitting the effective density vs. size relationship into a power function (Park et al., 2003; Xue et al., 2009):

$$\rho_{eff} = Cd_m^{D_f - 3} \tag{1}$$

where $\rho_{eff}$ is the effective density of particles, C is a constant, $d_m$ is the mobility diameter of particles, and $D_f$ is the fractal-like dimension.

Particle volatility was monitored with a volatility tandem differential mobility analyzer (VTDMA), in which monodisperse particles of mobility diameter $D_{mi}$ are selected by the 1st DMA followed by transport through a Dekati® thermodenuder (TD, residence time: approximately 17 seconds, temperature: 100 °C). The particle size after the TD ($D_{mf}$) is then measured by fitting a log-normal size distribution curve from the 2nd SMPS. Volume fraction remaining (VFR) is then calculated as the before and after the TD volume ratio, i.e., VFR = $(D_{mf}/D_{mi})^3$. Note that the "volume" in VFR measurement is based on mobility diameter measurement which includes void spaces in diesel agglomerates, and caution must be taken in using VFR measurements to infer volatility of OA. The VTDMA was calibrated for each diameter setting using VFR of dry $(NH_4)_2SO_4$ seed aerosol and/or diesel particles at room temperature.

The chemical evolution of organic particulates was observed by a high-resolution time-of-flight aerosol mass spectrometer (HR-ToF-AMS) (DeCarlo et al., 2006; Jayne et al., 2000). The operation mode of the HR-ToF-AMS alternated between the mass spectrum (MS) W-mode and the particle time-of-flight (PToF) mode. Only the data from the MS mode is shown in this study. Recently developed elemental analysis (EA) software was used to track atomic ratio (O/C) of non-refractory organic compounds (Aiken et al., 2008). Particle collection efficiency of the AMS is reported to be low for small (<70nm) particles (Jayne et al., 2000). Although the geometric mean diameter (GMD) of the diesel exhaust particles was initially small (<70nm), coagulation and/or preferential wall loss of these small particles caused the GMD to rapidly increase. The GMD during experiments

was typically within 70~200 nm. The reported results of the AMS are relative to the organic and nitrate signals. The sulfate and ammonium signals were negligible (<1%). Ethene concentration was measured by a gas chromatograph – flame ionization detector (GC-FID, Agilent technology 6890) that is equipped with a PLOT column. $NO_x$, CO, and $O_3$ concentration was measured by Teledyne model 200E, 300E, and 400E analyzers, respectively.

## 6.3　Results and Discussion

The engine load, initial concentrations (particle volume based on the SMPS measurement, $NO_x$, and ethene), calculated OH concentration (based on ethene decay rate), $D_f$ , bulk effective density of particles, and dilution ratio are summarized in Table 6.1. The dilution ratio is determined as the ratio of $NO_x$ concentration in the raw exhaust to that in the chamber.

Since the high NO concentration suppresses $O_3$ and $NO_3$ formation and ethene predominantly reacts with OH radical, exponential decay of ethene concentration was used to estimate OH radical concentration. OH concentration was calculated to be 1~2 x $10^6$ molecule cm$^{-3}$, approximately equivalent to the 12-h daytime average ambient OH concentration level (Atkinson, 2000). The OH concentration is in reasonable agreement with Weitkamp et al. (2007) (3 ($\pm$1) x $10^6$ molecule cm$^{-3}$).

Park et al. (2003) reported that particle fractal-like dimension somewhat increased as engine load decreased. Although the $D_f$ in Table 6.1 may indicate the same trend, it is

difficult to draw any conclusion regarding the effect of load on $D_f$ due to the additional

two parameters of the transfer line length and dilution method.

## 6.4 Interpretation of SOA formation

Results of Run 1(short transfer line, ejector-dilution) are summarized in Figure 7.2. Only

a minor increase of particle volume (wall-loss uncorrected) was observed after the black

lights were turned on, (Figure 6.1 (a)). Also, the VTDMA measurement indicated little

change in mobility diameter after passing through the TD that was set at 100°C (Figure

6.2 (b)). However, particle effective densities increased rapidly (approximately 30 to 80%

within 2 hours). The effective density – mobility diameter relationship was fit with a

power function (equation 1) to determine $D_f$ (Figure 6.2 (c)). The $D_f$ rapidly increased

from 2.52 to 2.81±0.06 after turning on the blacklights. The fitted power function was

used to interpolate / extrapolate particle density within the size range of the SMPS

measurement. Particle mass concentration was calculated from particle volume and

effective density as a function of mobility diameter. Calculated particle mass

concentration is shown in Figure 6.2 (a).

The small increase in volume and small change in VFR, but significant increase in

density and mass during SOA formation are consistent with the filling of the void space

of agglomerate particles by SOA. This is further confirmed by placing the TD in front of

the APM-SMPS system (not shown). Aging causes condensation of secondary organics;

hence aged diesel particulates show a greater decrease in effective density after passing

through the TD (compared to fresh particles) as they have more organic mass condensed onto their fractal agglomerate backbone. This demonstrates that particle volume measurement based only on mobility diameter can underestimate SOA formation from diesel exhaust.

The HR-ToF-AMS O/C measurement indicated that oxygenated species rapidly increased after blacklights were turned on (Figure 6.3). Prior to photooxidation, the O/C ratio of the diesel exhaust particulate was 0.05. After the blacklights were turned on, this ratio increased continuously to 0.25 within 12 hours due to condensation of secondary organics onto the diesel agglomerate. The continuous increase of the O/C ratio is consistent with the continuous gas-phase oxidation of diesel exhaust reported by Sage et al. (2008) (based on the profile of m/z 44) and/or the cleavage of C-C bond (fragmentation) of large molecules (Kroll et al., 2011; Kroll et al., 2009). Mass spectrums obtained by HR-ToF-AMS before and after the UV irradiation are shown in Figure 6.4. Increase of m/z 44 (confirmed to be $CO_2^+$ fragment by high resolution analysis) was observed. Also m/z 30 increased, which was largely ascribed to $NO^+$ fragment by high resolution analysis, suggesting that the high $NO_x$ condition applied in this study led to formation of nitrogen containing species.

The AMS has also been used to estimate the contribution of SOA during other diesel exhaust studies (Chirico et al., 2010; Sage et al., 2008; Weitkamp et al., 2007). Sage et al. (2008) used m/z 57 (assumed to be $C_4H_9^+$ ) measured by the quadrupole-AMS (Q-AMS)

as a tracer of primary organic aerosol. Chirico et al. (2010) pointed out that oxygen containing species such as $C_3H_5O^+$ can also contribute to m/z 57. Therefore, they selected $C_4H_9^+$ by utilizing the high resolution capability of the HR-ToF-AMS. In this study, $C_4H_9^+$ was also used as the tracer. As shown in Figure 6.3, $C_3H_5O^+$ significantly contributes to m/z 57 signal. However, the assumption of constant $C_4H_9^+$ / POA ratio should be considered as a rough approximation since mass spectra of POA may change (Chirico et al., 2010) . The fraction of SOA in organics was estimated by the following equation (Chirico et al., 2010):

$$\%SOA\ (t) = [Org\ (t) - (C_4H_9^+\ (t)/C_4H_9^+\ (t_o)) \times Org\ (t_0)] / Org\ (t) \qquad (2)$$

The estimated SOA fraction is shown in Figure 6.2 (d). After 12 hours of irradiation, 80% of organic aerosol was estimated to be SOA.

## 6.5     Effect of injection methods on particle physical structure and evolution

The previous section demonstrated that particle effective density measurement provides critical insight into the physical evolution of fractal particulate inside an environmental chamber. In this section, the impact of dilution method and transfer line length (Figure 6.1) on the measured physical and chemical evolution of diesel exhaust particulate is explored. The particle volume, mass concentration, and bulk effective density (mass concentration / volume concentration) for different injection/dilution conditions are shown in Figure 6.5.

The particle density was observed to be higher when raw exhaust was injected into the chamber (in-chamber dilution) than when dilute exhaust was injected (ejector-dilution) (Figure 6.5 (c)). The initial particle density was expected to be a function of the dilution ratio of the exhaust with more significant evaporation of semivolatile hydrocarbons occurring at a larger dilution ratio. However, the bulk effective density at varying dilution ratios (e.g., Runs 1~4, Figure 6.6) prove that dilution ratio by itself could not explain the low density in the ejector-dilution experiment (Run 1). The density difference between in-chamber dilution and ejector-dilution experiments also could not be ascribed solely to the size dependence of density (e.g., Figure 6.2 (c)) since the initial particle sizes did not systematically differ between dilution methods.

The differences in initial density values suggest that the relatively stagnant in-chamber dilution resulted in slower evaporation of semivolatiles compared to the ejector dilution. The ejector system creates rapid, turbulent dilution of diesel exhaust with purified compressed air; this pre-diluted exhaust subsequently fills the empty chamber resulting in additional turbulence during the filling process. This may lead to faster evaporation of semi-volatiles compared to the relatively stagnant method of injecting a puff of raw exhaust into chamber already filled with clean air. The previous work by Lipsky and Robinson (2005) showed an evaporation timescale of 2.5 seconds for diesel exhaust in a dilution sampler designed to induce turbulent mixing; Grieshop et al. (2009) showed that the evaporation timescale of lubrication oil aerosols in a chamber was in the order of hours. This contrast suggests that evaporation of semivolatiles was kinetically inhibited,

and hence, a more turbulent dilution method may enhance desorption of semi-volatiles from fractal agglomerates. To our knowledge, this is the first time two different methods of dilution and filling of an environmental-chamber have been compared, and resulting effects on particle effective density investigated.

In Runs 5~12, exhaust was rapidly diluted and then transferred through a 16 m transfer line. The bulk effective densities for the medium load experiments were independent of the dilution ratio (Figure 6.6; Runs 6, 7, 8, 11, and 12). A similar trend was observed by Lipsky et al. (2006); for medium engine loads, elemental carbon (EC) dominated the carbon fraction, and hence, the impact of evaporation of semivolatile organics due to dilution on the particle mass was minor. Unlike Run 1 (Figure 6.2) and Run 2~4, where exhaust was introduced through a shorter transfer line (~2m), the particle volume concentrations increased in the dark due to coagulation regardless of engine load. An example of particle volume evolution in the dark is shown in Figure 6.7. Since the particle mass concentration was confirmed to be decreasing due to wall-loss (Figure 6.7), the increase of volume indicates particle coagulation leading to less dense particles. The volume increase is not likely due to condensation because the particles are highly fractal and condensing semi-volatiles would have filled the void fraction of the fractal particle rather than lead to an increase in mobility diameter. Furthermore, after turning on the blacklights, the particle volume did not respond to the SOA formation (Figure 6.5 (a)), whereas the SOA formation was confirmed by the slight increase of particle mass concentration (Figure 6.5 (b)). This is an obvious case where the particle volume

measurement by the SMPS fails to represent SOA formation, and hence, mass based measurement techniques are required. Since the mass evolution of Run 1 and 10 (Figure 6.7) in the dark is similar, only mass-based analysis for those long transfer line experiments would provide insightful understanding towards SOA formation.

The increasing trend of particle volume in the dark is attributed to the fractal nature of the particles. As shown through the experiments in Figure 6.5 where  the increasing volume in the dark was observed (Run 6~12), the particle bulk effective densities were lower than in the other cases (Run 1~4). Coagulation of fractal particles should lead to bigger, less dense particles. This is consistent with the concurrent observations of increasing particle volume concentration and decreasing mass concentration.  Jacobson et al. (2005) notes that coagulation rates of fractal-like particles are faster than that of spherical particles (Jacobson et al., 2005). However, the fact that the density dissimilarity in Run 1 and Run 10 was small but the dark volume evolution between the two cases was in the opposite direction (Figure 6.7) may suggest other unknown transfer line effects that enhance particle coagulation. The trend of continuously increasing volume along with decreasing bulk effective density in the dark was observed during all experiments using the long transfer line regardless of engine load (Run 5-12).

The fraction of POA calculated by equation 2 is compared for the experiments with different engine loads and injection methods (Figure 6.8). For all conditions, the POA fraction rapidly decreased due to SOA formation. The SOA fraction in Run 6 and 8 were smaller than the other runs, which was consistent with the lower density measurement

(Figure 6.5). While SOA formation was undetectable using the APM-SMPS for Runs 6 and 8, some SOA formation was detected in Run 7. This difference is attributed to experimental variability. The AMS mass spectrums from Run 6 and 8 (AMS not available for Run 7) were similar to the runs with higher SOA formation (major m/z including 30, 41, 43, 44, 55, and 57). Figure 6.8 indicates that approximately half of organic aerosol is composed of SOA during the first 2 to 5 hours of photooxidation increasing to approximately 80% within 12 hours.

Particle (and possibly semi-volatile) wall-loss correction was not performed in this study due to the uncertainties such as size-dependent wall-loss or coagulation of fractal particles. However, the POA/SOA split calculated by the AMS tracer method (equation 2) is independent of particle wall-loss (Figure 6.8). The apparent abundance of SOA (~80% within 12 hours) highlights the importance of diesel exhaust as a source of SOA in urban area. For the future, in addition to the series of measurement techniques employed in this study, an elemental carbon (EC) or black carbon (BC) measurement can help to constrain the carbon balance and particle wall loss (Chirico et al., 2010).

## 6.6 Conclusion

SOA was produced from dilute diesel exhaust following UV irradiation inside an environmental chamber. A unique set up of the APM-SMPS system enabled the determination of particle effective density as a function of particle mass, which in turn gave an improved insight into particle physical evolution during environmental chamber

studies of diesel exhaust. The fractal-like dimension of diesel particulates was observed to be ~ 2.2 – 3.0 by the APM-SMPS, indicating the particle shape could either be fractal or nearly spherical depending on experimental conditions. Particle volume concentration was demonstrated to underestimate SOA formation due to the filling of void spaces of agglomerate particles. The HR-ToF-AMS measurement indicated O/C ratio increased rapidly right after turning on the blacklights and continued to increase from 0.05 to 0.25 within 12 hours. The AMS also showed that SOA contributed to 80% of OA mass within 12 hours, emphasizing the importance of diesel exhaust as a source of urban SOA. When raw exhaust was injected into a nearly full chamber (in-chamber dilution), instead of injecting the diluted exhaust from an ejector diluter system into a nearly empty chamber (ejector-dilution), the particle effective densities were observed to be higher; this was attributed to faster evaporation of semi-volatile species by the intense mixing of an ejector diluter. For interpretation of SOA formation from diesel exhaust, it is critical to run a particle mass measurement since the volume measurement alone was found to be misleading in cases where particles are highly fractal.

## 6.7 References

Aiken, A. C., DeCarlo, P. F., Kroll, J. H., Worsnop, D. R., Huffman, J. A., Docherty, K., Ulbrich, I., Mohr, C., Kimmenl, J. R., Sun, Y., Zhang, Q., Trimborn, A. M., Northway, M., Ziemann, P. J., Canagaratna, M. R., Onasch, T. B., Alfarra, M. R., Prevot, A. S., Dommen, J., Duplissy, J., Metzger, A., Baltensperger, U., Jimenez, J. L.: O/C and OM/OC ratios of primary, secondary, and ambient organic aerosols with High-Resolution Time-of-Flight Aerosol Mass Spectrometry, Environmental Science & Technology, 42, 4487-4485, 2008

Atkinson, R.: Atmospheric chemistry of VOCs and NOx, Atmospheric Environment, 34, 2063-2101, 2000

Chan, A. W. H., Kautzman, K. E., Chhabra, P. S., Surratt, J. D., Chan, M. N., Crounse, J. D., Kurten, A., Wennberg, P. O., Flagan, R. C., Seinfeld, J. H.: Secondary organic aerosol formation from photooxidation of naphthalene and alkylnaphthalenes: implications for oxidation of intermediate volatility organic compounds (IVOCs), Atmospheric Chemistry and Physics, 9, 3049-3060, 2009

Chirico, R., DeCarlo, P. F., Heringa, M. F., Tritscher, T., Richter, R., Prévôt, A. S. H., Dommen, J., Weingartner, E., Wehrle, G., Gysel, M., Laborde, M., Baltensperger, U.: Impact of aftertreatment devices on primary emissions and secondary organic aerosol formation potential from in-use diesel vehicles: results from smog chamber experiments, Atmos. Chem. Phys., 10(23), 11545-11563, 2010

Cocker, D. R., Flagan, R. C., Seinfeld, J. H.: State-of the art chamber facility for studying atmospheric aerosol chemistry, Environmental Science & Technology, 35(12), 2594-2601, 2001

Davidson, C. I., Phalen, R. F., Solomon, S.: Airborne particulate matter and human health: A review, Aerosol Science and Technology, 39, 737-749, 2005

DeCarlo, P. F., Kimmel, J. R., Trimborn, A. M., Northway, M., Jayne, J. T., Aiken, A. C., Gonin, M., Fuhrer, K., Horvath, T., Docherty, K., Worsnop, D. R., Jimenez, J. L.: Field-deployable, high-resolution, Time-of-Flight Aerosol Mass Spectrometer, Anal. Chem., 78, 8281-8289, 2006

Donahue, N. M., Robinson, A. L., Pandis, S. N.: Atmospheric organic particulate matter: From smoke to secondary organic aerosol, Atmospheric Environment, 43, 94-106, 2009

Ehara, K., Hagwood, C., Coakley, K. J.: Novel method to classify aerosol particles according to their mass-to-charge ratio-Aerosol particle mass analyzer, Journal of Aerosol Science, 27(2), 217-234, 1996

Eldering, A., Cass, G. R.: Source-oriented model for air pollutant effects on visibility, Journal of Geophysical Research, 101(D14), 19343-19369, 1996

Grieshop, A. P., Miracolo, M. A., Donahue, N. M., Robinson, A. L.: Constraining the volatility distribution and gas-particle partitioning of combustion aerosols using isothermal dilution and thermodenuder measurements, Environmental Science & Technology, 43(13), 4750-4756, 2009

IPCC (2007). Intergovernmental Panel on Climate Change: Climate Change 2007: The Physical Science
Basis, Cambridge University Press, UK.

Jacobson, M. Z., Kittelson, D. B., Watts, W. F.: Enhanced coagulation due to evaporation and its effect on nanoparticle evolution, Environmental Science & Technology, 39, 9486-9492, 2005

Jayne, J. T., Leard, D. C., Zhang, X., Davidovits, P., Smith, K. A., Kolb, C. E., Worsnop, D. R.: Development of an Aerosol Mass Spectrometer for size and composition analysis of sibmicron particles, Aerosol Science and Technology, 33, 49-70, 2000

Kanakidou, M., Seinfeld, J. H., Pandis, S. N., Barnes, I., Dentener, F. J., Facchini, M. C., Van Dingenen, R., Ervens, B., Nenes, A., Nielsen, C. J., Swietlicki, E., Putaud, J. P., Balkanski, Y., Wilson, J.: Organic aerosol and global climate modelling: a review, Atmospheric Chemistry and Physics, 5, 1053-1123, 2005

Khalek, I. A., Kittelson, D. B., Brear, F.: Nanoparticle growth during dilution and cooling of diesel exhaust: Experimental investigation and theoretical assessment, SAE Tech. Pap. Ser., 2000-2001-0515 2000

Khalizov, A. F., Zhang, R., Zhang, D., Xue, H., Pagels, J., McMurry, P. H.: Formation of highly hygroscopic soot aerosols upon internal mixing with sulfuric acid vapor, Journal of Geophysical Research, 114, D05208, doi: 10.1029/2008JD010595, 2009

Kroll, J. H., Donahue, N. M., Jimenez, J. L., Kessler, S. H., Canagaratna, M., Wilson, K. R., Altieri, K. E., Mazzoleni, C., Wozniak, A. S., Bluhm, H., Mysak, E. R., Smith, J. D., Kolb, C. E., Worsnop, D. R.: Carbon oxidation state as a metric for describing the chemistry of atmospheric organic aerosol, Nature Chemistry, 3, 133-139, 2011

Kroll, J. H., Smith, D. F., Che, D. L., Kessler, S. H., Worsnop, D. R., Wilson, K. R.: Measurement of fragmentation and functionalization pathways in  the heterogeneous oxidation of oxidized organic aerosol, Phys. Chem. Chem. Phys., 11, 8005-8014, 2009

Lipsky, E. M., Robinson, A. L.: Design and evaluation of a portable dilution sampling system for measuring fine particle emissions from combustion systems, Aerosol Science and Technology, 39, 542-553, 2005

Lipsky, E. M., Robinson, A. L.: Effects of dilution on fine particle mass and partitioning of semivolatile organics in diesel exhaust and wood smoke, Environmental Science & Technology, 40(1), 155-162, 2006

Malloy, Q., Nakao, S., Qi, L., Austin, R. L., Stothers, C., Hagino, H., Cocker, D. R.: Real-time aerosol density determination utilizing a modified Scanning Mobility Particle Sizer - Aerosol Particle Mass Analyzer system, Aerosol Science and Technology, 43, 673-678, 2009

Matti Maricq, M., Podsiadlik, D. H., Chase, R. E.: Size distributions of motor vehicle exhaust PM: A comparison between ELPI and SMPS measurements, Aerosol Science and Technology, 33, 239-260, 2000

McMurry, P. H., Wang, X. W., Park, K., Ehara, K.: The relationship between mass and mobility for atmospheric particles: A new technique for measuring particle density, Aerosol Science and Technology, 36, 227-238, 2002

Park, K., Kittelson, D. B., McMurry, P. H.: Relationship between particle mass and mobility for diesel exhaust particles, Environmental Science & Technology, 37(3), 577-583, 2003

Pope, C. A., Dockery, D. W.: Health effects of fine particulate air pollution: Lines that connect, J. Air & Waste Manage. Assoc., 56, 709-742, 2006

Presto, A. A., Miracolo, M. A., Kroll, J. H., Worsnop, D. R., Robinson, A. L., Donahue, N. M.: Intermediate-volatility organic compounds: A potential source of ambient oxidized organic aerosol, Environmental Science & Technology, 43, 4744-4749, 2009

Robinson, A. L., Donahue, N. M., Shrivastava, M. K., Weitkamp, E. A., Sage, A. M., Grishop, A. P., Lane, T. E., Pierce, J. R., Pandis, S. N.: Rethinking organic aerosols: Semivolatile emissions and photochemical aging, Science, 315, 1259-1262, 2007

Sage, A. M., Weitkamp, E. A., Robinson, A. L., Donahue, N. M.: Evolving mass spectra of the oxidized component of organic aerosol: results from aerosol mass spectrometer analyses of aged diesel emissions, Atmospheric Chemistry and Physics, 8, 1139-1152, 2008

Samy, S., Zielinska, B.: Secondary organic aerosol production from modern diesel engine emission, Atmospheric Chemistry and Physics, 10, 609-625, 2010

Schauer, J. J., Rogge, W. F., Hildemann, L. M., Mazurek, M. A., Cass, G. R.: Source apportionment of airbourne particulate matter using organic compounds as tracers, Atmospheric Environment, 30(22), 3837-3855, 1996

Shrivastava, M. K., Lipsky, E. M., Stanier, C. O., Robinson, A. L.: Modeling semivolatile organic aerosol mass emissions from combustion systems, Environmental Science & Technology, 40(8), 2671-2677, 2006

Volkamer, R., Jimenez, J. L., Martini, F. S., Dzepina, K., Zhang, Q., Salcedo, D., Molina, L. T., Worsnop, D. R., Molina, M. J.: Secondary organic aerosol formation from anthropogenic air pollution: Rapid and higher than expected, Geophysical Research Letters, 33(L17811), doi: 10.1029/2006GL026899, 2006

Weitkamp, E. A., Sage, A. M., Pierce, J. R., Donahue, N. M., Robinson, A. L.: Organic aerosol formation from photochemical oxidation of diesel exhaust in a smog chamber, Environmental Science & Technology, 41(20), 6969-6975, 2007

Xue, H., Khalizov, A. F., Wang, L., Zheng, J., Zhang, R.: Effects of coating of dicarboxylic acids on the mass-mobility relationship of soot particles, Environmental Science & Technology, 43, 2787-2792, 2009

**6.8    Table**

Table 6.1 Engine load, initial concentrations, calculated OH concentration, Df, bulk effective density, and overall dilution ratio.

| Run | load | PM volume ($\mu m^3/cm^3$)[a] | PM number ($10^4\,cm^{-3}$)[a] | initial $NO_x$ (ppm)[a] | initial ethene (ppb)[a] | calculated OH (molec/cm³)[b] | $D_f$ (Ave.±S.D.)[c] | bulk $\rho_{eff}$ (g/cm³)[d] | dilution ratio |
|---|---|---|---|---|---|---|---|---|---|
| Ejector-dilution, short transfer line | | | | | | | | | |
| 1  4/17/2010 | idle | 68 | 3.9 | 0.76 | N.A. | N.A. | 2.52 → 2.81 | 0.70 | 114 |
| In-chamber dilution, short transfer line | | | | | | | | | |
| 2  3/20/2010 | idle | 195 | 9.3 | 1.60 | 150 | $1.4 \times 10^6$ | 2.97 ± 0.05 | 1.16 | 54 |
| 3  4/23/2010 | idle | 22 | 2.5 | 0.24 | 32 | $1.6 \times 10^6$ | 2.65 → 2.83 | 0.84 | 362 |
| 4  5/7/2010 | idle | 50 | 3.7 | 0.54 | 71 | $1.6 \times 10^6$ | 2.79 → 2.90 | 0.99 | 161 |
| Ejector-dilution, long transfer line | | | | | | | | | |
| 5  5/16/2009 | medium | 94 | 2.4 | 0.57 | N.A. | N.A. | N.A. | N.A. | 409 |
| 6  11/13/2009 | medium | 103 | 5.3 | 0.65 | N.A. | N.A. | 2.39 ± 0.03 | 0.49 | 359 |
| 7  11/16/2009 | medium | 36 | 3.1 | 0.23 | N.A. | N.A. | 2.39 ± 0.03 | 0.49 | 1015 |
| 8  11/18/2009 | medium | 53 | 3.7 | 0.30 | N.A. | N.A. | 2.35 ± 0.05 | 0.55 | 778 |
| 9  2/1/2010 | low | 113 | 4.5 | 0.91 | 45 | $1.1 \times 10^6$ | 2.44 ± 0.04 | 0.51 | 176 |
| Ejector-dilution, long transfer line, dark | | | | | | | | | |
| 10  2/25/2010 | idle | 94[e] | 5.2[e] | 0.30[d] | 76 | N.A. | 2.55 → 2.45 | 0.67 | 290 |
| 11  5/9/2009 | medium | 124[e] | 4.9[e] | 0.92[d] | N.A. | N.A. | 2.38 ± 0.03 | 0.55 | 254 |
| 12  7/6/2010 | medium | 74[e] | 5.0[e] | 0.45[d] | N.A. | N.A. | 2.40 → 2.20 | 0.62 | 519 |

Note:
a   values when blacklights were turned on
b   calculated based on ethene decay
c   calculated by power curve fit on effective density v.s. mobility diameter (see text)
d   values when injection finished
e   values 2 hours after injection (typical time left in dark for aging experiments)

N.A.: not acquired

## 6.9 Figures
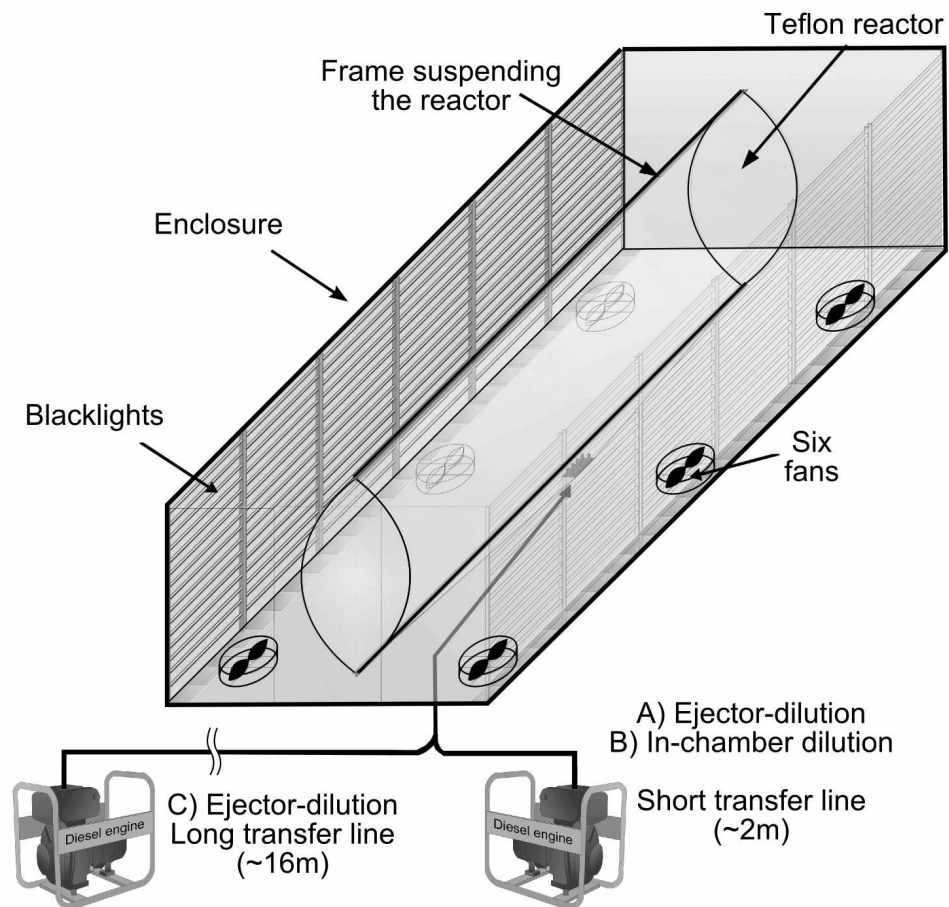


Figure 6.1 A schematic diagram of the CE-CERT/ UC Riverside mezzanine chamber.
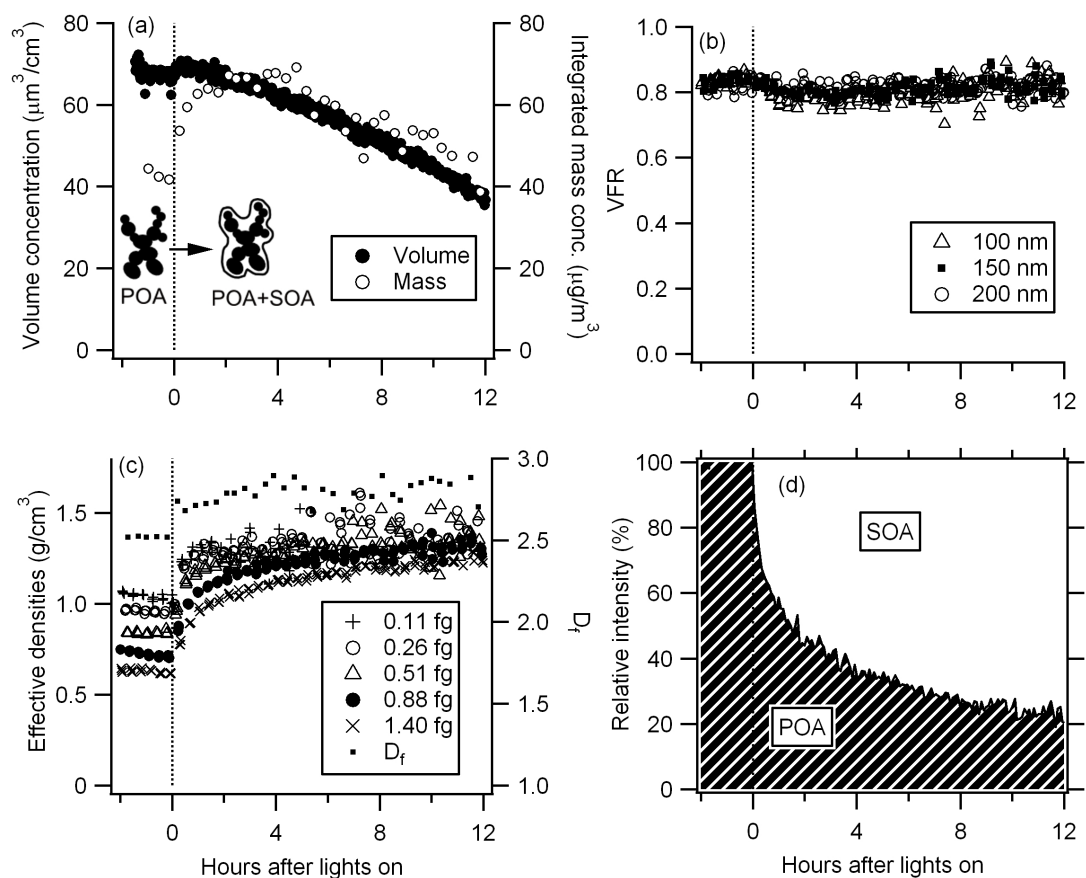
Figure 6.2 Time series of (a) particle volume concentration and mass concentration, (b) volume fraction remaining (100°C), (c) effective density, fractal-like dimension ($D_f$), and (d) OA fraction. See text for detail (Results of Run 1).
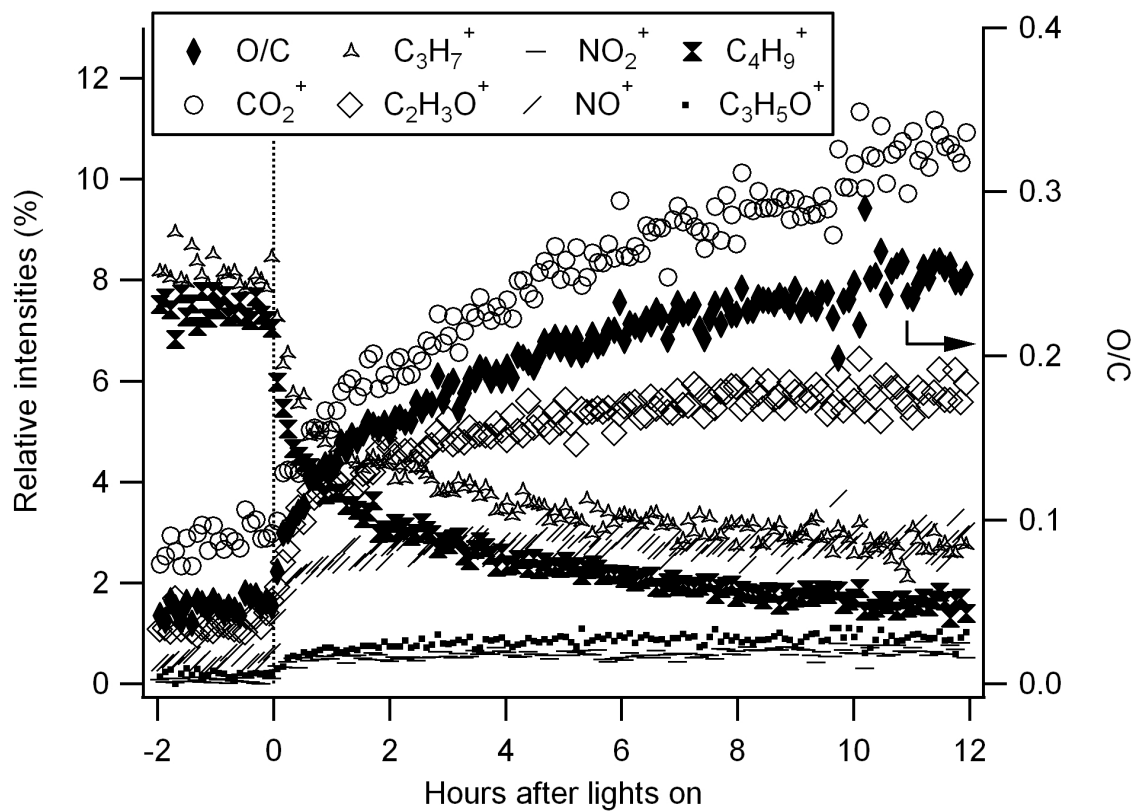
Figure 6.3 Time series of select ions measured by an AMS (Run 1).
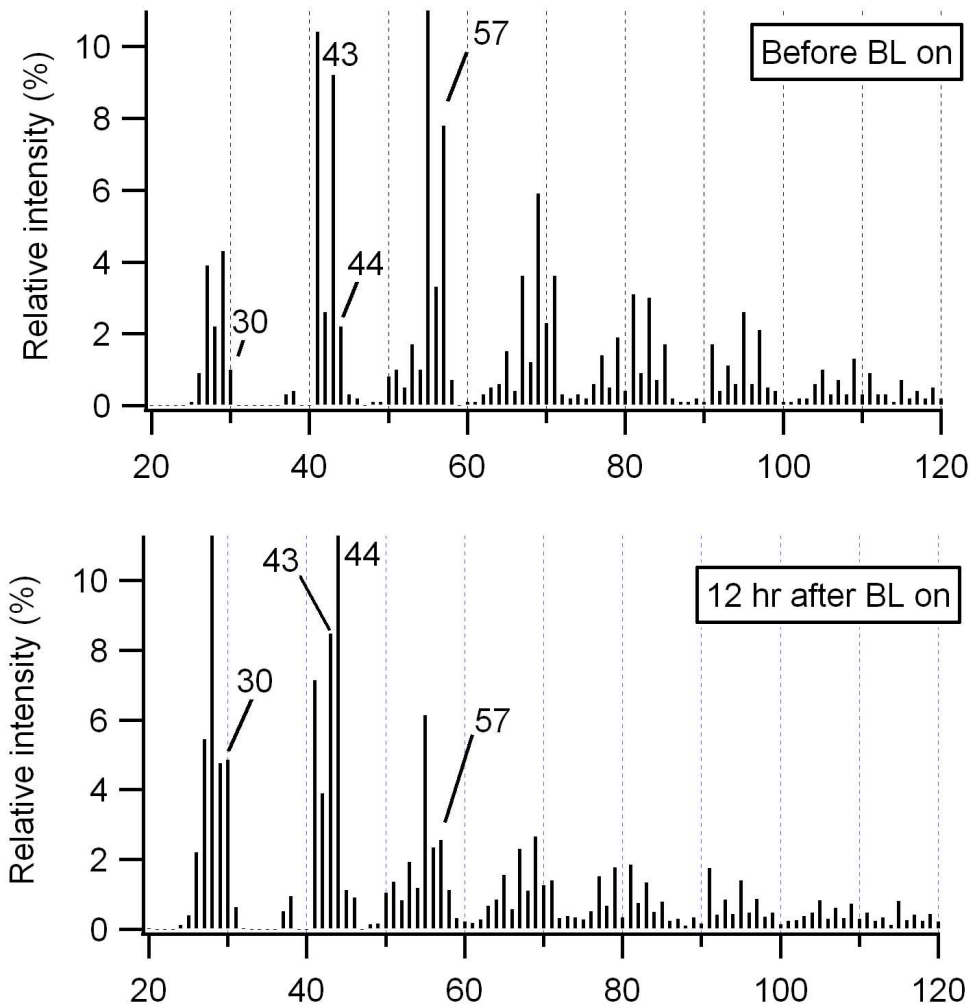
Figure 6.4 Aerosol mass spectrums of diesel exhaust particulate before and after UV irradiation (Run 1).
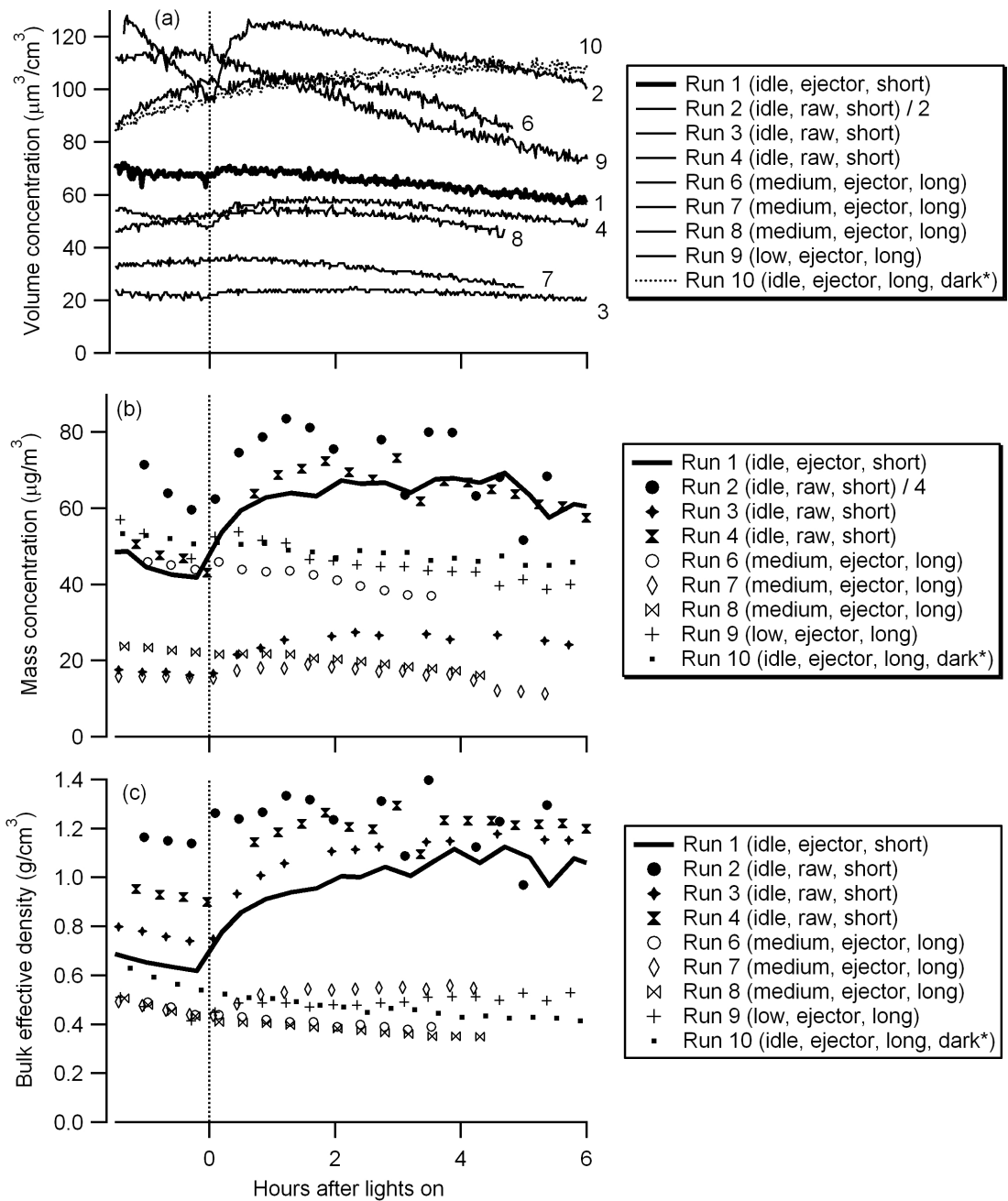
Figure 6.5 Evolution of particle volume, mass concentration, and bulk effective density (*Lights were not turned on for the Run 10, but shown for the sake of comparison. Time injection completed is set to -2hr).
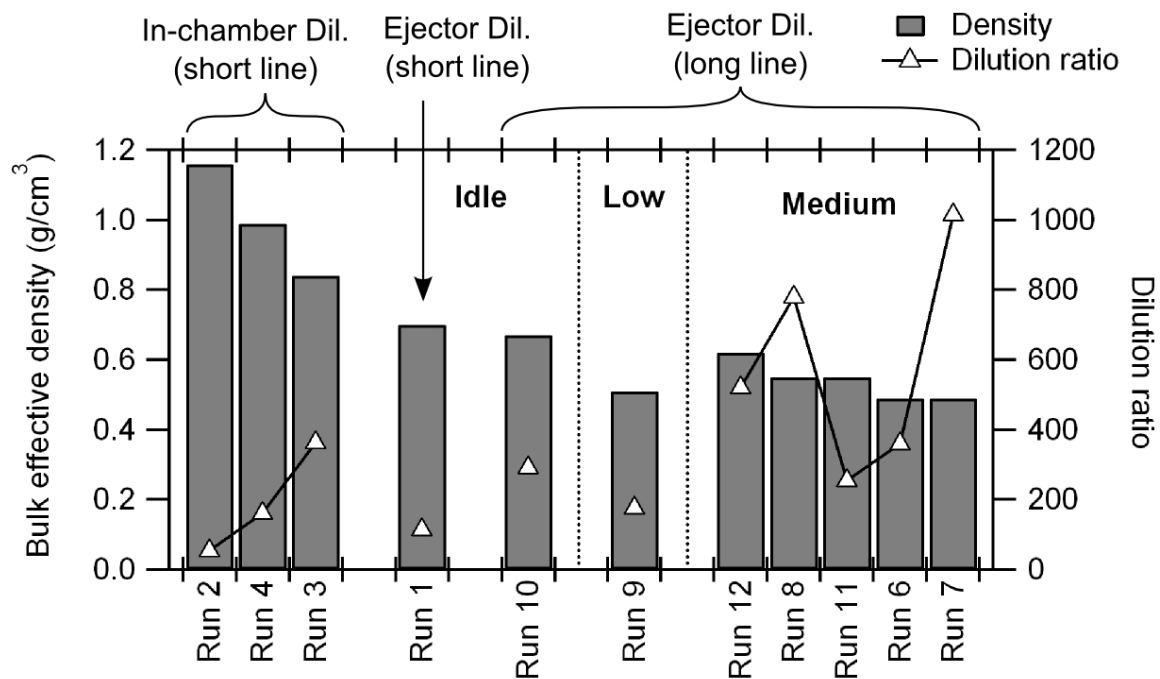
Figure 6.6 Effective densities of particles in an environmental chamber and dilution ratio when the injection was completed.
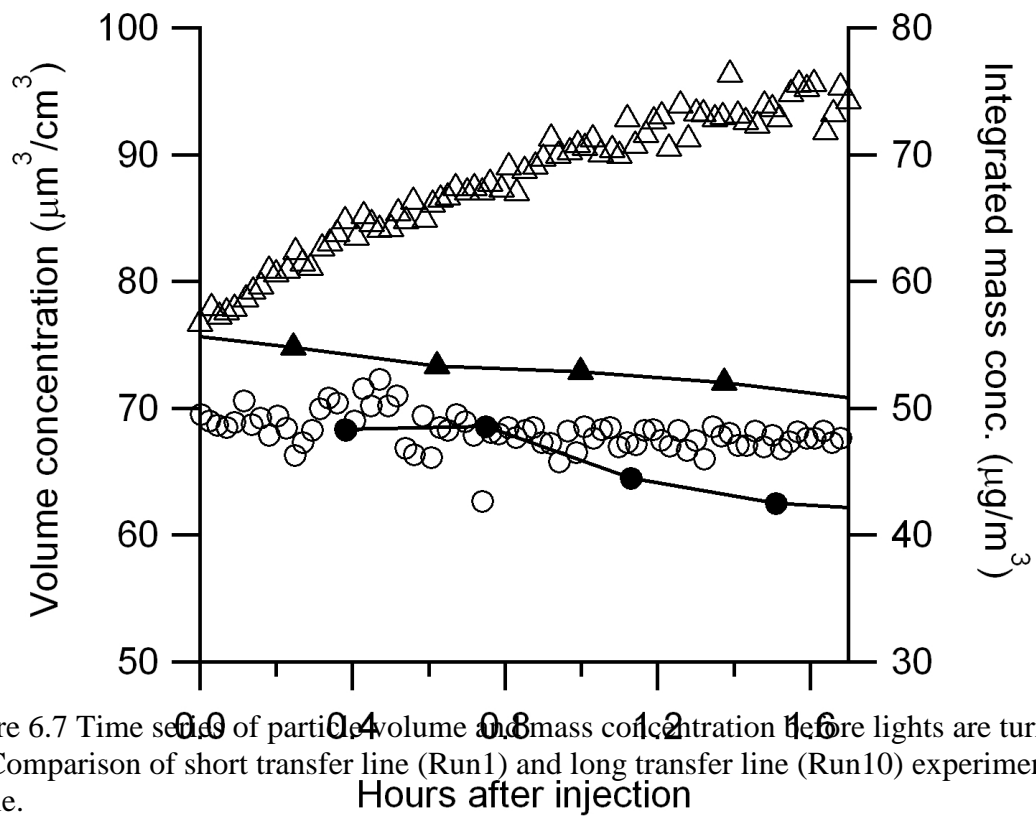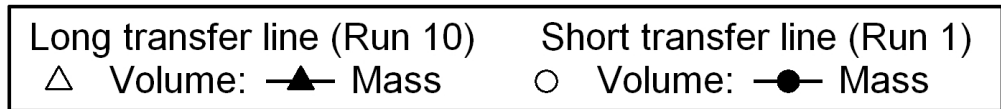
Figure 6.7 Time series of particle volume and mass concentration before lights are turned on. Comparison of short transfer line (Run1) and long transfer line (Run10) experiments at idle.
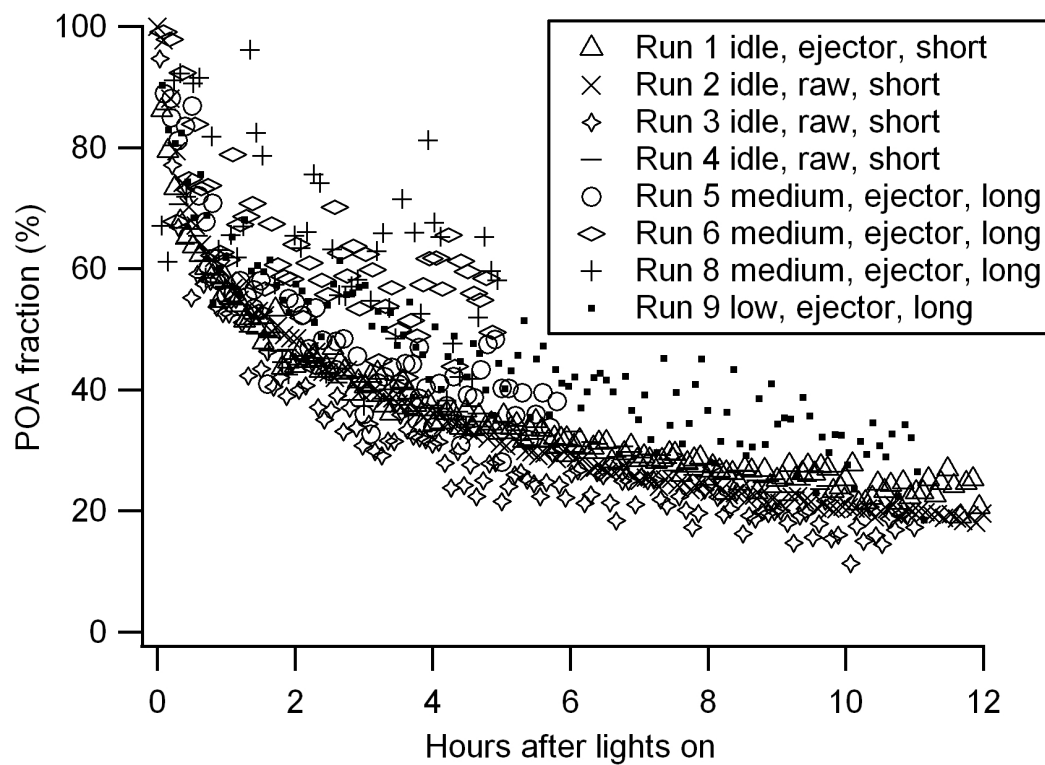
Figure 6.8 Evolution of POA fraction calculated by the AMS $C_4H_9^+$ tracer method (equation 2, see text).

# 7 Particles Formation from Photooxidation of Methyl Iodide (CH$_3$I): Mass-based Analysis of Fractal-like Particles

## 7.1 Introduction

The atmospheric chemistry of iodine (I) received much attention due to its importance in biogeochemical cycle and oxidizing capacity of the atmosphere. Reactions of iodine species influences oxidizing capacity of the atmosphere by catalytically destroying tropospheric ozone, thereby impacting HO$_x$ and NO$_x$ balance in the troposphere (Saiz-Lopez et al., 2011). Iodine species have been reported to contribute to new particle formation, which influences cloud formation and global climate (Jimenez et al., 2003; O'Dowd and de Leeuw, 2007; O'Dowd et al., 2002; Saiz-Lopez et al., 2011).

The global source of iodine species is dominated by marine emissions. In coastal areas, macro algae (seaweed) exposed to the atmosphere at low tide release a number of iodine species resulting in new particle formation (O'Dowd et al., 2002). Although CH$_2$I$_2$ was considered to be a promising source of new particles formed in coastal areas (Jimenez et al., 2003; O'Dowd et al., 2002), recent studies suggest that the contribution from iodine molecule (I$_2$) dominate the iodine source in coastal areas where seaweed is abundant (Saiz-Lopez and Plane, 2004; Saiz-Lopez et al., 2011). Importance of I$_2$ in open ocean, however, is uncertain. iodocarbons (e.g., CH$_3$I, CH$_2$I$_2$) released from microalgae (phytoplankton, cyanobacteria) may dominate over I$_2$ in open ocean (Saiz-Lopez et al., 2011).

Previous studies observed rapid new particle formation by photolysis and subsequent reactions of iodine radical with $O_3$ (Jimenez et al., 2003). Secondary particles formed by the photooxidation of iodine-containing species are referred to as iodine oxide particles (IOP). Previous studies proposed that IOP is formed from a number of iodine oxide species, such as OIO, $I_2O_3$, $I_2O_4$, and $I_2O_5$ as well as iodine oxyacids ($HIO_4$) (Jimenez et al., 2003). However, the chemical composition of IOP remains uncertain. Although a number of IOP precursors such as $I_2$ and $CH_3I$ exist, particle formation mechanisms except initial photolysis to release iodine radical (I) are expected to be similar between those IOP precursors.

Since the vapor pressures of iodine oxides are expected to be low, iodine oxides are likely to contribute to both new particle formation and growth of particles (O'Dowd and de Leeuw, 2007). Experimental investigation of growth of IOP could be challenging due to its fractal-like structure (Jimenez et al., 2003). Since the commonly used particle measurement techniques in the previous studies are based on particles (mobility) diameter, mass based particle formation yield (ratio of mass of IOP formed to mass of parent iodine containing species reacted) cannot be directly determined without measurements of particle density.

The aim of this study is to investigate IOP formation physically (mass-based yield) and chemically (HR-ToF-AMS) under varied conditions including $O_3$ and $NO_x$ levels to

150

better understand IOP formation mechanisms. Additionally, this study also developed a model to evaluate IOP formation mechanisms by comparing modeled and measured particle mass.

## 7.2 Experimental

### 7.2.1 Environmental chamber

The experiments were conducted in the UC Riverside/CE-CERT environmental chamber described in detail in Carter et al. (2005). Briefly, the chamber facility consists of dual 90 $m^3$ Teflon® reactors suspended by rigid frames in a enclosure ($27 \pm 1$ °C) continuously flushed with dry (a dew point below -40 °C) purified air generated by an Aadco 737 series (Cleves, Ohio) air purification system. Black lights (115 W Sylvania 350BL, $NO_2$ photolysis rate 0.13 $min^{-1}$) are used as the light source for all the experiments reported herein.

### 7.2.2 Gas and particle analysis

The Agilent 6890 Gas Chromatograph – Flame Ionization Detector was used to measure concentrations of $CH_3I$. Calibration was performed by injecting known amount of $CH_3I$ into the 90 $m^3$ chamber. $NO_x$, $O_3$, and CO are monitored by $NO$-$NO_y$ analyzer (Teco Model 42C), Ozone analyzer (Dasibi Model 1003-AH), and CO analyzer (Thermo Environmental Instruments Inc. Model 48C), respectively.

Particle size distribution between 28 nm and 712 nm was monitored by a custom built

Scanning Mobility Particle Sizer (SMPS) similar to that described by Cocker et al. (2001).

Particle volume in terms of mobility diameter is reported as a conventional way in

environmental chamber studies; due to the fractal-like structure of IOP, however, particle

effective density (particle mass / particle volume based on mobility diameter) is

necessary to obtain particle mass concentration. Particle effective density was measured

with an Aerosol Particle Mass Analyzer (APM, Kanomax) (Ehara et al., 1996) and SMPS

in series; herein referred as APM-SMPS system (Malloy et al., 2009; Nakao et al., 2011;

Nakao et al., 2012). The APM is located upstream of the SMPS for improved time

resolution and sensitivity over the more common configuration of Differential Mobility

Analyzer (DMA) – APM configuration (Khalizov et al., 2009; McMurry et al., 2002; Xue

et al., 2009). The effective density of fractal-like particles depends on size (mass) of

particles (Nakao et al., 2011; Xue et al., 2009); therefore, particle mass concentration is

calculated by integrating size dependent effective density and PM volume-size

distribution (Nakao et al., 2011).

Particle volatility was investigated with a volatility tandem differential mobility analyzer

(VTDMA) (Nakao et al., 2011; Qi et al., 2010; Rader and McMurry, 1986), in which

monodisperse particles of mobility diameter $D_{mi}$ are selected by the 1$^{st}$ DMA followed by

transport through a Dekati$^{®}$ thermodenuder (TD, residence time: approximately 17

seconds, at varied temperature). The particle size after the TD ($D_{mf}$) is then measured by

fitting a log-normal size distribution curve from the 2$^{nd}$ SMPS. Mobility diameter ratio is

then calculated as $D_{mf}/D_{mi}$. Note that the mobility diameter of fractal-like particle is not sensitive to evaporation (related to mass). Significant reduction of diameter can be observed when majority of particle evaporate or when particle shape changes.

Particle chemical composition and its evolution was observed by a high resolution time-of-flight aerosol mass spectrometer (HR-ToF-AMS) (DeCarlo et al., 2006; Jayne et al., 2000). The HR-ToF-AMS operated in the high sensitivity V mode. Chemical formula of IOP fragment ions (e.g., $IO^+$) was confirmed by a high-resolution analysis template (PIKA).

### 7.2.3 Chamber experiments

A known volume of high purity liquid $CH_3I$ was injected through a heated glass injection manifold system and flushed into the chamber with pure $N_2$. NO was injected into a chamber by flushing $N_2$ through a calibrated glass bulb filled with known pressure of pure NO (UHP grade, Matheson) and $N_2$; $NO_2$ was produced via a reaction between NO and $O_2$ (in pure air) inside a glass bulb and injected by the same way as NO. For the experiments with excess $O_3$, $O_3$ was produced by two $O_3$ generators (OZG-UV-01, HORIBA) supplied with 20 psi pure air. Pure CO (99.5%, Praxair) was introduced into the chamber through an activated charcoal trap (to remove impurity). Particle wall-loss correction was performed by using exponential decay rates of particle numbers (Carter et al., 2005).

## 7.3    Results and Discussions

The experimental test matrix is summarized in Table 1. Results from four different types of experiments are shown: 1) experiments with only $CH_3I$ (without $O_3$) to confirm particle formation does not occur from only $CH_3I$ photolysis, 2) experiments with $CH_3I$ and $NO_x$ where $O_3$ is slowly formed by photochemical reactions, 3) experiments with $CH_3I$, $NO_x$, and CO where CO enhances $O_3$ formation by converting OH to $HO_2$, and 4) experiments with $O_3$ added initially (excess $O_3$).

### 7.3.1    IOP formation

### 7.3.1.1    IOP size and volume analysis

Jimenez et al. (2003) observed no particle formation when $CH_2I_2$ is photolyzed without $O_3$; similarly, no particle formation was observed for the photolysis of $CH_3I$ without $O_3$ (Table 1: Run 1453B). Significant IOP formation was observed for the experiments with sufficiently high $O_3$. Example time traces of experiments with $O_3$ initially present (Run 1453A) or generated from reactions within an environmental chamber (Run 743B) is shown in Fig. 1. Particles were formed immediately following blacklight irradiation when there is $O_3$ initially present; on the other hand, particle formation was delayed for the experiments with $O_3$ generated by reactions within the chamber (Fig.1c), consistent with the critical role of $O_3$ in IOP formation. Size (geometric mean diameter) evolution suggests particles grew at similar rates in these two examples after nucleation.

### 7.3.1.2 Chemical analysis of IOP

An AMS spectrum of IOP formed with the presence of $NO_x$ is shown in Fig. 2. Mass spectra of IOP formed without $NO_x$ are similar and not shown. The abundant iodine containing species are consistent with Jimenez et al. (2003) with additional observations of $I_2O_2^+$ and $I_2O_4^+$ ($IO_5^+$ was not observed). In addition, only minor changes in particle composition are observed by taking ratios of major AMS signals to the most abundant $I^+$ signal (Fig.3). Since $NO^+$ (m/z 30) and $NO_2^+$ (m/z 46) fragments are minor ($[NO^+ + NO_2^+]/I^+ \sim 5\%$, from high-resolution analysis), contribution from nitrogen species such as $INO_2$ and $IONO_2$ to IOP is expected to be minor. Although $CO_2^+$ was reported to be minor by Jimenez et al. (2003), $CO_2^+$ was consistently observed to be the 2$^{nd}$ most abundant ion in this study (Fig.2, Fig.3). $CO_2^+$ fragment is a commonly observed fragment originating from thermal decomposition of carboxylic acids on the AMS vaporizer at 600°C (Aiken et al., 2008); the source of $CO_2^+$ fragment in this study is unknown. Contribution from background particles to $CO_2^+$ is unlikely since no particles are formed in experiments without $O_3$ (Run 1453B).

Significant hydrogen-containing fragments ($HI^+$, $HOI^+$, $HIO_2^+$, $HIO_3^+$) are observed as reported by Jimenez et al. (2003); however, formation mechanisms of the hydrogen-containing species is uncertain under the dry conditions used in this study and their study. Although $IO_3^-$ can be formed by aqueous reactions (McFiggans et al., 2000), contribution from aqueous reactions are unlikely since experiments were carried out under dry

conditions. Jimenez et al. (2003) proposed $HIO_3$ may be formed by unknown gas-phase reactions and/or reactions of particle-bound water and iodine oxides on the AMS vaporizer.

### 7.3.1.3    IOP mass analysis

Particle effective density was measured by an APM-SMPS. Since effective densities of fractal-like particles depend on particle size (Nakao et al., 2011; Xue et al., 2009), the APM setting (voltage and RPM) was alternated to select different particle masses so that density can be acquired as a function of particle mass (and size from the SMPS downstream) (Nakao et al., 2011). A time-series of effective densities for different particle masses (in femtogram) is shown in Fig.4. Size-dependent densities are typically observed for fractal-like particles; the effective densities of smaller agglomerate particles tend to be higher due to smaller fraction of void space within particles. The relationship between effective density and particle size is fitted into a power function; fractal-like dimension ($D_f$) is calculated as follows (Nakao et al., 2011; Park et al., 2003; Xue et al., 2009):

$$\rho_{eff} = C \cdot d_m{}^{D_f - 3} \tag{Eq.1}$$

where $\rho_{eff}$ is the particle effective density and $d_m$ is the mobility diameter (determined by the SMPS downstream of the APM). $D_f$ was calculated to be nearly constant within 2.1~2.2 for two excess $O_3$ experiments (Run 1452A and 1453A) (Fig.4). The power function fit is utilized to interpolate/extrapolate density-size relationship within SMPS size range (28-712nm) and particle mass concentration is calculated by integrating size-

dependent effective density and particle volume distribution over the SMPS can range (Fig.5) (Nakao et al., 2011); particle bulk effective density was calculated by dividing the integrated particle mass concentration by volume concentration (measured by the SMPS) and shown in Fig.4. Jimenez et al. (2003) reported that $D_f$ and effective density decreased over time which was likely to be due to particle growth by coagulation resulting in higher void fraction. Density evolution in this study was opposite (Fig.4); particle effective density increased, although $D_f$ was relatively constant. Since changes in chemical composition was minor (Fig.3), it would be reasonable to assume that the change in effective density is due to physical change in particle structure. The difference between density evolution of Jimenez et al. (2003) ($CH_2I_2$, decreasing trend) and this study ($CH_3I$, increasing trend) may be explained by different kinetics. $CH_2I_2$ can photolyze in a few minutes and then the supply of IOP precursor stops; once initial particle formation is ceased, particles coagulate and density decrease. On the other hand, the reaction of $CH_3I$ is much slower (Fig.1a) and IOP precursors are continuously supplied to the reaction system; iodine-containing vapors are likely to keep condensing onto particles after nucleation, while particles are still fractal-like enough not to fill up void space of particles (keeping $D_f$ nearly constant).

The effective density evolution can be used to calculate mass concentration of fractal-like particles. Since density measurements are only available for excess ozone experiments, density evolution for other type of runs are estimated based on delay in particle size evolution (Fig.1d). Compared to excess $O_3$ experiments, particle formation in $O_3$

formation experiment (with CO) was delayed by approximately 100 min; additional 100 min for experiments without CO. Particle mass-based yield (PM mass concentration / $CH_3I$ mass reacted) is shown in Fig.6. The yield ranged between 0 ~ 1.22. Effects of experimental conditions especially $NO_x$ conditions are discussed in the following sections.

### 7.3.1.4    NO and $NO_2$ effects on IOP formation

Until recently, iodine chemistry has been assumed to be suppressed by $NO_x$ and thus limited to occur in remote/clean regions; however, recent field studies suggested the reactive iodine is persistent under semi-polluted conditions (NO: <1 ppb, $NO_2$: ~2 ppb) (Mahajan et al., 2009; McFiggans et al., 2010). However, more recently, Mahajan et al. (2011) observed lack of new particle formation on the day with the highest level of I and $I_2$ over their field campaign but also with higher $NO_2$ (8 ppb), which suggest at higher level of $NO_x$ (or $NO_2$), particle formation may be suppressed. In this study, experiments were carried under varied $NO_x$ conditions (without $NO_x$ or with ~25 ppb $NO_x$) and its effect on $O_3$ and IOP formation was investigated (Table 1). Summary of experimental results are shown in Fig. 7 along with modeling results that are discussed in the following section.

The time of the onset of particle formation varied widely depending on the experimental conditions (Fig.7). The onset was observed to be largely dependent on NO concentration rather than $O_3$ concentration, since $O_3$ concentration at the onset of particle growth varied widely (10~40ppb, except for excess $O_3$ experiments) but NO concentration was in a

narrow range (2~6ppb). On the other hand, when all $NO_x$ is initially present as $NO_2$ (24ppb) in the Run 1452A ($CH_3I + NO_x + O_3$), particle formation started immediately after irradiation. Under the high $O_3$ and $NO_2$ condition, especially $IONO_2$ formation is expected to be enhanced, as well as $INO_2$ formation and reactions with $NO_3$ radicals. The immediate particle formation in Run 1452A suggests that $IONO_2$ reservoir is short-lived, in agreement with Mahajan et al. (2009).

Once NO becomes sufficiently low (a few ppb), IOP is formed and particle yields are nearly one (approximately 0.7~1.2), regardless of the presence of $NO_2$ (Fig.6). Therefore, the results suggest NO delays particle formation (without significantly changing final particle formation yield) and $NO_2$ possibly produce short-lived reservoir species without reducing particle formation at least in the laboratory conditions, which is consistent with the observation of only minor $NO^+$ and $NO_2^+$ fragment in AMS spectra (Fig.2, 3).

### 7.3.1.5 Volatility analysis of IOP

Changes in IOP diameter after passing through a thermodenuder is shown in Fig.8. No significant change in particle size was observed at 100~150°C; particles started to shrink at temperature above 150°C. Since diameter measurement of fractal-like particle is not sensitive to mass, it is likely that majority of particle mass has evaporated at 200~225°C (Fig.8). Since vaporizer temperature used in the AMS is ~600°C, IOP is expected to fully vaporize (Jimenez et al., 2003).

### 7.3.2 Model description

In order to test our interpretations of the experimental results described above, a model was developed based on previous studies (Furneaux et al., 2010; Jimenez et al., 2003; McFiggans et al., 2000; Pirjola et al., 2005; Saiz-Lopez et al., 2008) with some modifications. This model has three components: 1) base gas-phase mechanisms from SAPRC-07 (Carter, 2007); 2) additional iodine reactions that are not included in SAPRC-07(see Table 2), and 3) reactions for gas-to-particle conversion.

### 7.3.2.1 Gas-phase reactions

Gas-phase reactions used in the model are summarized in Table 2 and Figure 9. Reactions expected to be minor are shown by thin lines and small text in Fig. 9. For details of gas-phase reactions relevant to IOP formation, refer to a recent review by Saiz-Lopez et al. (2011).

In terms of ozone formation and loss, the reaction of I and $O_3$ (Reaction I-03) is the major $O_3$ loss process. If subsequent reactions regenerate I without conversion of NO to $NO_2$ or OH to $HO_2$, the net effect is the destruction of $O_3$. For instance, $OIO + h\nu \rightarrow I + O_2$ (Reaction I-34) leads to ozone destruction (by the reaction of I and $O_3$), but $OIO + NO \rightarrow IO + NO_2$ (Reaction I-33) regenerates $O_3$ by photolysis of $NO_2$ into NO and O and subsequent combination of O and $O_2$ (Saiz-Lopez et al., 2011).

In moderately polluted regions where anthropogenic $NO_x$ emissions contribute to maintaining a non-negligible $NO_x$ level, reactions involving NO and $NO_2$ and $NO_3$ (especially in the nighttime) play important roles in iodine chemistry. For instance, the reaction of $I_2$ and $NO_3$ (Reaction I-17) forms I and $IONO_2$, the photolysis of $IONO_2$ (Reaction I-44) regeneratesNO$_3$ and I, and these I atoms can destruct $O_3$ in semi-polluted environments (Saiz-Lopez et al., 2011). In addition, recent studies suggest that $IONO_2$ is short lived and its reaction with I (Reaction I-46) produces $I_2$ and makes iodine chemistry still active in semi-polluted environments (Kaltsoyannis and Plane, 2008; Mahajan et al., 2009).

### 7.3.2.2  Particle formation

Previous experimental and modeling studies investigated new particle formation from iodine chemistry (Jimenez et al., 2003; Pirjola et al., 2005). The model in this study focuses on mass-based analysis of condensational growth with a simplified representation of new particle formation. Briefly, particle formation is assumed to occur by bimolecular reactions of condensable species at a constant reaction rate for all the condensable species; the reaction rate is assumed to be 5.0 ppm$^{-1}$ min$^{-1}$ ($3.4 \times 10^{-15}$ molecule$^{-1}$ cm$^3$ s$^{-1}$) based on the best agreement of the predicted and measured onsets of particle growth for most of the experiments.

In the model, the conversions of gas-phase condensable species (e.g., $kOnI_2O_5$ for $I_2O_5$) to PM-phase condensable species are represented by treating such gas-to-particle

conversions as a reaction between condensable species and particle mass (PMmass), and

their rate constants are calculated as follows:

$$kOnI_2O_5 = (k[dif] \times k[kin]) / (k[dif] + k[kin]) \qquad (Eq.2)$$

where k[kin] is the free molecular kinetic limit and k[dif] is the continuum diffusion limit.

As discussed by Stroud et al. (2004), $k[kin] = 3\alpha_i c_i/(4\rho r)$ and $k[dif] = 3D_i/(\rho r^2)$ where $\alpha_i$

is the accommodation coefficient for species i, $c_i$ is the mean gas-phase molecular speed

of species i (given by sqrt $(8RT/\pi Mw_i)$ where R is the gas constant, T is the temperature

and $Mw_i$ is the molecular weight of species i (e.g., $MwI_2O_5$ for $I_2O_5$), $\rho$ is the density

(PMden), r is the particle radius (PMradius), and $D_i$ is the diffusion coefficient of species

i (estimated by using the molecular weight). In terms of the parameters defined above,

k[in] and k[dif] for $I_2O_5$ are calculated as follows:

$$k[kin] = 7.18 \times 10^{-4} \times \alpha(I_2O_5) \times sqrt(T) / (PMden \times PMradius \times sqrt(MwI_2O_5)) \qquad (Eq.3)$$
$$k[dif] = 1.8 \times 10^4 \times D(I_2O_5) / (PMden \times PMradius^2) \qquad (Eq.4)$$

where $7.18 \times 10^{-4}$ and $1.8 \times 10^4$ are conversion factors incorporating the gas constant R

and units of ppm for $I_2O_5$ and $\mu g/m^3$ for PMmass.

Condensable species and assumed accommodation coefficients are given in Table 2.

Although $INO_2$ and $IONO_2$ can be taken up by wet aerosols (McFiggans et al., 2000;

Saiz-Lopez et al., 2008), particle formation from $INO_2$ and $IONO_2$ are assumed to be

negligible in the dry conditions used in this study. The observation of only minor $NO^+$

and $NO_2^+$ fragments from IOP by the HR-ToF-AMS supports this assumption (Fig.2, 3).

Condensation was treated as a permanent irreversible loss (Furneaux et al., 2010). Since

experimental results of PMden are available only for experiments with excess $O_3$, PMden

evolution for experiments with $O_3$ generation (with CO) is assumed to be delayed by 100 min compared to excess $O_3$ experiment; experiments with $O_3$ generation without CO is assumed to be delayed by additional 100 min, based on the delay in particle diameter evolution for the three types of experiments (excess $O_3$, with CO, and without CO) (not shown).

PMradius at a given time in a given experiment is calculated from the ratio of the calculated PM volume to the calculated PM area (with a factor of 3) for each time of the experiment, using the mobility diameter measured by a SMPS. Jimenez et al. (2003) assumed that the influence of fractal nature on mass transfer of vapors to IOP is negligible since Rogak et al. (1991) reported that the mass transfer rates of 1.5 nm lead clusters (used as a surrogate for a gas-phase species) to spheres and agglomerates with the same mobility diameter were same. Therefore, this study uses surface area and volume to derive the average radius; the use of surface area and volume to calculate diameter for the condensation rate calculation is appropriate, since the mass transfer rate is proportional to surface area and is calculated using PMmass that is proportional to volume. Representative PMradius evolution is used for each type of experiments (excess $O_3$, $O_3$ formation with CO, and without CO).

Particle wall-loss rates were determined by calculating the first-order decay rate of particle number (Carter et al., 2005) and used as inputs for the model. Dilution rates are determined by calculating the first-order decay rate of an inert tracer, n-$C_6F_{14}$ (whenever

available), or CO (assuming CO is unreactive). Although CO reacts with OH (and acts as $O_3$ amplifier in the presence of $NO_x$), since the relative loss of CO through the reaction was small (e.g., estimated to be 0.3% loss in 6 hours by SAPRC-07 prediction for Run 734A), CO was used as a tracer to measure dilution factors.

### 7.3.3    Model vs. Experiment

Comparison of experimental results and model prediction is shown in Fig.7. Model A is based on reactions shown in Table 2; Model B uses arbitrarily enhanced $IONO_2$ thermal decomposition rate as discussed below. Experimental PM volume is acquired by SMPS (without wall-loss correction); model PM volume is calculated from predicted PM mass, particle density and wall-loss rate. Therefore, comparison of measured and modeled PM volume is equivalent to comparison of measured and modeled PM mass.

Model A predictions of $O_3$ and PM showed excellent to reasonable agreements with experimental results for experiments with excess $O_3$ (Run 1453A and 742A) except for Run 1452A with additional $NO_2$ (Fig. 7). When $NO_2$ and $O_3$ are both present at a relatively high level (Run 1452A), model A underpredicted the rates of $O_3$ decay and PM formation, which suggests inappropriate representation of reactions involving $NO_2$, such as erroneous accumulation of $IONO_2$. If $IONO_2$ accumulation is the reason for the poor underprediction of PM volume, the model error can be reduced either by assuming uptake of $IONO_2$ to particle or higher recycling rate of $IONO_2$. Since HR-ToF-AMS measurements suggest that the overall contribution from nitrate species is likely to be

minor (Fig.2,3), model B assumes a higher thermal decomposition rate (assumed to be same as that of $INO_2$, Reaction I-14) than that used for model A. Assuming faster decomposition of $IONO_2$ resolved the problem of underpredicting PM volume and moderately improved $O_3$ prediction. The better model performance using the higher thermal decomposition rate of $IONO_2$ indicates that reactions in Table 2 involving $NO_x$ (especially $NO_2$) are likely to be incomplete, resulting in accumulation of iodine (I) reservoir species such as $IONO_2$. When NO was initially present, particle formation was delayed until NO went down to a few ppb level (Run 738A, 743A, 1452B, 734A, and 743B); model A was unable to predict PM formation, again possibly due to accumulation of I reservoir species. Model B assuming higher thermal decomposition rate of $IONO_2$ resulted in reasonable prediction of PM and $O_3$. One thing to note is that currently there is no evidence to support the use of different thermal decomposition rate of $IONO_2$; the adjustment in the rate constant is only for demonstrating the impact of reducing reservoir species on PM prediction. Although no particle formation was observed for $CH_3I + h\nu$ run, models predicted particle formation likely due to incomplete representation of NO effect.

## 7.4   Conclusions

IOP formation from the photooxidation of $CH_3I$ within an environmental chamber under varied condition was investigated. Experiments were carried out under simplified (dry, no salt) and well-controlled conditions, providing fundamental insights on IOP formation. Immediate particle formation from the photolysis of $CH_3I$ was observed when $O_3$ was

initially present at a relatively high concentration (95-120 ppb), which is in agreement with previous studies. This study further evaluated the $NO_x$ effect on IOP formation. At lower $O_3$ concentrations, NO was observed to influence the onset time of IOP formation with threshold NO concentration of a few ppb, at least in the experimental conditions of this study. Particle mass yields were nearly 1.0 (0.7~1.2) when $O_3$was sufficiently high (e.g., ~100 ppb) and NO was relatively low (e.g., below ~2 ppb). Jimenez et al. (2003) investigated chemical composition of IOP formed from the photooxidation of $CH_2I_2$ without $NO_x$ by an Aerodyne AMS. In this study, aerosol mass spectra of IOP formed with and without $NO_x$ suggested that $NO_x$ does not significantly influence particle composition (only minor $NO^+$ and $NO_2^+$ fragments were observed) and that the role of $NO_x$ in this study was limited in gas-phase reactions. However, under atmospheric conditions, $NO_x$ may have complex impacts on IOP formation via aqueous reactions, which is beyond the scope of this study. The model developed in this study predicted IOP formation and $O_3$ decay reasonably only when $NO_x$ was absent. Underprediction of IOP was likely due to erroneous accumulation of iodine reservoir species formed by reactions with $NO_x$.

Aiken, A. C., DeCarlo, P. F., Kroll, J. H., Worsnop, D. R., Huffman, J. A., Docherty, K., Ulbrich, I., Mohr, C., Kimmenl, J. R., Sun, Y., Zhang, Q., Trimborn, A. M., Northway, M., Ziemann, P. J., Canagaratna, M. R., Onasch, T. B., Alfarra, M. R., Prevot, A. S., Dommen, J., Duplissy, J., Metzger, A., Baltensperger, U., Jimenez, J. L.: O/C and OM/OC ratios of primary, secondary, and ambient organic aerosols with High-Resolution Time-of-Flight Aerosol Mass Spectrometry, Environmental Science & Technology, 42, 4487-4485, 2008

Carter, W. P. L.: Development of the SAPRC-07 Chemical Mechanism and updated ozone reactivity scales, Final Report to the California Air Resources Board Contract No.03-318, June 15., Available at http://www.cert.ucr.edu/~carter/SAPRC, 2007

Carter, W. P. L., Cocker, D. R., Fitz, D. R., Malkina, I. L., Bumiller, K., Sauer, C. G., Pisano, J. T., Bufalino, C., Song, C.: A new environmental chamber for evaluation of gas-phase chemical mechanisms and secondary aerosol formation, Atmospheric Environment, 39, 7768-7788, 2005

Cocker, D. R., Flagan, R. C., Seinfeld, J. H.: State-of the art chamber facility for studying atmospheric aerosol chemistry, Environmental Science & Technology, 35(12), 2594-2601, 2001

DeCarlo, P. F., Kimmel, J. R., Trimborn, A. M., Northway, M., Jayne, J. T., Aiken, A. C., Gonin, M., Fuhrer, K., Horvath, T., Docherty, K., Worsnop, D. R., Jimenez, J. L.: Field-deployable, high-resolution, Time-of-Flight Aerosol Mass Spectrometer, Anal. Chem., 78, 8281-8289, 2006

Ehara, K., Hagwood, C., Coakley, K. J.: Novel method to classify aerosol particles according to their mass-to-charge ratio-Aerosol particle mass analyzer, Journal of Aerosol Science, 27(2), 217-234, 1996

Furneaux, K. L., Whalley, L. K., Heard, D. E., Atkinson, H. M., Bloss, W. J., Flynn, M. J., Gallagher, M. W., Ingham, T., Kramer, L., Lee, J. D., Leigh, R., McFiggans, G. B., Mahajan, A. S., Monks, P. S., Oetjen, H., Plane, J. M. C., Whitehead, J. D.: Measurements of iodine monoxide at a semi polluted coastal location, Atmos. Chem. Phys., 10(8), 3645-3663, 2010

Jayne, J. T., Leard, D. C., Zhang, X., Davidovits, P., Smith, K. A., Kolb, C. E., Worsnop, D. R.: Development of an Aerosol Mass Spectrometer for size and composition analysis of sibmicron particles, Aerosol Science and Technology, 33, 49-70, 2000


Jimenez, J. L., Bahreini, R., Cocker, D. R., Zhuang, H., Varutbangkul, V., Flagan, R. C., Seinfeld, J. H., O'Dowd, C. D., Hoffman, T.: New particle formation from photooxidation of diiodomethane (CH2I2), Journal of Geophysical Research, 108(D10) 2003


Kaltsoyannis, N., Plane, J. M. C.: Quantum chemical calculations on a selection of iodine-containing species (IO, OIO, INO3, (IO)2, I2O3, I2O4 and I2O5) of importance in the atmosphere, Physical Chemistry Chemical Physics, 10(13), 1723-1733, 2008


Khalizov, A. F., Zhang, R., Zhang, D., Xue, H., Pagels, J., McMurry, P. H.: Formation of highly hygroscopic soot aerosols upon internal mixing with sulfuric acid vapor, Journal of Geophysical Research, 114, D05208, doi: 10.1029/2008JD010595, 2009


Mahajan, A. S., Oetjen, H., Saiz-Lopez, A., Lee, J. D., McFiggans, G. B., Plane, J. M. C.: Reactive iodine species in a semi-polluted environment, Geophys. Res. Lett., 36(16), L16803, 2009


Mahajan, A. S., Sorribas, M., Gomez Martin, J. C., MacDonald, S. M., Gil, M., Plane, J. M. C., Saiz-Lopez, A.: Concurrent observations of atomic iodine, molecular iodine and ultrafine particles in a coastal environment, Atmos. Chem. Phys., 11(6), 2545-2555, 2011


Malloy, Q., Nakao, S., Qi, L., Austin, R. L., Stothers, C., Hagino, H., Cocker, D. R.: Real-time aerosol density determination utilizing a modified Scanning Mobility Particle Sizer - Aerosol Particle Mass Analyzer system, Aerosol Science and Technology, 43, 673-678, 2009


McFiggans, G., Bale, C. S. E., Ball, S. M., Beames, J. M., Bloss, W. J., Carpenter, L. J., Dorsey, J., Dunk, R., Flynn, M. J., Furneaux, K. L., Gallagher, M. W., Heard, D. E., Hollingsworth, A. M., Hornsby, K., Ingham, T., Jones, C. E., Jones, R. L., Kramer, L. J., Langridge, J. M., Leblanc, C., LeCrane, J. P., Lee, J. D., Leigh, R. J., Longley, I., Mahajan, A. S., Monks, P. S., Oetjen, H., Orr-Ewing, A. J., Plane, J. M. C., Potin, P., Shillings, A. J. L., Thomas, F., von Glasow, R., Wada, R., Whalley, L. K., Whitehead, J. D.: Iodine-mediated coastal particle formation: an overview of the Reactive Halogens in

the Marine Boundary Layer (RHaMBLe) Roscoff coastal study, Atmos. Chem. Phys., 10(6), 2975-2999, 2010

McFiggans, G., Plane, J. M. C., Allan, B. J., Carpenter, L. J., Coe, H., O'Dowd, C.: A modeling study of iodine chemistry in the marine boundary layer, J. Geophys. Res., 105(D11), 14371-14385, 2000

McMurry, P. H., Wang, X. W., Park, K., Ehara, K.: The relationship between mass and mobility for atmospheric particles: A new technique for measuring particle density, Aerosol Science and Technology, 36, 227-238, 2002

Nakao, S., Shrivastava, M., Nguyen, A., Jung, H., Cocker, D.: Interpretation of Secondary Organic Aerosol Formation from Diesel Exhaust Photooxidation in an Environmental Chamber, Aerosol Science and Technology, 45(8), 954-962, 2011

Nakao, S., Tang, P., Tang, X., Clark, C. H., Qi, L., Heo, E., Asa-Awuku, A., Cocker, D. R.: Density and elemental ratios of secondary organic aerosol: application of a density prediction method, submitted 2012

O'Dowd, C. D., de Leeuw, G.: Marine aerosol production: a review of the current knowledge, Philosophical Transactions of the Royal Society A: Mathematical, Physical and Engineering Sciences, 365(1856), 1753-1774, 2007

O'Dowd, C. D., Jimenez, J. L., Flagan, R. C., Seinfeld, J. H., Kulmala, M., Hoffman, T.: Marine aerosol formation from biogenic iodine emissions, Nature, 417, 632-636, 2002

Park, K., Kittelson, D. B., McMurry, P. H.: Relationship between particle mass and mobility for diesel exhaust particles, Environmental Science & Technology, 37(3), 577-583, 2003

Pirjola, L., O'Dowd, C. D., Yoon, Y. J., Sellegri, K.: Modelling Iodine Particle Formation and Growth from Seaweed in a Chamber, Environ. Chem., 2, 271-281, 2005

Qi, L., Nakao, S., Malloy, Q., Warren, B., Cocker, D. R.: Can secondary organic aerosol formed in an atmospheric simulation chamber continuously age?, Atmospheric Environment, 44, 2990-2996, 2010

Rader, D. J., McMurry, P. H.: Application of the Tandem Differential Mobility Analyzer to studies of droplet growth or evaporation, Journal of Aerosol Science, 17(5), 771-787, 1986

Rogak, S. N., Baltensperger, U., Flagan, R. C.: Measurement of Mass Transfer to Agglomerate Aerosols, Aerosol Science and Technology, 14(4), 447-458, 1991

Saiz-Lopez, A., Plane, J. M. C.: Novel iodine chemistry in the marine boundary layer, Geophys. Res. Lett., 31(4), L04112, 2004

Saiz-Lopez, A., Plane, J. M. C., Baker, A. R., Carpenter, L. J., von Glasow, R., Gómez Martín, J. C., McFiggans, G., Saunders, R. W.: Atmospheric Chemistry of Iodine, Chemical Reviews 2011

Saiz-Lopez, A., Plane, J. M. C., Mahajan, A. S., Anderson, P. S., Bauguitte, S. J. B., Jones, A. E., Roscoe, H. K., Salmon, R. A., Bloss, W. J., Lee, J. D., Heard, D. E.: On the vertical distribution of boundary layer halogens over coastal Antarctica: implications for O3, HOx, NOx and the Hg lifetime, Atmos. Chem. Phys., 8(4), 887-900, 2008

Sander, S. J., Abbatt, J., Barker, J. R., Burkholder, J. B., Friedl, R. R., Golden, D. M., Huie, R. E., Kolb, C. E., Kurylo, M. J., Moortgat, G. K., Orkin, V. L., Wine, P. H.: Chemical kinetics and photochemical data for use in atmospheric studies, Evaluation No. 17, JPL Publication 10-6(http://jpldataeval.jpl.nasa.gov) 2011

Stroud, C. A., Makar, P. A., Michelangeli, D. V., Mozurkewich, M., Hastie, D. R., Barbu, A., Humble, J.: Simulating organic aerosol formation during the photooxidation of toluene/NOx mixtures: Comparing the equilibrium and kinetic assumption, Environmental Science & Technology, 38, 1471-1479, 2004

Xue, H., Khalizov, A. F., Wang, L., Zheng, J., Zhang, R.: Effects of coating of dicarboxylic acids on the mass-mobility relationship of soot particles, Environmental Science & Technology, 43, 2787-2792, 2009

## 7.5 Tables

Table 7.1 Experimental matrix

| RunID | Reactants | Run type | Initial Concentrations CH$_3$I (ppb) | NO (ppb) | NO$_2$ (ppb) | CO (ppm) | O$_3$ (ppb) | Chamber dilution Tracer | Dilution[a] (% hr$^{-1}$) | ΔCH$_3$I (μg/m$^3$) | PM mass (μg/m$^3$)[b] | Yield (PM / ΔCH$_3$I) |
|---|---|---|---|---|---|---|---|---|---|---|---|---|
| 1453B | CH$_3$I | No O$_3$ | 503 | - | - | - | - | n-C$_6$F$_{14}$ | 0.08 | 59 | 0 | 0.00 |
| 738A | CH$_3$I + NO$_x$ | Slow O$_3$ formation | 202 | 16 | 8 | - | - | none | 0.68[f] | 10 | 0.1[c] | 0.91 |
| 743A | CH$_3$I + NO$_x$ | | 502 | 16 | 8 | - | - | none | 0.68[f] | 26 | 17.7[c] | 0.58 |
| 1452B | CH$_3$I + NO$_x$ | | 495 | 17 | 9 | - | - | none | 0.21[g] | 14 | 0.1[c] | 0.01 |
| 734A | CH$_3$I + NO$_x$ + CO | O$_3$ formation enhanced by CO | 201 | 16 | 8 | 56 | - | CO | 0.63 | 44 | 39.9[d] | 0.90 |
| 734B | CH$_3$I + NO$_x$ + CO | | 199 | 16 | 8 | 57 | - | CO | 0.58 | 38 | 38.0[d] | 1.01 |
| 738B | CH$_3$I + NO$_x$ + CO | | 201 | 16 | 8 | 55 | - | CO | 0.67 | 41 | 38.7[d] | 0.93 |
| 743B | CH$_3$I + NO$_x$ + CO | | 503 | 16 | 8 | 4 | - | none[h] | 0.68[f] | 120 | 49.2[d] | 0.41 |
| 1453A | CH$_3$I + O$_3$ | Excess O$_3$ | 499 | - | - | - | 100 | n-C$_6$F$_{14}$ | 0.33 | 71 | 86.5[e] | 1.22 |
| 742A | CH$_3$I + O$_3$ + CO | | 344 | - | - | 58 | 95 | CO | 0.85 | 83 | 71.5[e] | 0.86 |
| 1454A | CH$_3$I + O$_3$ + CO | | 490[i] | - | - | 4 | 120 | CO | 0.00 | - | 78.9[e] | - |
| 1452A | CH$_3$I + NO$_x$ + O$_3$ | | 490 | - | 24 | - | 110 | none | 0.21[g] | 136 | 99.7[e] | 0.73 |

a: Based on dilution at 6 hours after lights on.

b: Wall-loss corrected PM volume concentration multiplied by PM effective density (6 hours after lights on).

c: Density 1.46 g/cm$^3$ is assumed based on approximately 200 min delay in PM size evolution compared to excess ozone experiments.

d: Density 1.74 g/cm$^3$ is assumed based on approximately 100 min delay in PM size evolution compared to excess ozone experiments.

e: Average measured density 2.03 g/cm$^3$ (6 hours after lights on) for excess ozone experiments is used.

f: Average dilution rates of Runs 734A, 734B, and 738B (tracer: CO) is used. Dilution rates of Runs 1453A and 1453B is not included in the average since these runs were carried out four years later and dilution rates were significantly smaller.

g: Average dilution rates of Runs 1453A and 1453B (tracer: n-C$_6$F14) is used.

h: Using CO as a tracer resulted in unrealistically high PM yield (>>1) possibly due to lower concentration of CO and unknown interference

i: GC data not available. Initial concentration is calculated by injected amount/chamber volume

171

Table 7.2 Mechanism for methyl iodide used in this study to predict IOP formation

| Label | Reaction and Products [a] | Rate Parameters [b] | | | | Refs& Notes [c] |
|---|---|---|---|---|---|---|
| | | k(298) | A | Ea | B | |
| *Gas-phase reactions* | | | | | | |
| I-01) | CH3I + HV = MEO2 + I | | Phot Set=CH3I | | | 1,2 |
| I-02) | CH3I + OH = RO2C + xHCHO + I | 1.00E-13 | 4.3E-12 | 2.226 | | 1,3 |
| I-03) | I + O3 = IO + O2 | 1.30E-12 | 2.1E-11 | 1.649 | | 1 |
| I-04) | I + HO2 = HI + O2 | 3.87E-13 | 1.5E-11 | 2.166 | | 1 |
| I-05) | I + NO = INO | 3.73E-13 | Falloff, F=0.60, N=1.03 | | | 1 |
| | | | 1.8E-32 | 0 | -1 | |
| | | | 1.7E-11 | 0 | | |
| | | | 0.60 | 1.03 | | |
| I-06) | I + NO2 = INO2 | 5.24E-12 | Falloff, F=0.63, N = 1.03 | | | 1 |
| | | | 3E-31 | 0 | -1 | |
| | | | 6.6E-11 | 0 | | |
| | | | 0.63 | 1 | | |
| I-07) | I + NO3 = IO + NO2 | 1E-10 | | | | 1 |
| I-08) | I + INO = I2 + NO | 1.66E-10 | | | | 4 |
| I-09) | I + INO2 = I2 + NO2 | 8.32E-11 | | | | 4 |
| I-10) | INO + HV = I + NO | | Phot Set=INO | | | 5 |
| I-11) | INO + INO = I2 + #2 NO | 1.28E-14 | 8.4E-11 | 5.206 | | 1 |
| I-12) | INO2 + HV = I + NO2 | | Phot Set=INO2 | | | 5 |
| I-13) | INO2 + INO2 = I2 + #2 NO2 | 1.73E-15 | 4.7E-13 | 3.319 | | 1 |
| I-14) | INO2 = I + NO2 | 5.2 | 9.936E+17 | 23.57 | | 6, 7 |
| I-15) | I2 + HV = #2 I | | Phot Set=I2 | | | 5 |
| I-16) | I2 + OH = HOI + I | 2.1E-10 | | | | 1 |
| I-17) | I2 + NO3 = I + IONO2 | 1.5E-12 | | | | 1 |
| I-18) | I2 + O3P = IO + I | 1.4E-10 | | | | 5 |
| I-19) | I2 + O3 = IO + I + O2 | 3.8E-18 | | | | 6 |
| I-20) | I2 + O3 = OIO + IO | 3.8E-18 | | | | 6 |
| I-21) | HI + HV = HO2 + I | | Phot Set=HI | | | 1 |
| I-23) | HI + OH = H2O + I | 7.00E-11 | 1.6E-11 | -0.8744 | | 1 |
| I-24) | IO + IO = I + OIO | 4.95E-11 | | | | 8 |
| I-25) | IO + IO = I2O2 | 3.96E-11 | | | | 8 |
| I-26) | I2O2 = OIO + I | 20 | | | | 9 |
| I-27) | I2O2 + O3 = I2O3 + O2 | 1E-12 | | | | 10 |

| | | | | | | |
|---|---|---|---|---|---|---|
| I-28) | OIO + IO = I2O3 | 1.2E-10 | | | | |
| I-29) | OIO + OH = HOIO2 | 9.73E-11 | 2.2E-10 | 0.4829 | | 10 |
| I-30) | I2O3 + O3 = I2O4 | 1E-12 | | | | 10 |
| I-31) | OIO + OIO = I2O4 | 1.2E-10 | | | | 10 |
| I-32) | I2O4 + O3 = I2O5 | 1E-12 | | | | 10 |
| I-33) | OIO + NO = IO + NO2 | 6.78E-12 | 1.1E-12 | -1.077 | | 1 |
| I-34) | OIO + HV = I + O2 | | Phot Set=OIO | | | 5 |
| I-35) | IO + MEO2 = I + O2 + HCHO + HO2 | 2E-12 | | | | 8 |
| I-36) | IO + HO2 = HOI + O2 | 8.57E-11 | 1.4E-11 | -1.073 | | 1 |
| I-37) | IO + NO = I + NO2 | 1.96E-11 | 7.15E-12 | -0.596 | | 1 |
| I-38) | IO + NO2 = IONO2 | 3.54E-12 | Falloff, F=0.4, N=1.255 | | | 1 |
| | | | 7.7E-31 | 0 | -5 | |
| | | | 1.6E-11 | 0 | | |
| | | | 0.4 | 1.255 | | |
| I-39) | IO + NO3 = OIO + NO2 | 9E-12 | | | | 1 |
| I-40) | IO + O3 = I + #2 O2 | 1E-15 | | | | 1,11 |
| I-41) | IO +O3 = OIO + O2 | 2E-16 | | | | 1,11 |
| I-42) | IO + O3P = O2 + I | 1.4E-10 | | | | 1 |
| I-43) | IO + HV = I + O3P | | Phot Set=IO | | | 1 |
| I-44) | IONO2 + HV = I + NO3 | | Phot Set=IONO2 | | | 5 |
| I-45) | IONO2 = IO + NO2 | 2.90E-03 | 1.1E+15 | 23.97 | | 1 |
| I-46) | IONO2 + I = I2 + NO3 | 5.58E-11 | 9.1E-11 | 0.2901 | | 12,13 |
| I-47) | HOI + HV = OH + I | | Phot Set=HOI | | | 1 |

*Particle formation*

| Condensable species | Accomodation coefficients | |
|---|---|---|
| IO | 0.02 | 6,10 |
| OIO | 1 | 6,10 |
| HI | 0.02 | 6,10 |
| HOI | 0.02 | 6,10 |
| I2O5 | 0.02 | 6,10 |

[a] The same naming convention as used for the SAPRC-07 chemical mechanism (Carter, 2007) is used. Format of reaction listing: "=" separates reactants from products; "#number" indicates stoichiometric coefficient.

[b] The representation of rate parameters is same as in SAPRC-07. Except as indicated, the rate constants are given by $k(T) = A \cdot (T/300)^B \cdot e^{-Ea/RT}$, where the units of k and A

are cm$^3$ molec$^{-1}$ s$^{-1}$, Ea are kcal mol$^{-1}$, T is $^o$K, and R=0.0019872 kcal mol$^{-1}$ deg$^{-1}$. The following special rate constant expressions are used:

<u>Phot Set = name:</u> The absorption cross sections taken from references, where "name" indicates the photolysis set used. Unit quantum yields are assumed.

<u>Falloff:</u> The rate constant as a function of temperature and pressure is calculated using $k(T,M) = (k_0(T) \cdot [M]/[1 + k_0(T) \cdot [M]k_{inf}(T)) \cdot F^Z$, where $Z = [1 + \{\log_{10}(k_0(T) \cdot [M]/k_{inf}(T))/N\}^2]^{-1}$, [M] is the total pressure in molecules cm$^{-3}$, F and N are as indicated on the table, and the temperature dependences of $k_0$ and $k_{inf}$ are as indicated on the table.

[c] Footnotes documenting sources of rate constants and mechanisms are as follows:

[1] Rate constant or absorption coefficients based on IUPAC recommendation (current as of April 2012, http://www.iupac-kinetic.ch.cam.ac.uk). Unit quantum yields are assumed for photolysis reactions. Mechanism is also as recommended as IUPAC unless noted otherwise. [2] MEO2 is methyl peroxy radicals. [3] Although photolysis is the major loss process of CH$_3$I, reaction with OH radicals also occurs to some extent. Expected HCHO formation and NO to NO$_2$ conversion dependent on NO level are represented as xHCHO and RO2C. [4] NIST chemical kinetics database, http://kinetics.nist.gov/kinetics/. [5] NASA/JPL evaluation (Sander et al., 2011), http://jpldataeval.jpl.nasa.gov/. [6] McFiggans et al. (2000). [7] Noted as (2.4/0.005) x 2.07 x 10$^{15}$ e$^{(-11859/T)}$. [8] Saiz-Lopez et al. (2011). [9] The overall rate constant for IO + IO is k = 9.9x10$^{-11}$. The branching ratio is assumed to be ~50% for I$_2$O$_2$ forming channel and ~40% for the OIO forming channel (Saiz-Lopez et al., 2011, reaction 15a and 15b). [10] Jimenez et al. (2003). [11] Furneaux et al. (2010). [12] Upper limit values. [13] Kaltsoyannis and Plane (2008). [14] The recommended value. Upper limit: 1.6x10$^{-10}$e$^{(-146/T)}$. Lower limit: 2.5x10$^{-12}$e$^{(-146/T)}$.
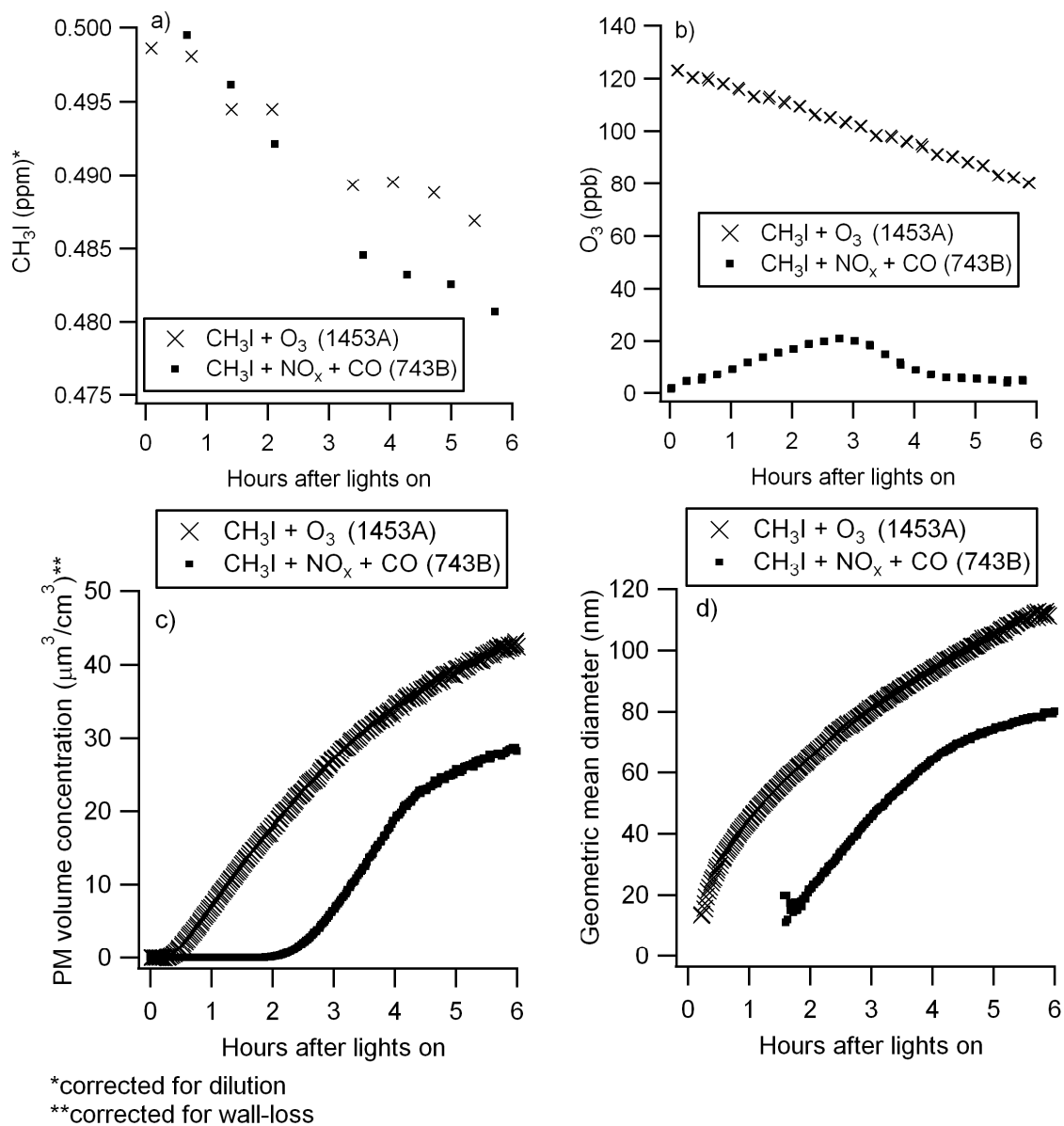
## 7.6    Figures



Figure 7.1  Time series of (a) CH₃I concentration, (b) O₃ concentration, (c) particle volume concentration, and (d) particle geometric mean diameter for Runs 743B and 1453A. Experiments with excess O₃ (Run 1453A) resulted in immediate particle formation.
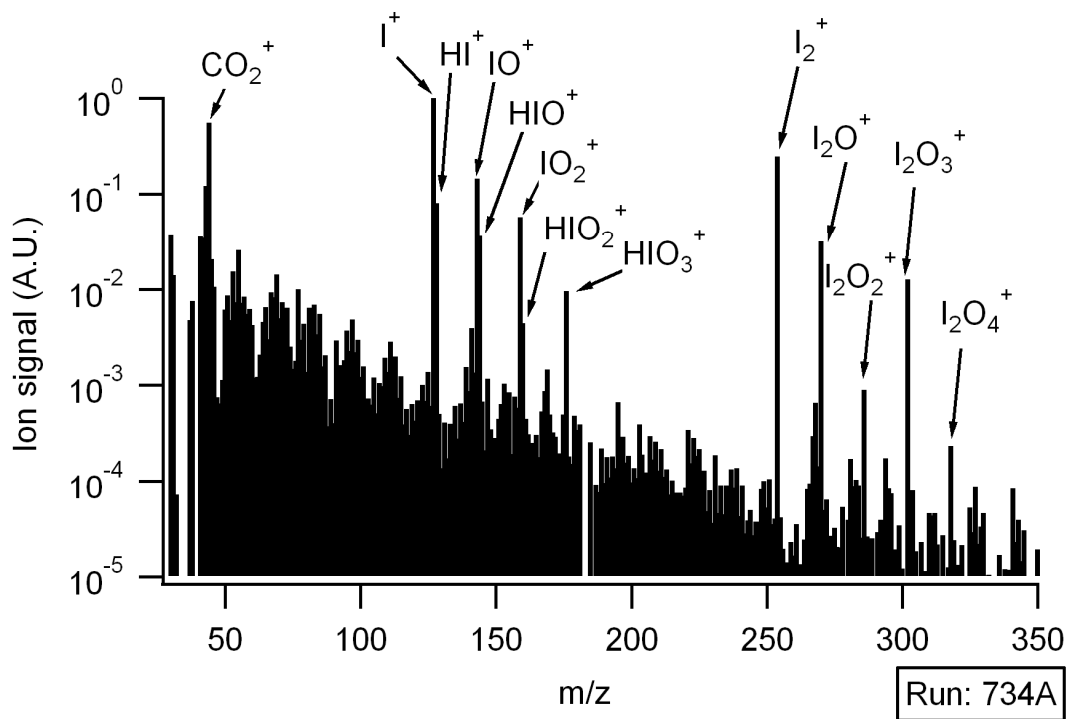
Figure 7.2 Mass spectra of IOP acquired by a HR-ToF-AMS. Formulae are confirmed by high-resolution analysis.
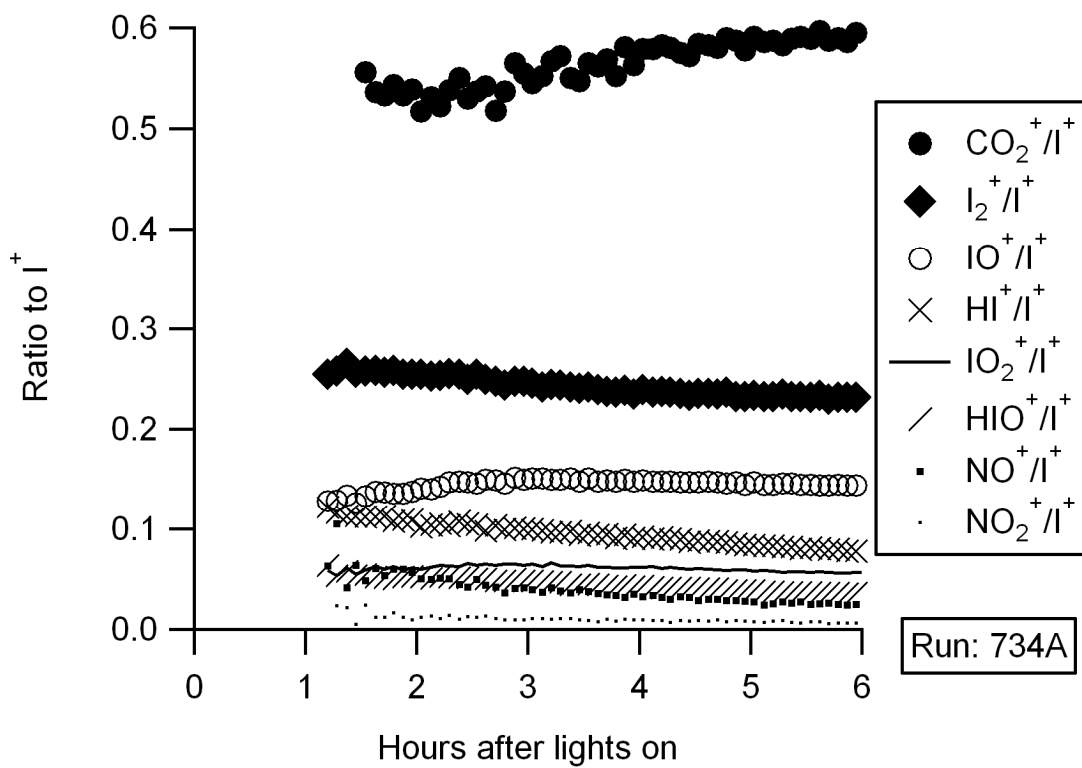
Figure 7.3 Time series of major ions measured by a HR-ToF-AMS indicating minor change in particle composition.
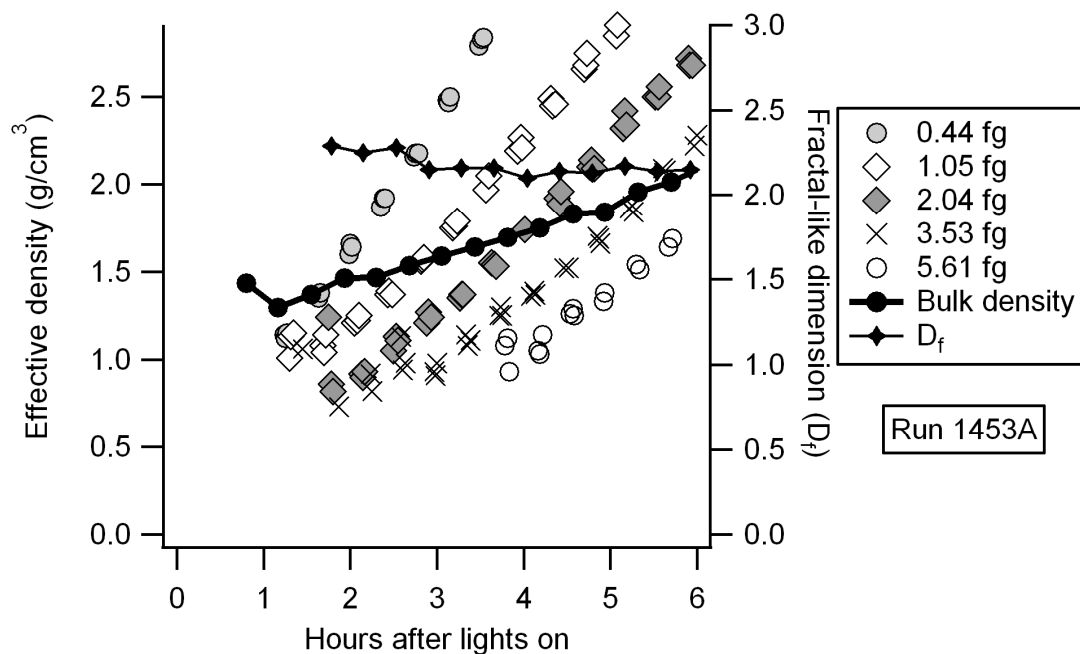
Figure 7.4 Time series of particle effective density measured by an APM-SMPS. The APM setting is alternated to select particles with predetermined masses (shown in femtogram); size-dependence of density is utilized to calculate fractal-like dimension ($D_f$) and bulk-effective density (see text and Fig. 5 for detail).
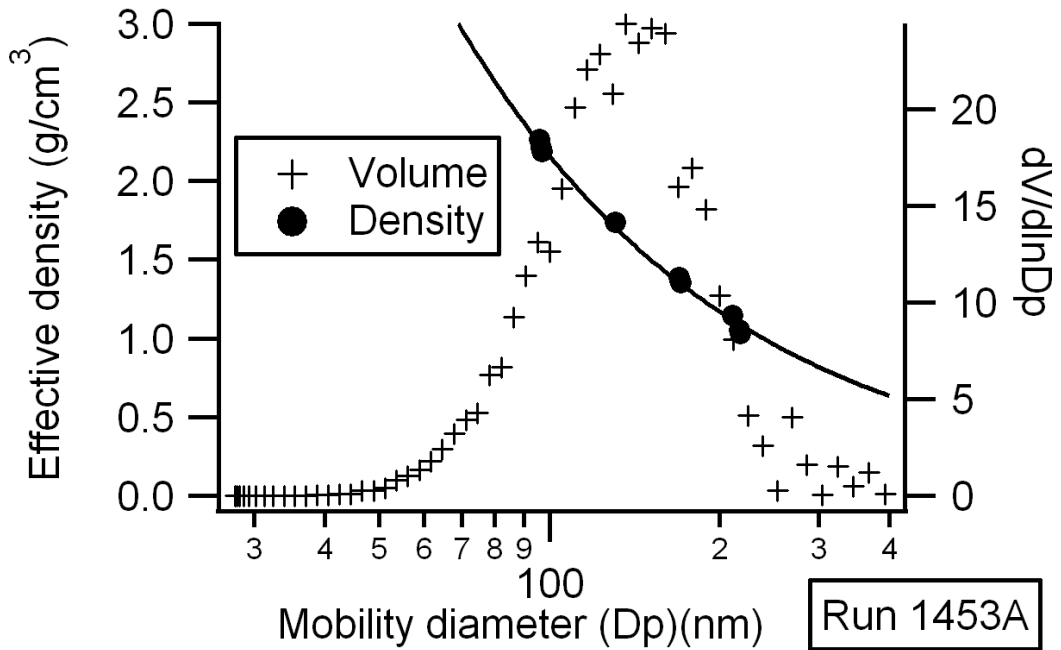
Figure 7.5 An example of size-dependent density (fitted to a power function) and particle volume distribution. Particle mass concentration is calculated by integrating the size-dependent density and volume distribution over the SMPS scan range. The power of the fit is used to calculate fractal-like dimension ($D_f$) (Eq.1).
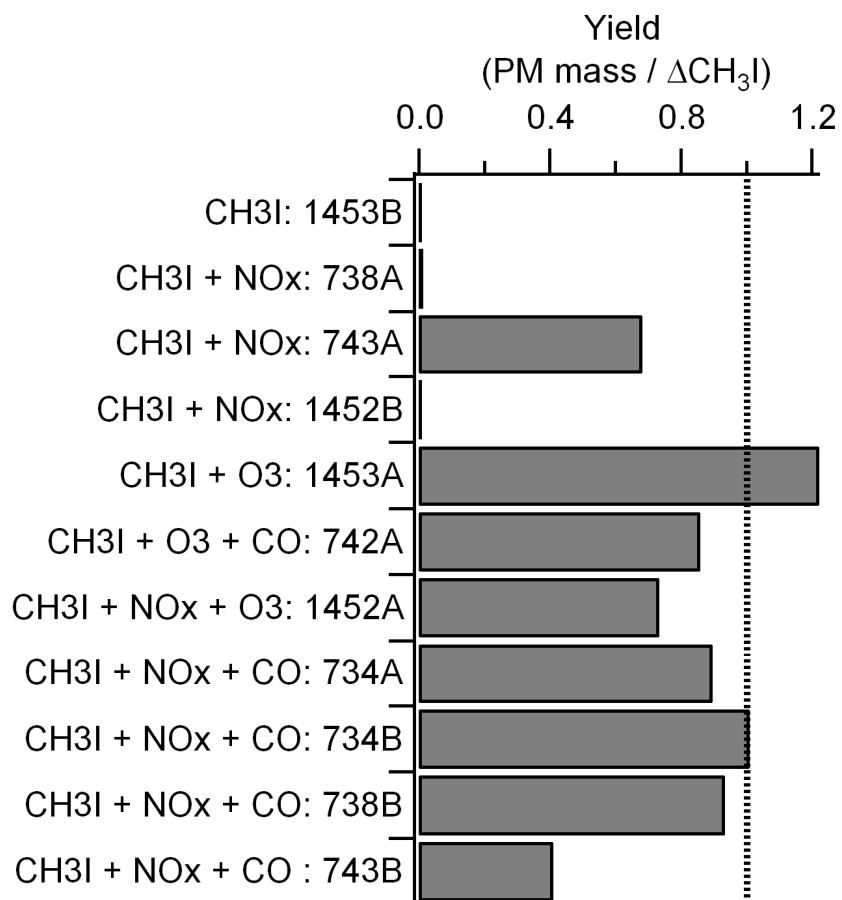
Figure 7.6 Mass-based particle formation yield (IOP mass formed / CH$_3$I mass reacted). IOP mass formed is calculated by wall-loss corrected PM volume concentration and effective density.
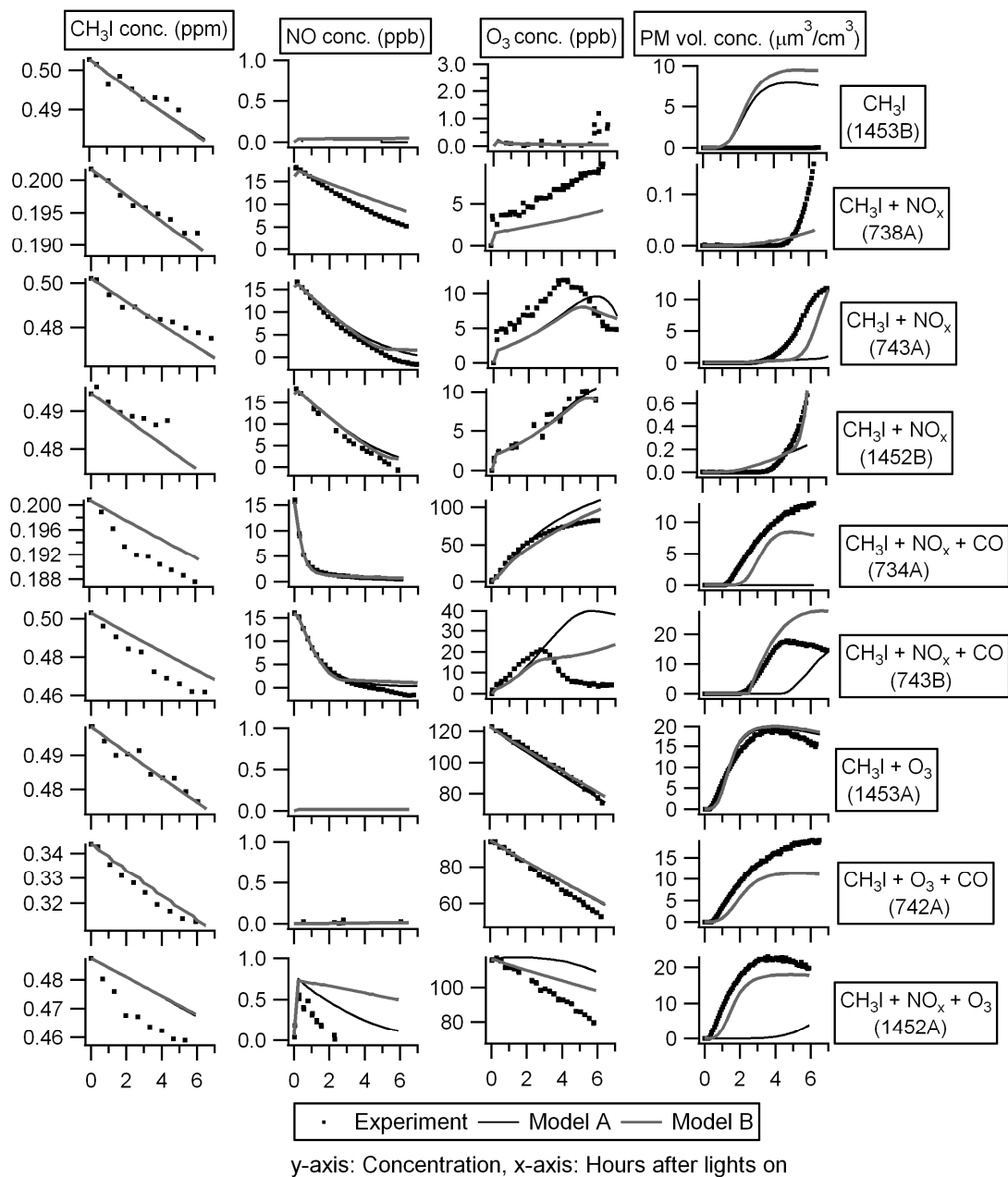
Figure 7.7 Comparison of experimental and modeling results. Model A uses the mechanism shown in Table 2; Model B uses an arbitrarily enhanced IONO$_2$ thermolysis rate as discussed in text.
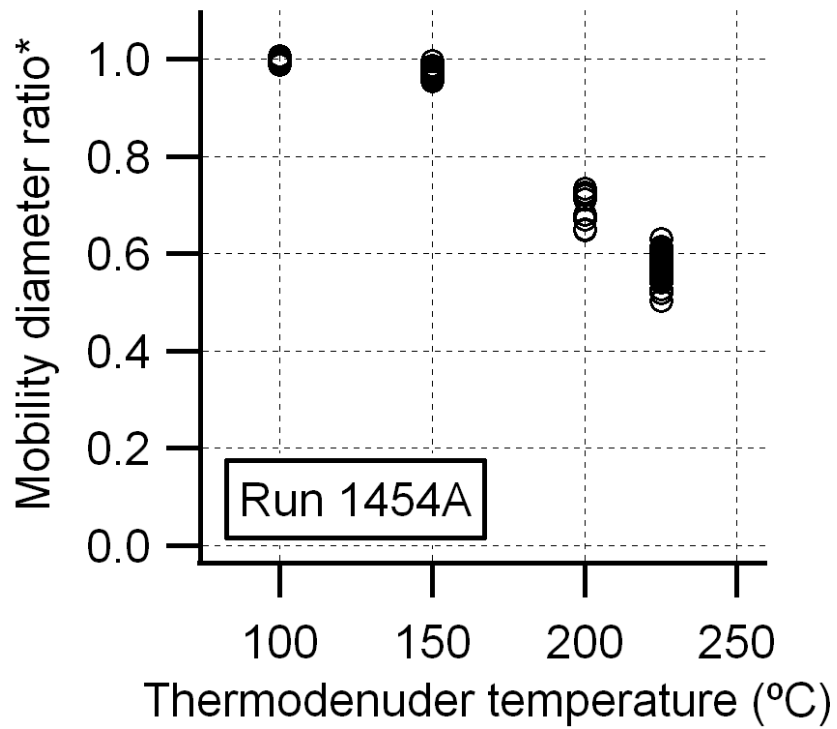
Figure 7.8 Temperature profile of IOP shrinkage measured by a VTDMA. The reduction in particle mobility diameter is either due to evaporation or restructuring (collapsing) of agglomerates. *Mobility diameter of particles after a thermodenuder (TD) divided by that before TD.
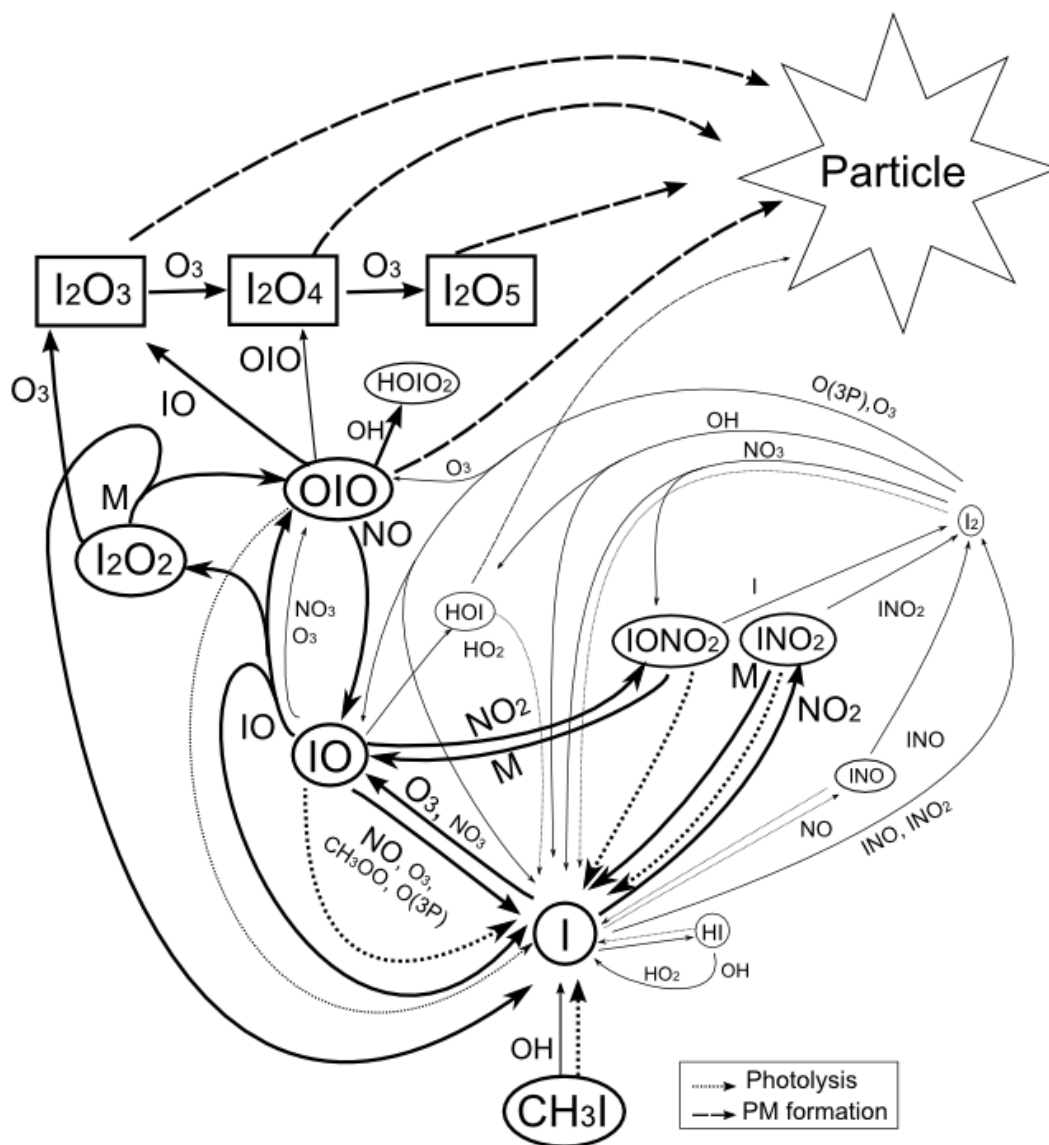
Figure 7.9 Reaction mechanisms used in this study to model IOP formation. Minor reactions are noted by thin lines and reactant names in a small size.

## 8    Summary of Dissertation

The overall objective of this study was to advance the understanding of anthropogenic influences on SOA formation with the major emphasis on aromatic SOA formation. The goal was achieved by directly evaluating the significance of major intermediate species of aromatic hydrocarbon oxidation, phenolic compounds and glyoxal as part of the complex multi-generational reaction systems. Another facet of this study developed and extensively utilized a new real-time density measurement system, an APM-SMPS, which provided insights on not only the aromatic-SOA system but also other atmospherically relevant systems such as oxidation of biogenic hydrocarbons (isoprene, monoterpenes, and sesquiterpenes), diesel exhaust, and methyl iodide ($CH_3I$).

Chapter 2 evaluated the significance of phenolic compounds as intermediate species of aromatic SOA and investigated possible mechanisms of aromatic/phenol SOA formation in the absence of $NO_x$. Measurements of SOA formation yields from aromatics and phenolics combined with gas-phase measurements indicated that approximately 20% of the SOA of benzene, toluene, and $m$-xylene could be attributed to the phenolic route in the low $NO_x$ conditions. Furthermore, this study described the first application of PILS as an on-line interface between an environmental chamber and an ESI-TOFMS. The PILS-TOFMS and off-line filter analysis of SOA agreed, with some additional possible water soluble gas phase products observed by PILS-TOFMS such as catechols. Major peaks observed in the TOFMS agreed with the currently accepted assumption of bicyclic

hydroperoxide formation. Although phenolic compounds were shown to contribute significantly to aromatic SOA formation, the majority (~80%) of aromatic SOA formation pathways remained uncertain. This study is a basis for future studies to evaluate the significance of other major first generation products of aromatic hydrocarbons, such as unsaturated dicarbonyls and benzaldehyde-type products. Additionally, identification of additional species by soft-ionization techniques is beneficial.

Chapter 3 extended Chapter 2, further evaluating glyoxal, another significant first generation product of aromatic hydrocarbon oxidation. Rapid SOA formation via glyoxal uptake onto deliquesced $(NH_4)_2SO_4$ was observed as shown in previous studies; however, no significant glyoxal uptake onto SOA formed from aromatic hydrocarbon oxidation was observed. As opposed to the current belief, the role of glyoxal in aromatic SOA formation was observed to be merely an OH radical source following photolysis, instead of contributing to SOA formation by reactive uptake, for the experimental conditions of this study (RH less than 80%). Thus, this study suggests that glyoxal uptake onto aerosol is more limited than previously thought. Since glyoxal is a significant reaction product of a number of atmospherically relevant hydrocarbons, the approach of this study has a profound potential to improve the understanding of the role of glyoxal in SOA formation from globally significant hydrocarbons (e.g., isoprene).

Chapter 4 described the development of the APM-SMPS system, which was heavily utilized in the following chapters. By locating the APM upstream of the SMPS, as opposed to the more common configuration of the DMA-APM, the new system performed density measurement at the time resolution of the SMPS (approximately 30 times faster than the traditional DMA-APM setup). Density measurement by APM-SMPS agreed with another technique based on different measurement principles (DMA-AMS), during $\alpha$-pinene and $m$-xylene SOA formation.

Chapter 5 described the extensive dataset of density and elemental ratios (O/C and H/C) of SOA formed by the oxidation of 23 different reactants including terpenes, aromatic hydrocarbons, and phenolic compounds within an environmental chamber; the dataset was utilized to evaluate a recently proposed semi-empirical relationship between organic aerosols density, O/C, and H/C. Experimental results suggested that SOA density was found to be nearly independent of oxidants used in chamber experiments. The semi-empirical relationship successfully predicted density of SOA within 20% error for more than 90% of experiments; therefore, the range of the application has been extended to include anthropogenic systems. The density estimation method has a potential to be applied to a number of predictive models. This study provided a fundamental dataset to support the applicability of the method to SOA formation from aromatic hydrocarbons. Future studies need to address the uncertainty due to the presence of nitrogen and sulfur in SOA.

Chapter 6 applied the APM-SMPS, as well as other chemical and physical instrumentation, to SOA formation from the oxidation of dilute diesel exhaust within an environmental chamber. The unique configuration of the APM-SMPS system enabled the determination of particle effective density as a function of particle mass (and size), thereby providing particle fractal-like dimension. The fractal-like dimensions of diesel particles were observed to be ~ 2.2 – 3.0 by the APM-SMPS, indicating the particle shape could either be fractal-like or nearly spherical depending on injection/dilution methods for the diesel exhaust.  Particle volume concentration was insensitive to SOA formation for fractal-like particles due to the filling of void spaces of agglomerate particles by secondary organics, highlighting the importance of mass-based analysis in interpreting SOA formation from diesel exhaust, or other systems involving fractal-like particles. The HR-ToF-AMS measurement showed that SOA contributed to 80% of OA mass within 12 hours, emphasizing the importance of diesel exhaust as a source of urban SOA. Experimental conditions, specifically injection and dilution methods were shown to have critical effects on physical evolution of particles. This study's approach bridged the gap between SOA studies of individual compounds to complex mixtures containing fractal-like agglomerate particles. Appropriate treatment of fractal-like agglomerate, as was done in this study, is critical in interpreting SOA formation from combustion sources, as well as other physical processes such as water uptake onto agglomerate.

Finally, iodine oxide particle (IOP) formation from the photooxidation of $CH_3I$ within an environmental chamber was investigated; since previous studies reported fractal-like

187

structure of IOP, this study applied the APM-SMPS and other chemical/physical instrumentation to acquire new mass-based insights on IOP formation. Immediate particle formation from the photolysis of $CH_3I$ was observed when high concentration of $O_3$ was initially present (95-120 ppb) in agreement with previous studies. This study further evaluated the $NO_x$ effect on IOP formation. At lower $O_3$ concentration, NO was observed to influence onset of IOP formation with threshold NO concentration of a few ppb. Particle mass yields were nearly one (0.7~1.2) when sufficiently high $O_3$/low NO was present. Aerosol mass spectra of IOP formed with and without $NO_x$ suggested that $NO_x$ does not significantly influence particle composition (only minor $NO^+$ and $NO_2^+$ fragments are observed), and hence the role of $NO_x$ in this study was limited togas-phase reactions. A predictive model was developed by including iodine chemistry to SAPRC-07 mechanism. The model predicted IOP formation and $O_3$ decay reasonably only when $NO_x$ was absent. IOP was underpredicted when $NO_x$ was present, suggesting that the current understanding in iodine reactions involving $NO_x$ is incomplete.

The combination of chemical and physical investigations of this study advanced understanding of the significance of intermediate species in aromatic SOA formation, as well as SOA formation processes in a number of atmospherically relevant systems. The unique approaches and findings of this work provide foundations for future development of SOA models to better understand the anthropogenic influence on urban air quality and global climate.